Dissertation
submitted to the
Combined Faculties for the Natural Sciences and for Mathematics
of the Ruperto-Carola University of Heidelberg, Germany
for the degree of
Doctor of Natural Sciences

presented by
Diplom-Physikerin Nicole Ursula Hannelore Frindt
born in Angol, Chile
Oral examination: February 06$^{\text{th}}$ 2013

Development and implementation of electrostatic Zach phase plates for phase contrast transmission electron microscopy

Referees:

Prof. Dr. Rasmus R. Schröder

Prof. Dr. Ulrich Schwarz

Entwicklung und Anwendung elektrostatischer Zach Phasenplatten für die Phasenkontrast Transmissionselektronenmikroskopie

Die Transmissionselektronenmikroskopie (TEM) spielt eine zentrale Rolle in der Strukturaufklärung von biologischen und materialwissenschaftlichen Proben. Geräteseitig sind Auflösungen im sub-Ångstrøm Bereich möglich. Schwache Phasenobjekte erreichen diese Auflösung aufgrund ihres niedrigen Signal-Rausch-Verhältnis nicht. Da die Strukturinformation schwacher Phasenobjekte hauptsächlich in ihrem Phasenkontrast enthalten ist, besteht die konventionelle Methode zur Verstärkung ihres Phasenkontrasts in der Bildaufnahme mit hohem Defokus. Dies verringert die erreichbare Auflösung und führt, aufgrund der sinusförmigen Phasenkontrast-Transferfunktion, zu einer Kontrastumkehr für verschiedene Ortfrequenzen des Objekts. Aufgrund dieser Probleme ist die Entwicklung von physikalischen Phasenplatten für die in-Fokus Phasenkontrast-Verstärkung in der TEM von großem Interesse. In dieser Arbeit wird die Entwicklung und Anwendung der elektrostatischen Zach Phasenplatte (ZPP) vorgestellt. Der Einfluss der ZPP Positionierung auf das entstehende single sideband Bildartefakt wird untersucht. Die Anwendbarkeit der ZPP zur Erzeugung von invertierbarem und abstimmbarem Phasenkontrast wird an gefrorenen, hydratisierten biologischen Proben erstmals demonstriert. Es werden ZPP Kontaminationen, daraus resultierende Aufladungsartefakte und mögliche Lösungen dieser Probleme vorgestellt. Weiterhin wird die Anwendbarkeit der ZPP in einer konventionellen Elektronenoptik und in einem Mikroskop mit Diffraktions-Vergrößerungs-Einheit und Aberrationskorrektor verglichen. Daraus ergeben sich Weiterentwicklungen in Richtung einer abschattungsfreien, anamorphen Phasenplatte (APP), für die auf Simulationen basierende Vergleiche zwischen ZPP und APP diskutiert werden.

Development and implementation of electrostatic Zach phase plates for phase contrast transmission electron microscopy

Transmission electron microscopy (TEM) plays an important role in structure determination of biological or material science samples. Resolutions up to the sub-Ångstrøm range are attainable. Weak phase objects do not reach this resolution due to their low signal-to-noise ratio. As the structure information of weak phase objects is mainly contained in their phase contrast, the conventional method for contrast enhancement is image acquisition at high defocus. This leads to a lower attainable resolution and contrast inversion for different spatial frequencies, due to the sinusoidal phase contrast transfer function. As a consequence of these drawbacks, the development of physical phase plates for in-focus phase contrast enhancement in TEM is of widest interest. In this thesis the development and application of the electrostatic Zach phase plate (ZPP) is presented. The impact of ZPP positioning on single sideband image artefacts is investigated. The applicability of the ZPP for inducing invertible and tunable phase contrast is demonstrated for the first time experimentally on frozen-hydrated biological samples. ZPP contamination, resulting charging artefacts and solution for these problems are presented. Furthermore the application of the ZPP with conventional electron optics and with a microscope containing a diffraction magnification unit and an aberration corrector is compared. From this new insights into the design and use of an obstruction free anamorphic phase plate (APP) can be gained.

Contents

List of Figures

List of Tables

Abbreviations

aCTF amplitude contrast transfer function

APP electrostatic anamorphic phase plate

BFP back focal plane

BPP electrostatic Beorsch phase plate

CTF contrast transfer function

cryo-TEM cryo transmission electron microscopy

DMU diffraction magnification unit

dZPP electrostatic double Zach phase plate

FIB focused ion beam

HRTEM high resolution transmission electron microscopy

KIT Karlsruher Institut für Technologie

NMR nuclear magnetic resonance spectroscopy

pCTF phase contrast transfer function

PP phase plate

PSF point spread function

SEM scanning electron microscopy

SNR signal to noise ratio

TEM transmission electron microscopy

WPO weak phase object

ZPP electrostatic Zach phase plate

1 Electrostatic phase plates for transmission electron microscopy

With cryo transmission electron microscopy (cryo-TEM) biological samples, such as purified proteins, helical filaments, whole cells or viruses can be imaged close to their native state by freezing them in vitreous ice and imaging them under cryo conditions [1]. Cryo-TEM of samples embedded as multiple single particles in vitreous ice allows three dimensional reconstruction and structure analysis of such objects. Three dimensional density maps of viral particles or proteins with resolution of around 3.5 - 5 Å [2–4] can now bridge the gap between resolutions achieved with light microscopy, which are several tens of nm [5] and X-ray crystallography or NMR (Nuclear magnetic resonance spectroscopy), which reach several Ångstrøm [6] of resolution.

1.1 Limitations of imaging biological samples with cryo-TEM

Ice embedded biological samples are considered as weak phase objects, giving rise to very low image contrast for such samples. This low image contrast originates from the low atomic mass of the sample and the surrounding ice. Due to this the transmitting electron wave contains almost no amplitude contrast, but almost all the sample information is encoded in the small phase shift or phase contrast of the exit wave. Furthermore ice embedded biological samples are very beam sensitive. Thus they have to be imaged at very low dose. The reachable resolution of the three dimensional reconstructions of these samples is constrained by the low image contrast or low signal to noise ratio (SNR) of the individual images. To achieve resolution in the sub-nanometer range for single particle reconstruction, hundreds of thousands up to a million of single particle images have to be aligned and averaged accurately. The resulting quality of these processing procedures and the resulting 3D reconstruction is strongly dependent of the contrast obtained in individual images.

In conventional cryo-TEM the low phase contrast of the samples is improved by defocusing the objective lens, using values of approximately 1 up to 6 µm. This method can still be

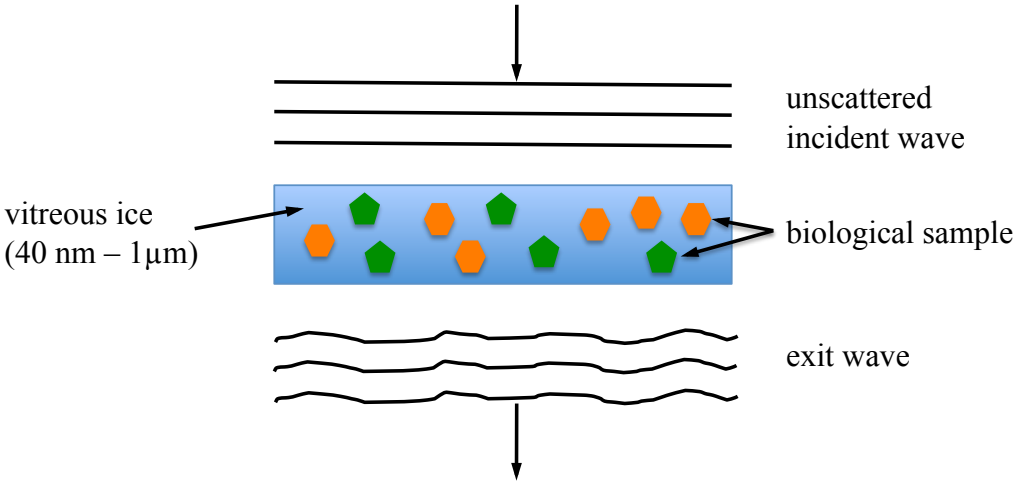

Figure 1.1: Schematic illustration of biological samples embedded in vitreous ice as used in cryo-TEM. Based on the low mass thickness of the atoms, the sample causes only little modulation in amplitude and phase for an incident plane wave. Thus the sample is classified as a weak phase object (WPO), meaning that image information is mainly encoded in the small phase shift of this exit wave.

used, as the physics of the image formation is well understood: The final images results from a convolution of the object wave function and the sinusoidal phase contrast transfer function (pCTF) [7], which also depends on the spherical aberration of the objective lens. However this defocusing technique has the disadvantage of causing decreasing contrast at low spatial frequencies and limited overall image resolution, as the information is more delocalised, and it produces a strongly oscillation of the pCTF resulting in a complete loss of information at the zeros of the function. Figure 1.2 shows an example of frozen-hydrated ribosomal 70S subunits. Figure 1.2 a) shows the marginal contrast of in-focus image acquisition. The corresponding Power Spectra* in figure 1.2 b) shows no oscillations in the contrast transfer. Figure 1.2 b) shows the enhanced contrast by image acquisition at 4.4 µm under-focus. The corresponding Power Spectra in figure 1.2 d) shows an increased number of oscillations in contrast transfer, which are called Thon rings† [9].

To overcome the restriction of low phase contrast transfer and the disadvantages of the defocusing technique, a device is needed that enables in-focus (a defocus of 0.0 µm) image acquisition with increased phase contrast. Boersch, for example, [10] proposed the use of physical phase plates for transmission electron microscopy (TEM). Similar to the already

* The term **Power Spectra** describes the square modulus of the Fourier transform of an image $\mathrm{PS}(\mathbf{r}) = \mathcal{F}^{-1}[\mathrm{I}(\mathbf{r})]$. This image shows the square modulus of the exit wave modulated by the contrast transfer function (CTF) [8].

† **Thon rings** are rings visible in the Power Spectra of images acquired with bright field electron microscopy. They denote the extreme point positions of the square modulus values of the CTF [9].

known $\lambda/4$ plates in light microscopy [11], these physical phase plates for TEM should induce a relative phase shift between scattered and unscattered electrons. Therefore the phase plates are inserted into the back focal plane (BFP) of the objective lens, where scattered and unscattered electrons are spatially separated. For producing the relative phase shift, he proposed e.g. to use the inner potential of a thin film or an electrostatic field. Due to the small dimensions that are mandatory to produce such phase plates for TEM, it took several decades until technical and engineering abilities had progressed far enough to enable Boersch's idea.

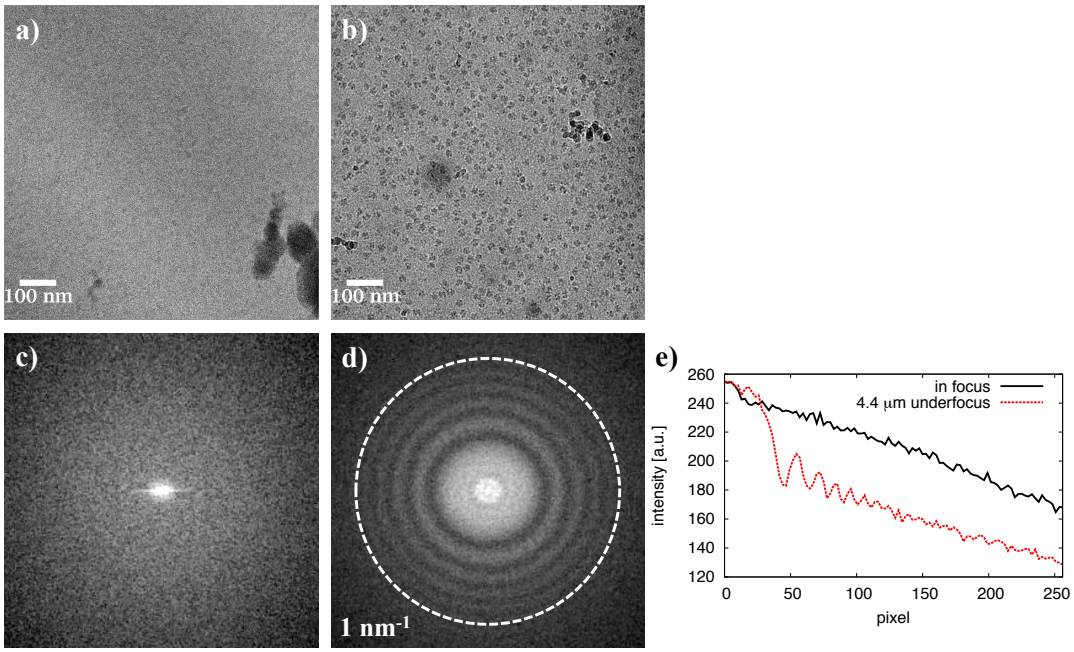

Figure 1.2: Images of frozen-hydrated ribosomal 70S subunits. a) shows the marginal contrast of an image taken in-focus ($\Delta f = 0.0$ nm). The center part of the corresponding Power Spectra is shown in c). No oscillations in contrast transfer are visible here. Compared to this, image b) shows the enhanced contrast by using a defocus value of 4.4 µm. d) shows the center part of the corresponding Power Spectra, with the increased number of oscillations in contrast transfer, which are called Thon rings. Radial line scans calculated from image c) and d) are shown in image e) as an illustration of the modulated contrast transfer. Note that this diagram shows the square of the absolute value of the contrast transfer function (CTF).

1.2 Phase plates for phase contrast enhancement in TEM

Since Boersch's proposal in 1947, several attempts to apply phase plates for TEM have been made [12,13]. However the first realization of a physical phase plate kept in use until today, was provided by the group of Nagayama [14]. It consist of a carbon film with a hole in the center and is called Zernike-type film phase plate. The name is related to Zernike's proposals for light microscopy [11]. The film is placed in the back focal plane (BFP) of the objective lens, where the unscattered electrons pass through the central hole and are not affected by the inner potential of the carbon film. However, the scattered electrons receive an additional phase shift of $\pi/2$ by passing the inner potential of the carbon film with a well-defined thickness. A second version of a film phase plate, called Hilbert film phase plate, was also proposed by the same group [15]. It consist of a carbon film covering only have of the diffraction plane and with double the thickness of a Zernike film phase plate. Hence one half of the scattered electrons experience an additional phase shift of π, whereas the other half and the unscattered electrons in the center remain unaffected. However the application of film phase plates shows that they suffer from drawbacks such as reduced resolution, contamination and uncontrolled charging.

To avoid these problems, other groups focused on the development of electrostatic phase plates. These phase plates with more complex design produce an electrostatic potential in the BFP of the objective lens or a conjugate plane to produce a relative phase shift of $\pi/2$ between scattered and unscatterd electrons. An electrostatic phase plate based on Boersch's original ideas, was proposed in 1996 by Matsumoto and Tonomura [16] as so called Boersch phase plate and was first realized and operated by Majorovits et al. and Schultheiss et al. [17, 18]. This phase plate consist of a five-layered annular electrostatic lens, supported by three radial bars. The unscattered electrons passing through this lens gain an additional relative phases shift of $\pi/2$. Furthermore Cambie et al. [19] presented a two-electrode phase-contrast element (drift tube) which is also suitable for phase contrast electron microscopy.

However, application of these phase plates showed that this design is limited in its usability due to its prohibitive obstruction of electrons, also known as spatial frequencies, by the supporting bars and the ring electrode. These obstructions lead to a loss of image information, which can only be partially recovered by utilizing Friedel* symmetry for weak phase objects in subsequent image processing steps.

* **Friedels law** goes back to Georges Friedel [20]. It means that a diffraction image of an object is always centrosymmetric. The object itself does not need to have any symmetry at all. Two centrosymmetric point in frequency space $P_1(q_x, q_y)$ and $P_2(q_x, q_y)$ are called Friedel pairs. They contain the same structure information about the object. This law is an attribute of Fourier transforms of real functions. The

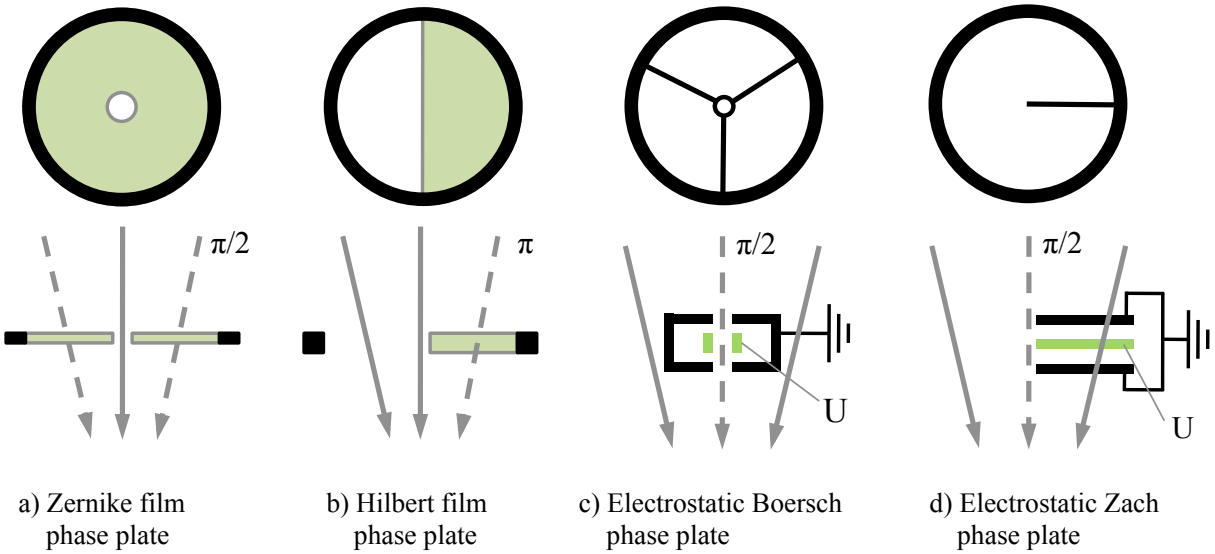

Figure 1.3: Illustration of typical examples for film and electrostatic phase plates. a) Zernike film phase plate consisting of a carbon film with hole in the center and thickness to produce a phase shift of $\pi/2$. b) Hilbert film phase plate consisting of a carbon film with covering a half plane with thickness to produce a phase shift of π. c) Electrostatic Boersch phase plate consisting of a central ring electrode supported by three radial bars. An electrostatic field is induced inside the ring electrode, to produce a phase shift of $\pi/2$. d) Electrostatic Zach phase plate consisting of one electrode rod with a structure like a coaxial cable. Again an electrostatic field is induced at the tip of the rod to produce a phase shift of $\pi/2$.

To overcome these problems of frequency obstruction, an obstruction-minimized design was proposed by Zach [21]. First manufacturing attempts and practical application for phase contrast imaging were shown by Schultheiss et al. [22]. In contrast to the Boersch phase plate, this Zach phase plate geometry is reduced by removing the ring electrode and two of the three supporting bars. The Zach phase plate therefore consists of a five-layered electrode with a layer organization comparable to a coaxial cable. It produces an anisotropic electrostatic field at the position of the unscattered electron beam and thus introduces a relative phase shift between the scattered and unscatterd electrons.
It needs to be noted, that the Zach phase plate is the first working phase plate which uses an inhomogeneous, anisotropic electrostatic potential distribution to induce the relative

---

function

$$F(q) = \int_{-\infty}^{\infty} f(x) e^{iqx} dx$$

has the property

$$F(q) = F^*(q).$$

$F^*(q)$ is the complex conjugate of $F(q)$.

phase shift. As we will discus lateron, it is therefore the model system for more advanced obstruction free phase plate designs, introduced in chapter 1.3.
Nevertheless also the Zach phase plate design still obstructs some spatial frequencies by its remaining electrode bar. At present a minimization of the bar is restricted to a width of approximately 1 µm due to technical limitations. The production of the Zach phase plates is done in collaboration with the Laboratory of Electron Microscopy at Karlsruher Institut für Technologie (KIT) and funded by DFG projects. For further minimization of spatial frequency obstructions the Zach phase plate is installed into an electron microscope with a diffraction magnification unit (DMU) instead of an electron microscope with conventional electron optics. This DMU provides an enlarged diffraction plane, whereas the minimal width of the phase plate bar remain constant. This minimizes the relative amount of obstructed spatial frequencies.

1.3 An ideal matter free electrostatic phase plate

The use of the electrostatic Zach phase plate in combination with a DMU minimizes the obstruction problem of spatial frequencies but still does not provide an optimal solution. An ideal electrostatic phase plate without any obstruction of spatial frequencies due to mechanical parts was proposed by Schröder [23]. For this, so called anamorphic phase plate a highly anamorphic* electron optics is needed, like provided in the ray path of aberration correctors. The anamorphic phase plate consists of a five layered structure, with four electrically contacted electrodes in the central layer, surrounded by two isolating layers and finally covered from the top and bottom side with two electrically shielding metal layers. Figure 1.4 shows a schematic illustration of the design of the central electrodes. The design consist of two rectangular, horseshoe-like looking electrodes and two electrode bars, arranged as a rectangle with interrupted boundary and a slit like opening in the center. These electrodes induce a highly anisotropic and inhomogeneous electrostatic potential in the central narrow slit aperture of this phase plate. For its application the whole diffraction image has to pass through this slit aperture and therefore needs to be compressed in one direction. Two operating modes are possible by applying different potential arrangements to the electrodes (figure 1.4 a) and b)):
1. Hilbert imaging mode: A phase shift of π for the left or right half-plane of spatial frequencies is induced, leaving the other half-plane unaffected. Here one of the two half-planes includes the zero order beam of unscattered electrons. The name arises due to sharing the same physical imaging formation properties as the Hilbert film phase plate.

* The term **anamorphic** means that the ray path inside the electron optics is elongated along one axes and compressed along the other perpendicular axes.

For this application only one anamorphic diffraction plane and corresponding anamorphic phase plate is needed.

2. Zernike imaging mode: Two anamorphic phase plates, oriented perpendicular to each other are needed. They are positioned in two different diffraction planes, which again both need to be anamorphic. Hence the diffraction image has to be compressed and stretched two times in perpendicular directions. Each phase plate produces a relative phase shift of $\pi/4$ for a central frequency band of scattered electrons but including the zero order beam. Both frequency bands are oriented perpendicular to each other. This leads to a total relative phase shift of $\pi/2$ for the zero order beam and two perpendicular frequency bands of scattered electrons with a phase shift of $\pi/4$.

Due to the need of highly anamorphic ray paths in diffraction planes, this anamorphic phase plate can be installed only into aberration corrector-like optical devices. Before an highly expensive instrumentation project can be started, it is therefore advisable to test the fundamental assumptions of the anamorphic system, meaning that also anisotropic and inhomogeneous potential distributions can be used as physical phase plates. To prove these assumptions, at least for the Zernike mode, a modification of the former introduced Zach phase plate can be used, together with electron microscopes providing conventional round electron optics. This model consists of two opposite electrode bars and is called electrostatic double Zach phase plate. It produces an inhomogeneous electrostatic potential at the zero order beam position, with comparable shape as the one produced by the anamorphic phase plate (figure 1.5).

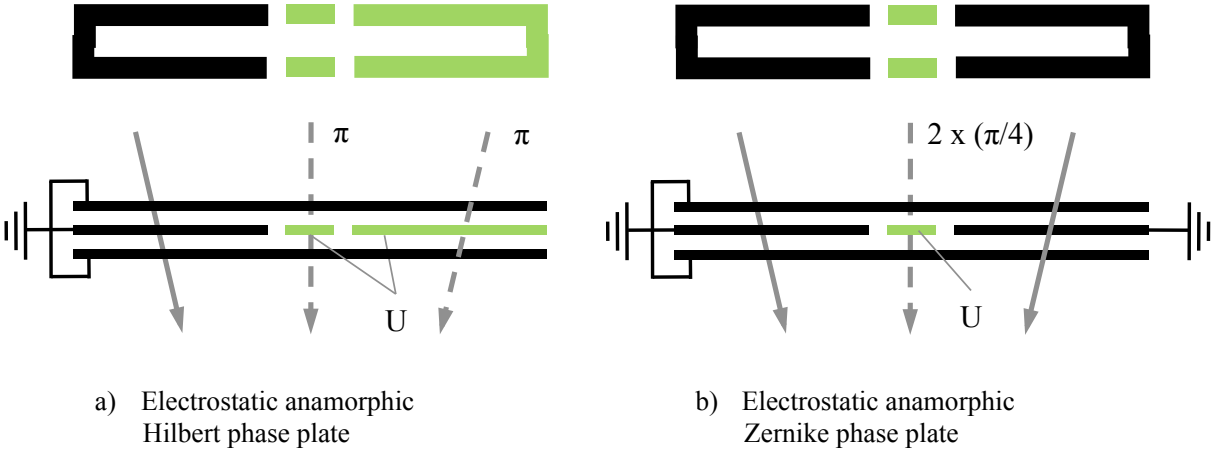

Figure 1.4: Illustration of electrostatic anamorphic phase plates, consisting of a five layered electrode structure. The ray path has to be compressed and stretched to fit into the slit like aperture. a) voltage configuration for Hilbert mode. A phase shift of π for one half plane of scattered electrons and for the zero order beam is induced. b)voltage configuration for Zernike working mode. A phase shift of $\pi/4$ for the zero order beam is induced. Two such phase plates perpendicular to each other have to be used for a total phase shift of $\pi/2$ for the zero order beam.

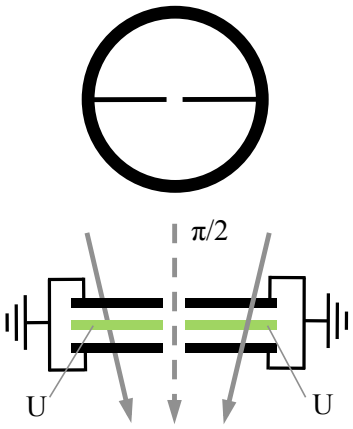

Figure 1.5: Illustration of electrostatic double-Zach phase plates, consisting of two opposite bars, each with a five layered electrode structure. The potential distribution at the zero order beam position is equal to the distribution in an anamorphic Zernike-type phase plate. Thus the double-Zach phase plate model can be used for preliminary test in an electron microscope with round electron optics.

1.4 Aims of the presented work

Since electron microscopes suitable for the application of anamorphic electrostatic phase plates are not jet available, first extensive research on anisotropic and inhomogeneous electrostatic phase plates usable for round electron optics need to be done. The most promising design refers to the electrostatic Zach phase plate, due to its minimized electron obstruction in the diffraction plane. First practical applications as prove of principal of the electrostatic Zach phase plate demonstrated that further optimization of the phase plate design is necessary. This implies its mechanical geometry to further minimize obstruction of spatial frequencies in the diffraction plane and to optimize the shape of the produced electrostatic potential. Furthermore its application to biological samples - especially on cryo samples - has to be proven. As next step in the application the design of the Zach phase plate should also be adapted for the use in TEM with a diffraction magnification unit (DMU) combined with an aberration corrector for spherical aberrations, as this provides a further minimization of spatial frequency obstruction. Here an optimal design regarding the shape of the produced electrostatic potential needs to be developed. The first practical application for phase contrast imaging using TEM with DMU needs to be shown. Likewise solutions for occurring problems during application need to be found. These are for example charging effects, which need to be minimized. The aim of this work is to study the advantages and disadvantages of the electrostatic Zach phase plate for electron microscopes with conventional electron optics and for electron microscopes with a diffraction magnification unit combined with an aberration corrector for spherical aberrations. Resulting from performed studies the following points are discussed in this thesis:

- What are the advantages or disadvantages of the electrostatic Zach phase plate?
- What are the advantages or disadvantages of a diffraction magnification unit for transmission electron microscopy?
- Can the Zach phase plate geometry be minimized in such a way, that invertible, in-focus phase contrast imaging for cryo samples with a conventional electron microscope is possible?
- How can unwanted single side band contrast be reduced?
- How has the geometry of the Zach phase plate to be changed or optimized for an application in TEM with DMU? Which are the additional, unwanted effects that occur due to the use of a DMU?

- How can these unwanted effects like charging of the phase plate structure be minimized? What are the reasons for these effects?
- How can the lifetime of such a Zach phase plate be extended?
- How would future developments of an ideal obstruction free anamorphic electrostatic phase plate look like? Which similarities to the Zach phase plate are given and how can future experiments look like?

2 Mechanism of contrast formation in TEM and options for contrast transfer improvement

In this chapter the fundamental concepts of image formation in TEM are described. The contrast in an image is produced by the interference of the amplitude and phase modulated scattered part of the incident electron wave with the corresponding unscattered electron wave part. Furthermore image formation is affected by the wave distortions due to the aberrations of the electron optical systems. In this context specimens consisting of light atoms such as biological samples show very low amplitude and phase contrast. To improve the image contrast for these kind of samples in a conventional electron microscope, the focal length of the objective lens can be modulated or phase plates can be used. Additional use of aberration correctors also improves the image contrast.

2.1 Formation of image contrast by electron-specimen interaction

For the interaction processes of the electron wave and the sample in TEM two scattering processes are distinguished, which are **elastic** and **inelastic** scattering. The elastic scattering of electrons by the Coulomb potential of a nucleus is the most important part that contributes to the image contrast formation. This image contrast occurs from the coherent interference of the unscattered incident electron wave and the scattered wave. For elastic scattered electrons there is no energy loss [24]. Inelastic scattered electrons with energy loss and thus incoherent interference of unscattered and scattered electron wave, is induced by the excitation of electrons in the sample into higher energy states. This can be for example the excitation of phonons or plasmons in solids. Likewise the production of ionisation states or Auger electrons also leads to inelastic scattering events. In the following section the interaction process of the incoming plane electron wave and the sample is described. As described in [7] the wave function of an electron wave after passing through a specimen can be written as

$$\Psi_s(\mathbf{r}) = \Psi_0 \left[1 - a_s(\mathbf{r})\right] \exp\left[i\varphi(\mathbf{r})\right] \tag{2.1}$$

Here Ψ_0 is the incoming unscattered plane wave, the vector $\mathbf{r}$ describes the radius vector in the specimen plane, $a_s(\mathbf{r})$ is the local decrease of amplitude and $\varphi(\mathbf{r})$ is the phase shift caused by the specimen.
Amplitude contrast described by the amplitude factor ($0 \leq a_s(\mathbf{r}) \leq 1$) arises from absorption in material. One possibility to increase amplitude contrast is to use an energy filter, which removes inelastic scattered electrons of a well defined energy width from the image. Another amplitude contrast mechanism is the absorption of electrons, which are scattered outside a given numerical aperture, by elastic high angle scattering or multiple scattering events. Here the electrons are filtered out by the obstruction of the objective aperture.
Phase contrast described by the factor $\varphi(\mathbf{r})$ is produced due to the different refractive index $n(\mathbf{r})$ for different atoms inside the sample. The refractive index $n(\mathbf{r})$ depends on the attractive Coulomb potential $V(\mathbf{r})$ of the atoms [7]. The induced phase shift $\varphi(\mathbf{r})$ of an exit wave after passing through a sample of thickness t is described by

$$\varphi(\mathbf{r}) = \frac{\pi}{\lambda E}\chi(U_0) \int_{-\frac{t}{2}}^{\frac{t}{2}} V(x, y, z)dz \tag{2.2}$$

Here λ is the wavelength of the electrons, E is the kinetic electron energy, $\chi(U_0)$ describes a relativistic constant. This relativistic constant is calculated by

$$\chi(U_0) = \frac{2(E_0 + E)}{(2E_0 + E)} \tag{2.3}$$

where E_0 is the rest energy of the electron.

2.2 Image contrast formation for weak phase objects

Samples that consist of elements with low atomic number Z, are called weak phase objects in TEM. This means that they show very small changes of phase and amplitude compared to the incoming plane wave and thus poor phase and amplitude contrast. Biological specimens are assigned to this group of samples as they consist mostly of light atoms like hydrogen, nitrogen, carbon or oxygen (H, N, C, O). It had been shown [7] that for such specimens the scattering amplitude and the total elastic cross-section decrease with smaller values of Z. Scattering events especially into large angles are very rare and most of the electrons pass unscattered through the sample, resulting in low amplitude contrast. Furthermore as described in equation 2.1 the induced phase shift is also very small, as it

depends on the Coulomb potential $V(\mathbf{r})$ and with this also from Z.
Due to the small amplitude factor ($0 \leq a_s(\mathbf{r}) \ll 1$) and small phase shift ($\varphi(\mathbf{r}) \ll 1$) equation 2.1 can be rewritten by using first a Taylor expansion for the term $\exp[i\varphi(\mathbf{r})] = 1 + i\varphi(\mathbf{r}) - \frac{\varphi(\mathbf{r})^2}{2} \pm \ldots$. This leads to the equation

$$\begin{aligned} \Psi_s(\mathbf{r}) &= \Psi_0[1 - a_s(\mathbf{r})]\exp[i\varphi(\mathbf{r})] \\ &= \Psi_0[1 - a_s(\mathbf{r})][1 + i\varphi(\mathbf{r}) \pm \ldots] \\ &\approx \Psi_0[1 - a_s(\mathbf{r}) + i\varphi(\mathbf{r})] \end{aligned} \tag{2.4}$$

whereby the term ($ia_s(\mathbf{r})\varphi(\mathbf{r}) \ll 1$) is neglected.
This formulation is known as the weak phase approximation [7]. In this equation the exit wave is described as a superposition of the unscattered incident wave Ψ_0 and the scattered wave $\Psi_0[a(\mathbf{r}) + i\varphi(\mathbf{r})]$. If now the small amplitude factor is also neglected ($a_s(\mathbf{r}) \approx 0$) the exit wave function is given by

$$\begin{aligned} \Psi_s(\mathbf{r}) &= \Psi_0 + i\Psi_0\varphi(\mathbf{r}) \\ &= \Psi_0 + i\Psi_{sc}(\mathbf{r}) \end{aligned} \tag{2.5}$$

with $\Psi_{sc}(\mathbf{r}) = \Psi_0\varphi(\mathbf{r})$.
Equation 2.5 implies that the relative phase shift between an unscattered and a scattered wave is given in a first approximation by a factor of $\pi/2$. This is indicated by the factor i. This relationship between scattered and unscattered electron wave can be well illustrated in a complex vector diagram in imaginary space. Here the amplitude of the unscattered wave is described by the vector Ψ_0 and the amplitude of the scattered wave is described by the vector Ψ_{sc}. The relative phase shift of $\pi/2$ between these two parts is then described by the vector $\Psi_0 + i\Psi_{sc}$. Figure 2.1 a) shows that the resulting amplitude is almost equal in length with respect to the amplitude of the unscattered wave Ψ_0, if $\Psi_{sc} \ll \Psi_0$, which hold for weak phase objects. With regard to the visible intensity, which can be described as the square of the absolute value of these amplitude vectors, it can be said that they are almost equal for the incoming unscattered wave and the resulting wave. This results in an almost invisible object contrast [7]. To increase the amount of phase contrast an additional phase shift of $\pm\pi/2$ has to induced to the amplitude vector of the scattered wave. Figure 2.1 b) and c) show the vector diagram illustrations of the resulting increased positive and negative phase contrast, respectively for an additional phase shift of $+\pi/2$ and $-\pi/2$.
This additional phase shift to the scattered electron wave is induced by the aberrations of

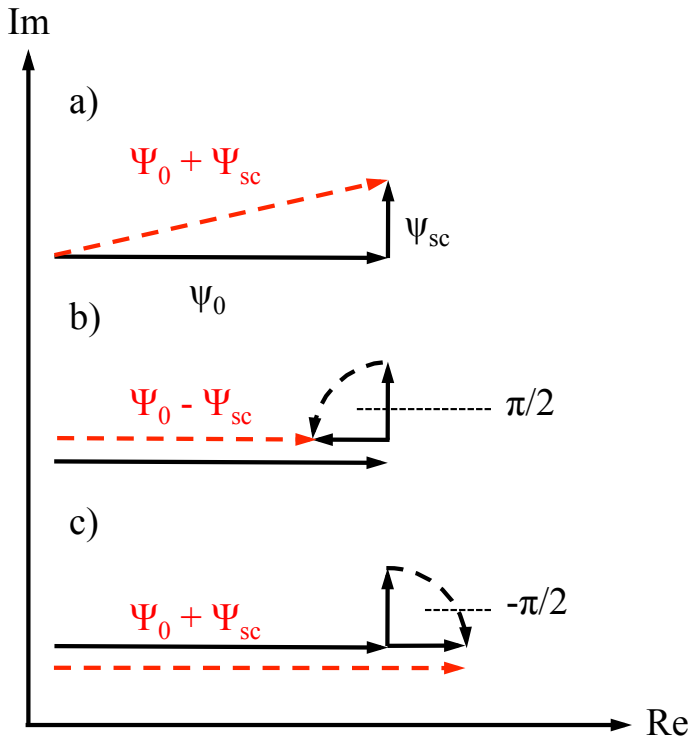

Figure 2.1: Schematic representation of wave amplitude vector diagrams of weak phase objects. The amplitudes of the unscattered and scattered part of the electron wave are represented by Ψ_0 and Ψ_{sc}. a) The amplitudes Ψ_0 and Ψ_{sc} are phase shifted by $\pi/2$. This results in a very low phase contrast. An improved phase contrast can be induced by an additional phase shift of $\pm\pi/2$, which results in b) positive phase contrast for a phase shift of $+\pi/2$ and c) negative phase contrast for a phase shift of $-\pi/2$.

the objective lens. Another possibility is to gain the additional phase shift by presenting an electrostatic potential in the back focal plane of the objective lens by using phase plates. The influence of the electron optical wave aberrations on the image formation is described in the following section. Subsequently the use of physical phase plates and their influence on image formation is discussed.

2.3 Influence of wave aberrations on image formation

In the electron optical system of a transmission electron microscope the exit electron wave of the sample is affected by several aberrations of the electron optical lenses. These aberrations can be classified into isotropic and anisotropic aberrations. However the defocus Δz of the objective lens, its spherical aberration C_S and chromatic aberration C_C are the major factors affecting image formation, whereas higher order aberration show a minor influence. Therefore only these three aberrations are considered in the following.

The defocus Δz of the objective lens describes a reduction or elongation of the focal length with regard to its nominal value. The spherical aberration C_{S} of an electron optical lens induces a shorter focal length for electrons passing through the lens with large lateral distance to the optical axis. The chromatic aberration C_{C} arises from the objective lens, since electrons of different energy are focused in different planes. Reasons for energy dispersion of the illumination can be an instability of the acceleration voltage, the energy spread of the electron gun of the microscope or energy loss of the electrons by interactions with the sample [7].

As an effect of these aberrations on the image formation, an object point P is not exactly imaged into an image point P' but it is blurred and imaged as an Airy disc. This influence on the wave amplitude $\Psi_{\mathrm{m}}(\mathbf{r}')$ at point P', coming from point P as wave amplitude $\Psi_{\mathrm{s}}(\mathbf{r})$, is described by the point spread function (PSF) $h\,(\mathbf{r})$ [7, 24].

$$\begin{aligned} \Psi_{\mathrm{m}}(\mathbf{r}') &= \int \Psi_{\mathrm{s}}(\mathbf{r}) h(\mathbf{r}' - \mathbf{r}) d\mathbf{r} \\ &= \Psi_{\mathrm{s}}(\mathbf{r}) \otimes h(\mathbf{r}) \end{aligned} \tag{2.6}$$

If now the convolution theorem is applied, equation 2.6 can be written as a multiplication in frequency space instead of a convolution in real space.

$$\Psi_{\mathrm{m}}(\mathbf{q}') = \Psi_{\mathrm{s}}(\mathbf{q}) H(\mathbf{q}) \tag{2.7}$$

Here $\Psi_{\mathrm{m}}(\mathbf{q}')$, $\Psi_{\mathrm{s}}(\mathbf{q})$ and $H(\mathbf{q})$ are the Fourier transform of $\Psi_{\mathrm{m}}(\mathbf{r}')$, $\Psi_{\mathrm{s}}(\mathbf{r})$ and $h(\mathbf{r})$. The vector $\mathbf{q}$ denotes the spacial frequency in frequency space. $H(\mathbf{q})$ is the so called pupil function, which consists of the following terms.

$$H(\mathbf{q}) = e^{-iW(\mathbf{q})} M(\mathbf{q}) E(\mathbf{q}) \tag{2.8}$$

The factor $M(\mathbf{q})$ is a masking function describing the absorption of electrons by the objective aperture, if their scattering angle is larger then a maximum scattering angle $\Theta_{\max} = \alpha_0$. This maximum scattering angle corresponds to a maximal spatial frequency $q_{\max} =\mid \mathbf{q}_{\max} \mid$ in the back focal plane of the objective lens. Figure 2.2 shows that for scattering angles in the mrad range, which are typical in TEM, this maximal spatial frequency is expressed by $q_{\max} = {}^{r}/_{f\lambda}$. Here r denotes the radius of the objective aperture, f is the focal length of the objective lens and λ the electron wave length. The masking function has the values

$$\begin{aligned} M(\mathbf{q}) &= 1 \quad \text{for} \quad |\,\mathbf{q}\,| < q_{\max} \\ &= 0 \quad \text{for} \quad |\,\mathbf{q}\,| > q_{\max} \end{aligned} \tag{2.9}$$

in the normal bright field mode.

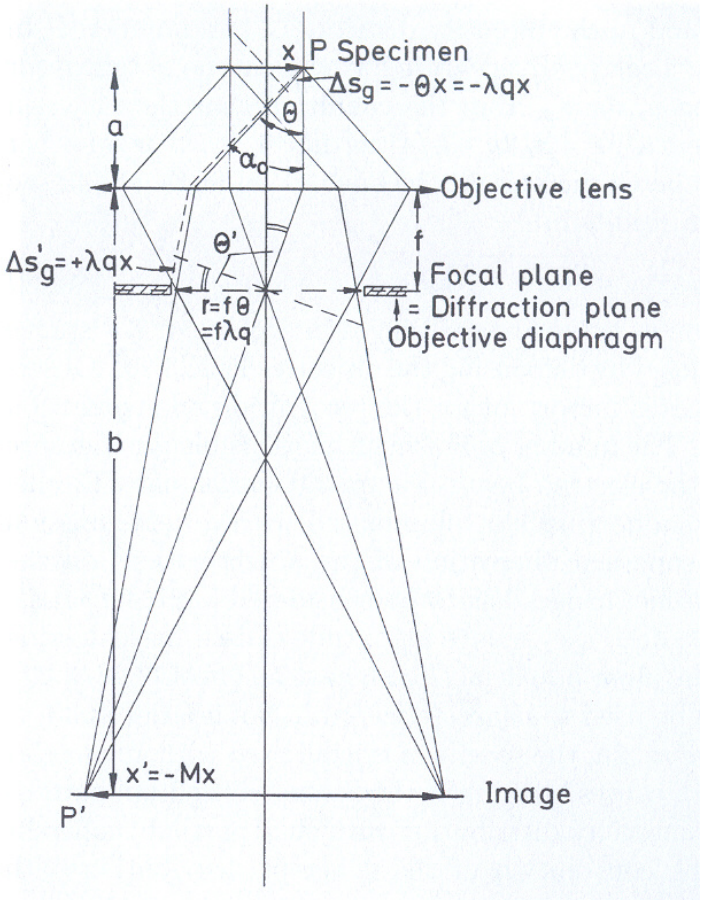

Figure 2.2: Ray diagram for image formation by an objective lens. Image taken from [7].

The factor $E(\mathbf{q})$ denotes envelope functions with damping effects on the exit wave induced by the variation of the electron energy, including chromatic aberration and illumination apertures. This is distinguished by two contributing terms.

$$E(\mathbf{q}) = K_{\mathrm{C}}\,(\mathbf{q})\,K_{\mathrm{S}}\,(\mathbf{q}) \tag{2.10}$$

with

$$K_{\mathrm{C}}(\mathbf{q}) = \exp\left[-\left(\frac{\pi\lambda\mathbf{q}^2}{4\sqrt{\ln 2}}C_{\mathrm{C}}\frac{\Delta E}{E}\frac{1+E/E_0}{1+E/2E_0}\right)^2\right] \tag{2.11}$$

marking the chromatic aberration envelope and

$$K_{\mathrm{S}}(\mathbf{q}) = \exp\left[-\frac{(\pi C_{\mathrm{S}}\lambda^2\mathbf{q}^3 - \pi\Delta z\mathbf{q})^2\alpha_{\mathrm{i}}^2}{\ln 2}\right]. \tag{2.12}$$

labelling the spatial coherence envelope. In equation 2.11 E is the electron energy, ΔE is the variation in electron energy, E_0 the rest energy of the electron and C_{C} is the chromatic aberration. Due to the finite size of the electron source the emitted electrons do not form an exactly parallel beam but the beam is spread by an aperture angle. This illumination aperture is described by α_{i} in equation 2.12.

The factor $e^{-iW(\mathbf{q})}$ describes the influence of the objective lens aberrations. These aberrations cause an additional phase shift to the exit wave and is described by the aberration function

$$W(\mathbf{q}) = \frac{\pi}{2}\left(C_{\mathrm{S}}\lambda^3\mathbf{q}^4 + 2\Delta z\lambda\mathbf{q}^2\right) \tag{2.13}$$

Here $\mathbf{q}$ is the spatial frequency, λ the electron wave length, C_{S} the spherical aberration and Δz the defocus value.

The image intensity $I(\mathbf{r}') =\mid \Psi_{\mathrm{m}}(\mathbf{r}') \mid^2$ for the weak phase object is now calculated by using equations 2.7 and 2.4, considering the just described additional phase shift factor $e^{-iW(\mathbf{q})}$ but neglecting the envelope function. Ψ_0 is set to the value one.

$$\begin{aligned}
\Psi_{\mathrm{m}}(\mathbf{q}') &= \Psi_{\mathrm{s}}(\mathbf{q})H(\mathbf{q}) \\
&= [1 - a_{\mathrm{s}}(\mathbf{q}) + i\varphi(\mathbf{q})]\, e^{-iW(\mathbf{q})} \\
&= [1 - a_{\mathrm{s}}(\mathbf{q}) + i\varphi(\mathbf{q})]\,[\cos(W(\mathbf{q})) - i\sin(W(\mathbf{q}))]
\end{aligned} \tag{2.14}$$

By using Fourier transformation, the relation $I(\mathbf{r}') =\mid \Psi_{\mathrm{m}}(\mathbf{r}') \mid^2$ and neglecting non symmetric contributions the image intensity becomes

$$I(\mathbf{r}') = 1 + 2\mathcal{F}^{-1}\left[-\cos W(\mathbf{q})a_{\mathrm{s}}(\mathbf{q}) + \sin W(\mathbf{q})\varphi(\mathbf{q})\right]. \tag{2.15}$$

The term with the factor $a_{\mathrm{s}}(\mathbf{q})$ describes the amplitude contrast transfer function (aCTF):

$$\begin{aligned}
\mathrm{aCTF}(\mathbf{q}) &= \cos W(\mathbf{q}) \\
&= \cos(\frac{\pi}{2}\left(C_{\mathrm{S}}\lambda^3\mathbf{q}^4 + 2\Delta z\lambda\mathbf{q}^2\right))
\end{aligned} \tag{2.16}$$

Furthermore the term with the factor $\varphi(\mathbf{q})$ describes the phase contrast transfer function (pCTF):

$$\begin{aligned} \mathrm{pCTF}(\mathbf{q}) &= \sin W(\mathbf{q}) \\ &= \sin(\frac{\pi}{2}\left(C_s\lambda^3\mathbf{q}^4 + 2\Delta z\lambda\mathbf{q}^2\right)) \end{aligned} \tag{2.17}$$

2.4 Optimizing image contrast by utilizing Scherzer Defocus

Due to the small amplitude contrast for weak phase objects, the influence of the aCTF is marginal for the image formation compared to the modulation of the pCTF. As can be seen from equation 2.17 the three variable quantities in the formula describing the pCTF are the electron wavelength λ, the defocus value Δz and the spherical aberration C_S. The wavelength λ can now be assumed as fixed value, as during an operation session of the microscope, the acceleration voltage and with this the electron wavelength, is not altered. In a conventional TEM without a C_S - corrector also the value of the spherical aberration is a fixed value. This means that in practice the defocus value Δz is the only factor that can be varied. The sinusoidal pCTF has a number of zeros depending on the values of λ, C_S and Δz. Here the pCTF acts like a filter as there is no contrast transfer for the spatial frequencies at these zero points. A second consequence of this sinusoidal is also a contrast transfer with varying sign for certain frequency bands. By varying the defocus Δz an optimal value can be found to maximize the width of the transfer band without zeros for spatial frequencies. For a perfect lens with $C_S = 0.0$ mm, this would be $\Delta z = 0.0$ mm. But in reality where $C_S \neq 0.0$ mm in a conventional transmission electron microscope, this optimal value can be calculated to

$$\Delta f_\mathrm{Sch} = -1.2(C_\mathrm{S}\lambda)^{\frac{1}{2}}. \tag{2.18}$$

This value is known as the Scherzer defocus Δf_Sch [24]. At this defocus value the pCTF shows an almost constant transfer band for spatial frequencies up to the first zero, as can be seen in figure 2.3. The first zero for the applied Scherzer defocus is defined as the instrumental resolution limit. This characterizes the limit up to which image information is transferred with equal contrast transfer in sign and with this gives interpretable image information without using further image processing.
The corresponding spatial frequency can be calculated by using

$$q_\mathrm{Sch} = 1.51(C_\mathrm{S}\lambda^3)^{-\frac{1}{4}}. \tag{2.19}$$

The resolution at Scherzer defocus is then defined by the reciprocal value of q_Sch.

$$r_{\mathrm{Sch}} = \frac{1}{1.51}(C_{\mathrm{S}}\lambda^3)^{\frac{1}{4}}. \tag{2.20}$$

The application of the Scherzer defocus works very well for high resolution TEM (HRTEM), where the spatial frequencies of the small objects lie in the transfer band of pCTF, for typical acceleration voltages and C_S values. But when imaging biological specimens the size of the objects often exceeds the range for which their spatial frequencies are still covered by the Scherzer defocus transfer band. This is shown in figure 2.3, solid line. Instead these objects have smaller spatial frequencies which are only transferred very weakly due to the sinusoidal shape for small frequencies of the pCTF. Much higher defocus values in the micrometer range have to be applied to this samples to induce a usable image contrast at lower spatial frequencies. This is shown in figure 2.3, dashed line. In comparison the Scherzer defocus for a conventional transmission electron microscope operated at an acceleration voltages at 200 keV (electron wave length $\lambda = 2.51$ pm) with a spherical aberration of $C_S = 2.2$ mm has a value of $\Delta f_{Sch} = 89.2$ nm. These chosen values for the acceleration voltage and spherical aberration are typical specification values as hold for the Zeiss EFTEM 912, which is one of the microscopes used for the experimental results presented in this work. Figure 2.3 demonstrates how the Scherzer defocus and a typical values of $\Delta z = -1000$ nm for Cryo-TEM influence the pCTF for $\lambda = 2.51$ pm and $C_S = 2.2$ mm.

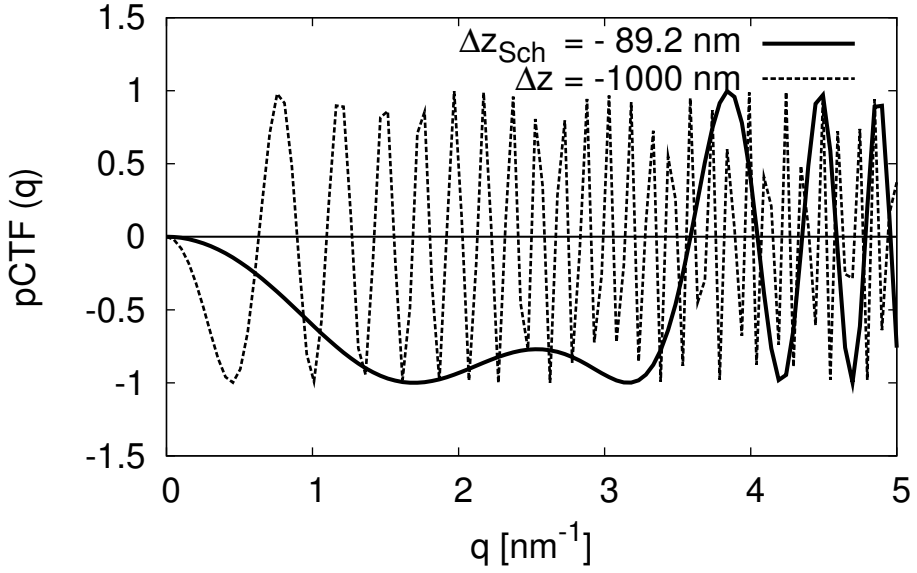

Figure 2.3: Comparison of pCTFs for an conventional microscope with spherical aberration $C_S = 2.2$ mm, without phase plate, operated at 200 keV (electron wave length $\lambda = 2.51$ pm). Shown are the pCTF at Scherzer defocus $\Delta f_{Sch} = -89.2$ nm (solid line) and the pCTF at a defocus value of $\Delta z = -1000$ nm (dashed line). Δf_{Sch} provides a large transfer band for spatial frequencies up to the first zero at $q_{Sch} = 3.6$ nm^{-1}, marking the instrumental resolution limit. Otherwise for small spatial frequencies up to approx. 0.7 nm^{-1} the transfer values are still low. The high defocus value of $\Delta z = -1000$ nm typical for Cryo-TEM images causes a strong oscillation of the pCTF but provides high transmission values for small spatial frequencies between approx. (0.3 - 0.6) nm^{-1}. Using defocus series an even larger band in the low spatial frequency range can by utilized.

2.5 Optimizing contrast transfer by correcting spherical aberrations

In a conventional transmission electron microscope every optical element producing a rotational symmetric electromagnetic field that acts as a lens is affected by lens aberrations. This statement was already proven by Scherzer in 1936 [25]. On the other hand Scherzer also proposed to use non-rotational symmetric optical elements in TEM for the correction of lens aberrations. To correct for the spherical aberration a combination of two hexapoles and two transfer lens doublets is needed. In 1998 the application of the first spherical aberration corrected transmission electron was reported by Uhlemann and Haider [26]. The corrector implemented in this project was describe in 1990 by Rose [27].
As described by Lentzen et al. [28] the point resolution at Scherzer Defocus can be ex-

tended by reducing the value of C_S. Since an extension of this point resolution is only reasonable up to the information limit of the microscope, the optimal values for spherical aberration and corresponding defocus are given by

$$C_{\mathrm{Sch,Opt}} = \frac{16}{3}\frac{1}{\lambda^3 q_{\mathrm{inf}}^4} \tag{2.21}$$

$$\Delta z_{\mathrm{Opt,C_S}} = -\frac{8}{3}\frac{1}{\lambda q_{\mathrm{inf}}^2} \tag{2.22}$$

where q_{inf} is the spatial frequency of the information limit. This optimal defocus value $\Delta z_{\mathrm{Opt,C_S}}$ is called Lentzen defocus. The information limit of the microscope is defined by the spatial frequency where the contrast transfer has dropped down to a value of $e^{-1/2}$. This damping of the pCTF is caused by the limited coherence of the electron wave, described by the chromatic envelope $K_C(\mathbf{q})$ and the spatial coherence envelope $K_S(\mathbf{q})$ introduced in chapter 2.3.
In spite of the improved transfer band for medium and high spatial resolution, specimen details at low resolution are still transferred with low contrast, as can be seen in figure 2.5 (dashed line). To overcome this problem an additional electron optical device to increase low spatial frequency phase contrast is needed. This means that a physical phase plate is advisable in a corrected system if a wide transfer spatial frequency band is desirable.

2.6 Optimizing contrast transfer by using physical phase plates

The use of physical phase plates in phase contrast TEM affects the possibility to obtain a constant transfer band for spatial frequencies in the pCTF with maximal extension, including small frequencies as well as frequencies up to the information limit of the microscope. Preferably this constant transfer band is thus independent of spatial frequencies.
As already described in chapter 2.4 and 2.5 an enlarged transfer band for spatial frequencies can be produced to a certain extend by the spherical aberration of the objective lens and by utilizing Scherzer defocus or when using Lentzen defocus. A third possibility to optimize the shape of this transfer band is utilized by applying physical phase plates. These physical phase plates have to be inserted into the back focal plane of the objective lens or a conjugate plane. Due to the spatial separation of the unscattered and the scattered part of the electron wave in these planes the phase plates provide the possibility to induce a relative phase shift between these two parts of the waves. Figure 2.4 shows the ray diagram of the electron wave through the sample, the objective lens and the position where the phase plates are inserted.

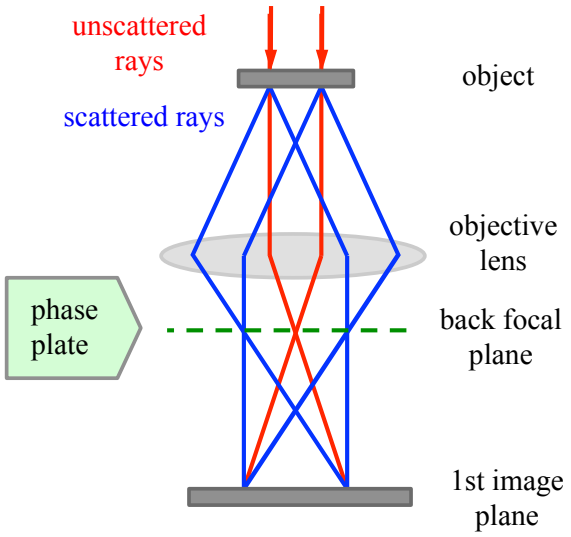

Figure 2.4: Ray diagram of unscattered and scattered electrons in a transmission electron microscope between the sample and the back focal plane (BFP) of the objective lens. Unscattered electrons are focused by the objective lens into the zero order beam position in the center of its BFP. Scattered electrons are focused with a radial distance to this zero order beam. Due to this spatial separation, this plane can be used for the installation of phase plates, inducing an additional relative phase shift between scattered and unscattered electrons.

For an improvement in phase contrast only a relative phase shift between the scattered and the unscattered part of the electron wave is important. Therefore it is insignificant if the additional phase shift is applied to the unscattered or the scatted part of the electron wave. In the aberration function $W(\mathbf{q})$ this additional phase shift by a phase plate is described by adding a factor ϕ_{PP}.

$$W_{\mathrm{PP}}(\mathbf{q}) = \frac{\pi}{2}\left(C_{\mathrm{S}}\lambda^3\mathbf{q}^4 + 2\Delta z\lambda\mathbf{q}^2\right) + \phi_{\mathrm{PP}} \tag{2.23}$$

By applying an additional phase shift of $\phi_{\mathrm{PP}} = \pm\pi/2$ the contrast transfer function for a weak phase object with a former sinusoidal shape is transferred to a function with cosine functionality:

$$\begin{aligned} \mathrm{pCTF}_{\mathrm{PP}}(\mathbf{q}) &= \sin(\frac{\pi}{2}\left(C_{\mathrm{S}}\lambda^3\mathbf{q}^4 + 2\Delta z\lambda\mathbf{q}^2\right) + \phi_{\mathrm{PP}}) \\ &= \pm\cos(\frac{\pi}{2}\left(C_{\mathrm{S}}\lambda^3\mathbf{q}^4 + 2\Delta z\lambda\mathbf{q}^2\right) \end{aligned} \tag{2.24}$$

This change to a cosine function already optimizes the contrast transfer for small spatial frequencies.

2.6.1 Phase plate without C_S correction

If such a phase plate is used in a microscope without the possibility of C_S correction, the defocus value for an optimized transfer band is given by

$$\Delta z_{\mathrm{Opt,PP}} = -0.73(C_S\lambda)^{\frac{1}{2}}. \tag{2.25}$$

This value was assigned by [29] using Scherzers criteria. The corresponding resolution limit in spatial frequencies for this defocus value is calculated by

$$q_{\mathrm{Opt,PP}} = 1.4(C_S\lambda^3)^{-\frac{1}{4}}. \tag{2.26}$$

By comparing equation 2.26 with equation 2.19, it becomes clear that the resolution of the microscope slightly decreased at this optimal defocus value. On the other hand the transfer of low spatial frequencies is highly improved. A schematic illustration of such transfer functions is shown in figure 2.5 as solid line.

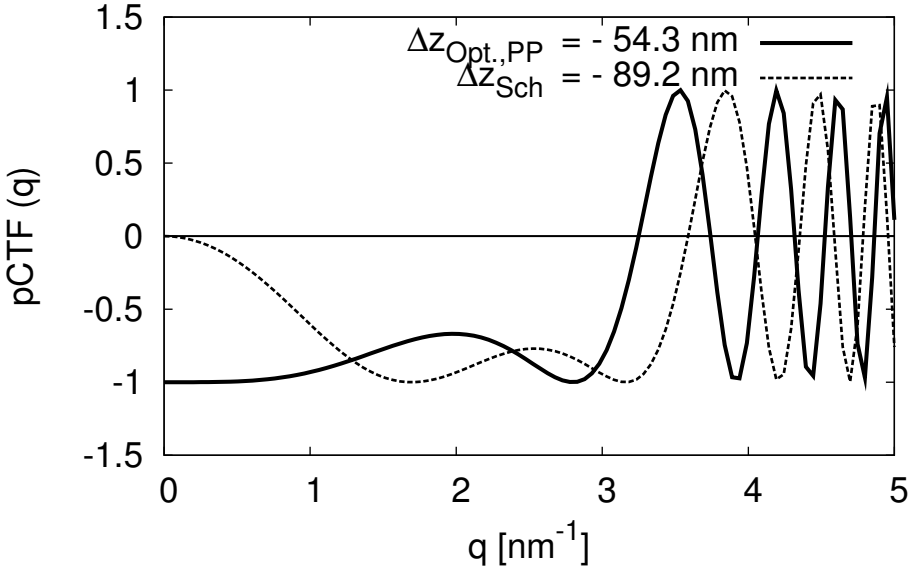

Figure 2.5: Comparison of pCTF for a conventional microscope operated at 200 keV without C_S corrector. Shown are the pCTF with phase plate and optimal chosen defocus value of $\Delta z_{\mathrm{Opt,PP}} = -54.3$ nm (solid line) and the pCTF without phase plate at Scherzer defocus $\Delta z_{Sch} = -89.2$ nm (dashed line). By using a phase plate with the optimal defocus value, contrast transfer is reduced slightly for high spatial frequencies but is significantly improved at low spatial frequencies.

2.6.2 Phase plate with C_S correction

When the phase plate is used in a microscope with a C_S - corrector, the optimal values for defocus and spherical aberration would be $\Delta z = 0.0$ mm and $C_S = 0.0$ mm. With these values and a phase shift of $\phi_{PP} = \pi/2$ by the phase plate, the pCTF becomes a constant function with value one. The contrast transfer is now independent of the spatial frequencies.

$$\begin{aligned} \mathrm{pCTF}_{\mathrm{PP},\Delta z,C_S}(\mathbf{q}) &= \sin(0 + \phi_{PP}) \\ &= \pm 1 \end{aligned} \tag{2.27}$$

In a realistic application the values for Δz, C_S and ϕ_{PP} can only be set to zero or rather $\pi/2$ with a certain error or defocus spread, if an extended object is assumed. For these conditions the optimal contrast transfer band, with an additional phase shift of $\phi_{PP} = \pm\pi/2$ is given by

$$\Delta z_{\mathrm{PP},C_S} = -\frac{1}{2} C_S \lambda^2 q_{\mathrm{inf}}^2 \tag{2.28}$$

for $\Delta z_{\mathrm{PP},C_S}$ and C_S having opposite signs, as described in [30]. Here q_{inf}^2 describes the frequency of the information limit, where the pCTF drops down to a value of $e^{-1/2}$ due to the envelope functions for chromatic aberration and spatial coherence as described in section 2.3. For this defocus value the first maximum of the pCTF is at the spatial frequency $q_1 = 0$ nm, whereas the second maximum of the pCTF is coincident with the information limit

$$q_{\mathrm{PP},C_S} = \sqrt{\frac{-2\Delta z_{\mathrm{PP},C_S}}{C_S \lambda^2}}. \tag{2.29}$$

Due to experiences during experimental application of phase plate work in a C_S corrected microscope (Zeiss Libra 200 DMU) described in this work, a realistic value for C_S after correction is about 5 µm. Figure 2.6 shows the pCTF for a microscope operated at 200 keV with such a $C_S = 5$ µm and applied phase plate in comparison to the pCTF for a microscope at 200 keV with C_S corrector, without phase plate but with optimal chosen values C_S and Δz, as described in section 2.5.

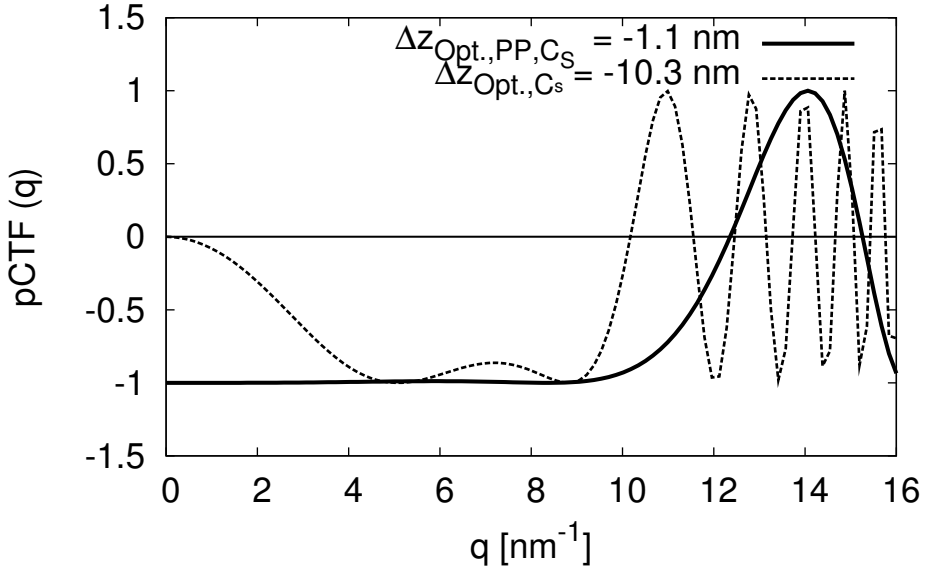

Figure 2.6: Comparison of pCTF for a microscope with C_S corrector operated at 200 keV. Shown are the pCTF with phase plate at optimal defocus $\Delta z_{\mathrm{Opt,PP,C_S}} = -1.1$ nm (solid line) versus the pCTF without phase plate and optimal chosen defocus value of $\Delta z_{\mathrm{Opt,C_S}} = -10.3$ nm (dashed line). By using a phase plate with the optimal defocus value, contrast transfer is increased for high spatial frequencies as well as for low spatial frequencies.

2.7 Optimizing contrast transfer by applying a diffraction magnification unit

Until now in all chapters an ideal phase plate was assumed. This means that the additional relative phase shift of $\pm\pi/2$ produced by the phase plate influences the whole range of spatial frequencies of the pCTF. In fact for very small spatial frequencies all phase plates do not only shift the phase of the zero order beam of unscattered electrons but also scattered electrons in the close vicinity of the zero order beam are phase shifted by a certain amount. Therefore the relative phase shift between these scattered and unscattered electrons is also smaller than $\pm\pi/2$ and the resulting values of the pCTF for the contrast transfer of the associated spatial frequencies are smaller than one. Other phase plates like the Boersch phase plate do even obstruct whole bands of spatial frequencies due to their obstructing annular lens electrode. For these spatial frequencies the transfer function has even vanishing information transfer. The spatial frequencies from which on the pCTF shows an ideal contrast transfer with value of one is called the "cut-on frequency" of the phase plate [31]. The exact value of this cut-on frequency is especially important when

imaging larger objects with low spatial frequencies. In structural biology this can be - for example - cell constituents like ribosomes or actin filaments with object sizes of a few 10 nanometers. The constituent spatial frequencies are of the order of values below 0.1 nm^{-1}.

There are basically two possibilities to reduce the value of this cut-on frequency. The first one is to minimize the geometry of the phase plate structures, to reduce the size of the area in the vicinity of the zero order beam where scattered electrons gain the same or similar relative phase shift as the unscattered ones. If a phase plate is applied in a conventional electron microscope this is the only possibility to reduce the cut-on frequency. The second possibility is to magnify the diffraction plane where the phase plate is inserted, which reduces any obstruction in the diffraction plane by a given phase plate structure. This can be done by increasing the focal length of the objective lens and by modifying the microscope and applying a diffraction magnification unit (DMU). This additional electron optical element, magnifies a conjugate plane of the back focal plane of the objective lens. This magnification minimizes the obstruction of spatial frequencies by the given phase plate structures. Furthermore it reduces the band width of spatial frequencies for scattered electrons with an similar or equal relative phase shift as the zero order beam. In such a microscope the phase plate is inserted in this magnified diffraction plane, rather than into the back focal plane of the objective lens.

The DMU element consists only of one round lens, the diffraction magnification lens (DML) [32, 33]. Because of additional aberrations by this lens, this DMU element can only reasonably be used in an electron microscope together with an C_S corrector. The last lens of the C_S corrector, the adaption lens (ADL), and the DML form together a telescopic magnification system. This system magnifies the back focal plane of the objective lens into the plane of the DML, where the phase plate is inserted [32,33]. The ADL magnifies both the image of the sample into a first intermediate image plane and the back focal plane of the objective lens into the second diffraction plane inside the DML. The DML images the first intermediate image into the entrance image plane of the first projective lens without any further magnification [32,33]. Figure 2.7 shows the ray path through the objective lens in a conventional microscope with the appropriate phase plate position and the ray path through a microscope with a DMU and appropriate phase plate position.

For the experimental results presented in this work two microscopes where used. The Zeiss EFTEM 923 with conventional electron optics and an objective focal length of $f = 2.7$ mm and the Zeiss Libra 200 DMU (KRONOS) with a objective focal length of $f = 4.6$ mm. With the increased focal length and the additional magnification factor of 3.6x due to the DMU, a total magnification of a factor 6.1x of the diffraction plane is obtained for the Zeiss Libra 200 DMU compared to the Zeiss EFTEM 923.

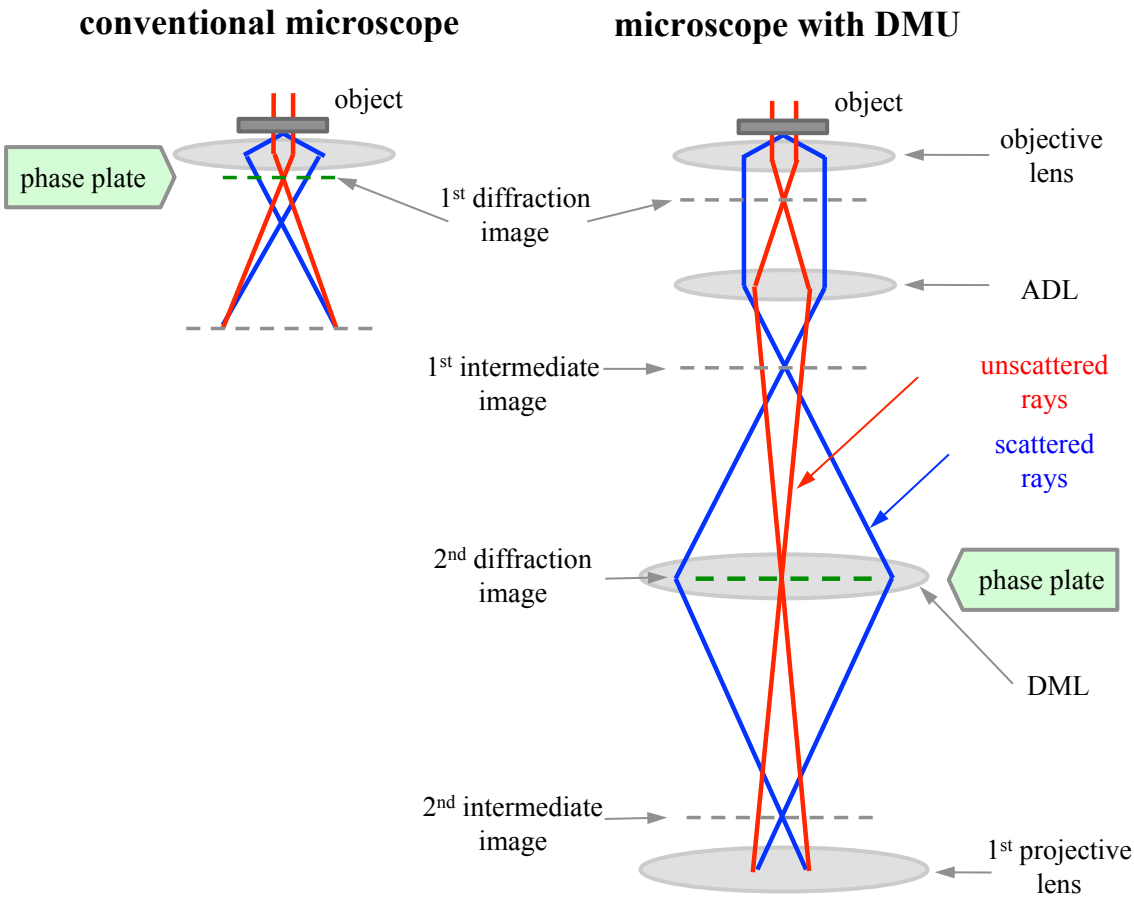

Figure 2.7: Comparison of the ray path of scattered and unscattered electrons in an conventional microscope and a microscope with a diffraction magnification unit (DMU). For both types the plane for inserting a phase plate are indicated. A microscope with DMU provides a magnified diffraction plane for the application of a phase plate. Thus obstructions of spatial frequencies and the cut-on frequency of the phase plate can be reduced compared to the application of a phase plate applied in a conventional electron microscope. The Zeiss Libra 200 DMU (KRONOS) microscope provides a magnification factor of 3.6x for the diffraction plan inside the diffraction magnification lens (DML). In comparison to the Zeiss EFTEM 923 the focal length of the objective lens is enlarged by a factor of 1.7x, leading to a final magnification factor of 6.1x.

3 Design and operation principles of the electrostatic Zach phase plate, heating system and phase plate holder system

This chapter introduces the design and operating mode of the electrostatic Zach phase plate and a heating system for contamination reduction. Then the fabrication steps of both components are described. Moreover the construction of a new phase plate holder system for the Zeiss Libra 200 DMU is described as well as the installation and working instruction for proper phase plate positioning and image acquisition in phase plate mode.

3.1 Design of the electrostatic Zach phase plate

The electrostatic Zach phase plate was developed as a design improvement of the electrostatic Boersch phase plate. The latter one, consisting of an annular lens electrode supported by three bars, has the disadvantage of obstructing a wide range of spatial frequencies by this mechanical components (figure 3.1 a). Information encoded in spatial frequencies obstructed by the bars from one side in the diffraction plane have been proposed to be reconstructed by utilizing Friedel symmetry in frequency space [34]. Confer chapter 4.5.4 for the new experimental results. The definition of the term Friedel symmetry is given in chapter 1.1.
However, spatial frequencies obstructed by the annular lens electrode are completely lost, because both Friedel pairs are filtered out. To overcome these disadvantages, the non-essential mechanical parts have to be removed. Zach proposed the design of the Zach phase plate [21,35], where the annular lens electrode and two of the three supporting bars are removed, with only one bar remaining. This electrode is built up in a five layered structure. Figure 3.1 b) and c) show CAD drawings of the Zach phase plate and its five layered structure. It consists of a center electrode, surrounded by two insulating layers from the bottom and the top side. This is then shielded by a top and bottom gold layer.

This shielding layer is electrically grounded to produce an electrostatic field at the free tip of the bar, between the center electrode and the outer gold layer. As insulating layers materials are chosen with high permittivity to allow high breakdown voltages.

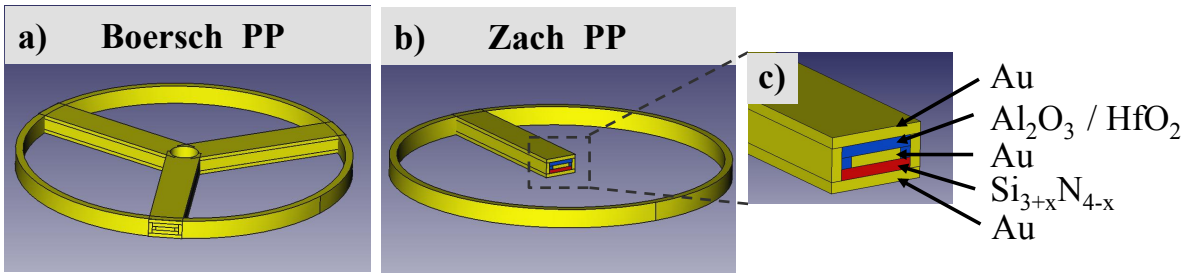

Figure 3.1: CAD drawing of a) the Boersch and b) the Zach phase plate structure. The five layered structure is shown for the Zach phase plate in c). It consists of a central gold (Au) electrode, surrounded by two insulating layers of Al_2O_3 or HfO_2 and $Si_{3+x}N_{4-x}$. This is shielded from the top and bottom side by two gold layers.

The phase plate tip is positioned as close as possible to the zero order beam in a diffraction plane of the transmission electron microscope, as shown in figure 2.4. There, the Zach phase plate produces a highly inhomogeneous electrostatic field with a steep gradient as a function of distance to the electrode tip. The 3D potential distribution can be calculated. A corresponding simulation is discussed in chapter 4.2 and shown in figure 4.2 d). This localized electrostatic field induces a relative phase shift between scattered and unscattered electrons, which are spatially separated in a diffraction plane. The quantity of induced phase shift depends on the voltage level applied to the central electrode and on the distance of the zero order beam to the phase plate tip. For an induced relative phase shift of $\pm\pi/2$ optimal phase contrast transfer is expected. By tuning the voltage between positive and negative values, positive and negative phase contrast can be obtained.

3.2 Design of a heating system for contamination reduction

To address contamination and charging problems during the work with a phase plates, the phase plate is equipped with a heating system. Heating of the phase plate structure helps to remove organic contaminations, which consist mainly of light carbon compounds. These molecules adhere to the phase plate structure and their charging effect becomes apparent mainly at positions close to the phase plate tip, next to the intense zero order beam. The reason for this charging might by a polymerisation of these carbon compounds when hitting them with the focused unscattered zero order beam [36].

Furthermore, there are more contamination effects appearing right after the installation of a phase plate inside a microscope, even before the zero order beam is brought in the vicinity of the phase plate tip. A native oxide layer on the gold surface might be the origin of this charging type [36]. The presence of all such contaminations on the phase plate becomes noticeable in the resulting image quality but especially in the corresponding Power Spectra of this images, where a strong deformation of the Thon rings can be observed (figure 3.2 b) and a "glowing" of the phase plate tip. The definition of the terms Power Spectra and Thon rings is given in chapter 1.1.

The installed heating system for the reduction of unwanted contaminations is based on the developments described in [37]. All heating systems of this type applied in experiments presented in this work, were produced by S. Hettler at Karlsruher Institut für Technologie (KIT). The heating system is fabricated on a separate silicon chip. However, both silicon chips carrying the phase plate structure and the heating device are electrically connected and share the same electrical potential. The connection is made by glueing both chips on a metallic holder plate using a low-resistivity and high-vacuum compatible epoxy glue. Afterwards the electrical connections are fixed by glueing or soldering. A detailed view of a holder plate carrying phase plate and heating system is given in figure 3.3 a) and b). The heating system itself consists of four heating resistors connected in parallel. They are made out of gold traces with thickness of 1 µm and distance of 1 µm (figure 3.2 a), resulting in a total wire length of approximately 4 cm and a total resistance of 4 kΩ. The heating system is operated at 30 V DC with a temperature dependent heating power of approximately 225 mW. After the application of a constant voltage, the specific electrical resistance of the gold wires and together with this the current drop down as a function of temperature. This temperature dependence can be described as linear function for the temperature range in use as

$$\rho(T) = \rho(T_0)\left[1 + \alpha(T - T_0)\right]. \tag{3.1}$$

Here $\rho(T_0)$ is the resistance at starting temperature $T_0 = 20$ °C, $\rho(T)$ is the resistance at the achieved heating temperature and $\alpha = 3.4 \cdot 10^{-3}$ K^{-1} is the empirical linear temperature coefficient for gold at 20 °C. By measuring the current $I(T)$ during the heating process and with the relation $\rho(T) = U/I(T)$, where U is the applied voltage, the reached temperature of the heating system $\Delta T = T - T_0$ can be measured by using

$$\Delta T = \left[\frac{I(T_0)}{I(T)} - 1\right]\alpha^{-1}. \tag{3.2}$$

Thermal stability of the system is reached within one hour and temperatures above 50 °C can be achieved.

Due to heating a thermal expansion occurs, affecting the whole phase plate structure including the supporting holder system. This expansion is in the order of several of ten micrometers. To minimize the heat flow between the phase plate holder and the column of the microscope, the holder is thermally insulated from the microscope. The raise in temperature also decreases the dielectric strength of the insulating layers of the phase plate, resulting in a reduction of the breakdown voltage. This also reduces the maximal achievable phase shift. These effects prevent the simultaneous application of heating system and phase plate imaging. After heating the phase plate system to $50 - 60$ °C for several hours, it has to cool down for about 4-5 hours before phase contrast imaging is again possible.

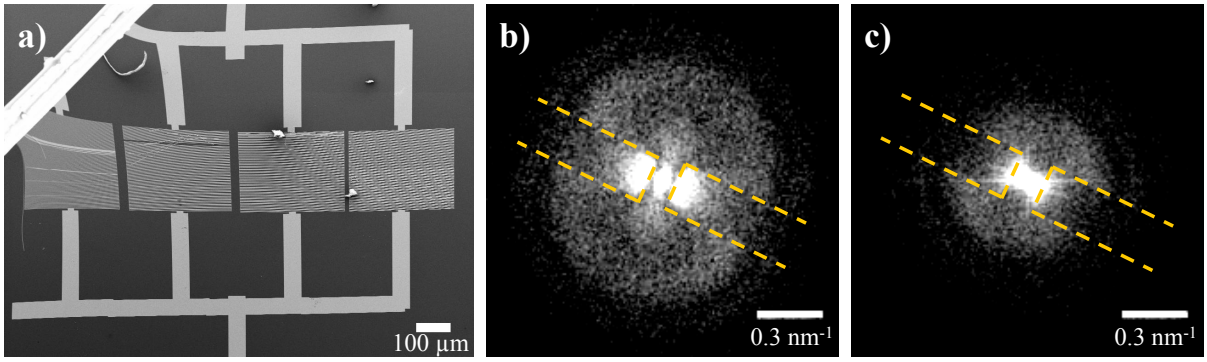

Figure 3.2: Figure a): SEM image of a heating system adapted to Zach phase plates, consisting of four parallel connected Au-heating resistors. Figure b) and c) show Power Spectra of TEM images of filamentous actin embedded in vitreous ice on Quantifoil carbon grids before and after heating of the phase plate. The phase plate position is indicated by blue dashed lines. Figure b): Strong deformation of the Thon rings due to a charged phase plate tip are visible. Figure c): After heating for several hours the deformation of Thon rings disappears.

3.3 Fabrication of the Zach phase plate with heating system

The fabrication process in its basic procedures was established for the manufacturing of Boersch phase plates and the first Zach phase plates as described in [18] and [38]. Some technological advances were applied as reported in [37] and will be briefly described in the following. For the fabrication of the phase plate, a commercially available low stress silicon nitride membrane ($Si_{3+x}N_{4-x}$) is used as starting material. At the same time, this is the first of the two insulating layers, as shown in figure 3.1 b). This silicon membrane is coated on a silicon chip with a thickness of 200 µm and width and length of (4x12) mm^2. The supporting silicon chip contains two cut-out windows above which the silicon nitride

membrane is self-supported. Three different windows sizes and membrane heights are used for fabrication of phase plates applied for the experiments presented in this work: 100 µm x 100 µm x 100 nm (height), 200 µm x 200 µm x 200 nm (height) and 500 µm x 500 µm x 100 nm (height).

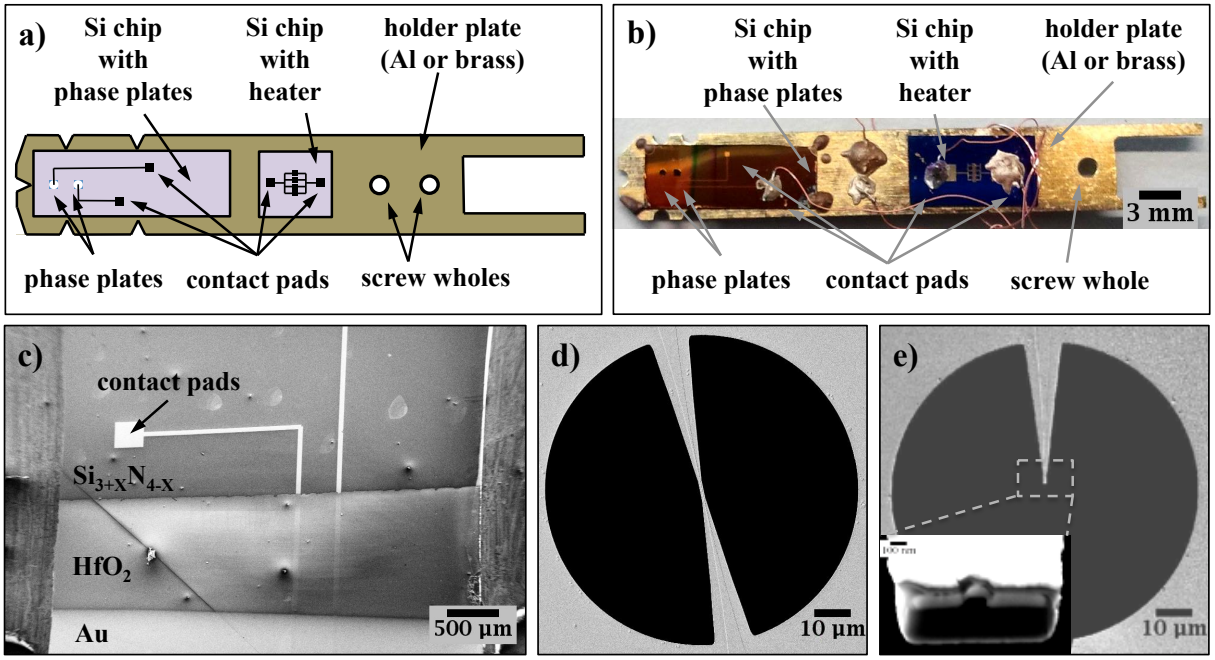

Figure 3.3: Figure a) and b): Schematic and real image of a holder plate with glued on phase plate chip, heating system and electrical contacts. Figure c): SEM image of a evaporated Au, HfO_2 and $Si_{3+X}N_{4-X}$ layers at their evaporation boarder near a contact pad. (Figure d) and e) acquired by S. Hettler, KIT.) Figure d): SEM image of a phase plate structure after evaporation of all layers and figure e): final phase plate structure after cutting with FIB. The zoomed out image shows the five layered profile of the tip.

The first step in the fabrication process is to coat the bottom side of the silicon chip with a conducting metal layer to form the bottom part of the shielding outer layer. Here gold is used as coating material. The coating is done by using electron beam evaporation inside a high vacuum chamber. For a better adhesion of the gold layer, first a chrome layer of 3.5 nm thickness is evaporated onto the silicon chip. The subsequent evaporated gold layer has a thickness between 70 nm and 150 nm for Zach phase plates used in this work.

Afterwards, the central electrode, a pad for electrical connection and the interconnection in between is fabricated. The top side of the silicon nitride membrane is coated with an electron sensitive varnish. By using electron beam lithography the varnish is irradiated with an electron beam in the region of the cut-out windows. Here the varnish at the future position for the center electrode and the contact pad is illuminated by the electron

beam. After this, the irradiated vanish is washed away by methyl isobutyl ketone, leaving a negative topological structure of the future central electrode.

For the central electrode gold is used as material, as well as for the shielding outer layers. Gold and a underlying Chrome layer for a better adhesion are coated onto the remaining varnish by again using electron beam evaporation. The thickness of the central gold electrodes varies between 40 nm and 75 nm for the Zach phase plates used in this work. The width varies between 140 nm and 1200 nm. Afterwards the varnish layer with the chrome and gold on top are removed by washing the chip in acetone, leaving only the electrode, pad structure and interconnection.

The structure of the Zach phase plate including the bar with the central electrode and the surrounding aperture have now to be cut out from the silicon nitride membrane. This is done with dry-plasma etching using CHF_3 and O_2 gases. This fabrication step replaces a former cut out method by using a 30 V focused ion beam operated with Ga^+ ions (Zeiss EsB 1540 SEM/FIB dual-beam). Using dry-plasma etching has the advantage of providing better reproducibility of the cut out structures, multiple phase plates can be fabricated simultaneously and aperture with larger diameters but unchanged electrode bar tip width can be produced.

Due to mechanical stability reasons, first a bar containing the electrode but also connecting two opposite sides of the aperture is left over after the cut-out process. Furthermore for the same reason both sides of the bar are extended in width from the center of the aperture towards the border (figure 3.3 d).

In the next fabrication step the second insulation layer has to be coated onto the cut-out electrode bar, the surrounding aperture area and the connection part to the contact pad. From this coating step on, the contact pad has to be covered to ensure that it remains free from coating by further materials.

As materials Al_2O_3 or HfO_2 are used. Again these layers are deposited by using electron beam evaporation under high vacuum conditions. For the Zach phase plates used in this work the layers thickness of Al_2O_3 or HfO_2 varies between 100 nm and 140 nm. Due to its higher dielectric strength HfO_2 was used to replace Al_2O_3.

As last coating step the electrode bar has to be covered from the top, left and right side with the conducting metal layer to form the last part of the shielding outer layer. Here again, gold with an underlying chrome layer is used for coating. The silicon chip is rotated inside the evaporation chamber to ensure all sides to be evenly coated. This last gold layer has a thickness between 70 nm and 150 nm for the used Zach phase plates.

Afterwards, the unwanted parts of the electrode bar have to be cut out by using a 30 kV focused ion beam (FIB) operated with Ga^+ ions (Zeiss EsB 1540 SEM/FIB dual-beam). This includes one half of the bar that contains no electrode, left over only for a better

mechanical stability during all fabrication steps. The remaining electrode bar extending from the border of the aperture up to center has a tip width between 2.8 µm and 1 µm for the phase plates used in this work. The aperture diameter ranges from 90 µm to 470 µm (figure 3.3 e).
The heating system for the phase plate is fabricated on a separate silicon chip with the same characteristics as the one for the phase plate fabrication. The application procedure of the gold wires of the four heating resistors and their supply conductors onto the silicon chip is identical to the fabrication step of the central gold electrode of the phase plate. A negative topological structure on a coating of varnish layer for the future wire positions is drawn by using electron beam lithography. The gold and underlying chrome layers are coated by using electron beam evaporation under high vacuum conditions. As before, excessive varnish is washed away with methyl isobutyl ketone.
This work was mainly done by B. Gamm and S. Hettler in the collaboration with D. Gerthsen, LEM (KIT).

3.4 Construction of a new phase plate holder system for Zeiss Libra 200 DMU

For the application of phase plates with the Zeiss EFTEM 923 a holder system already exists from former experiments with Boersch phase plates. For the implementation of the electrostatic Zach phase plate into the Zeiss Libra 200 DMU a new phase plate holder system had to be designed. This system allows the assembly of the phase plate into the electron microscope and its precise positioning into the diffraction plane inside the DMU. The principal components of this new phase plate holder are a piezo driven Kleindiek micro-manipulator (MM3A-UHV) adapted with a self-made phase plate carrier system and the electrical line system to control the micro-manipulator, the phase plate potential and the heating system. The micro-manipulator is screwed to an aluminium flange, which is adapted with a vacuum compatible electrical connector. Furthermore a lead cover is mounted above the flange to shield possible X-ray irradiation. Figure 3.4 a) and b) show a CAD drawing and the completed phase plate holder system with its main components. Figure c) shows the Zeiss Libra 200 DMU with the mounted phase plate holder system and the electrical splitting box for system control. The DMU is marked in red.
The Kleindiek micro-manipulator allows a horizontal in/out movement with a step size of 0.25 nm and 12 mm operating range. For left/right and up/down movement only a slewing drive is possible, with a step sizes of $1 \cdot 10^{-6}$ mrad and 240° operating range. To prevent an inclination of the phase plate inside the DMU, the up/down motion is used as little as possible.

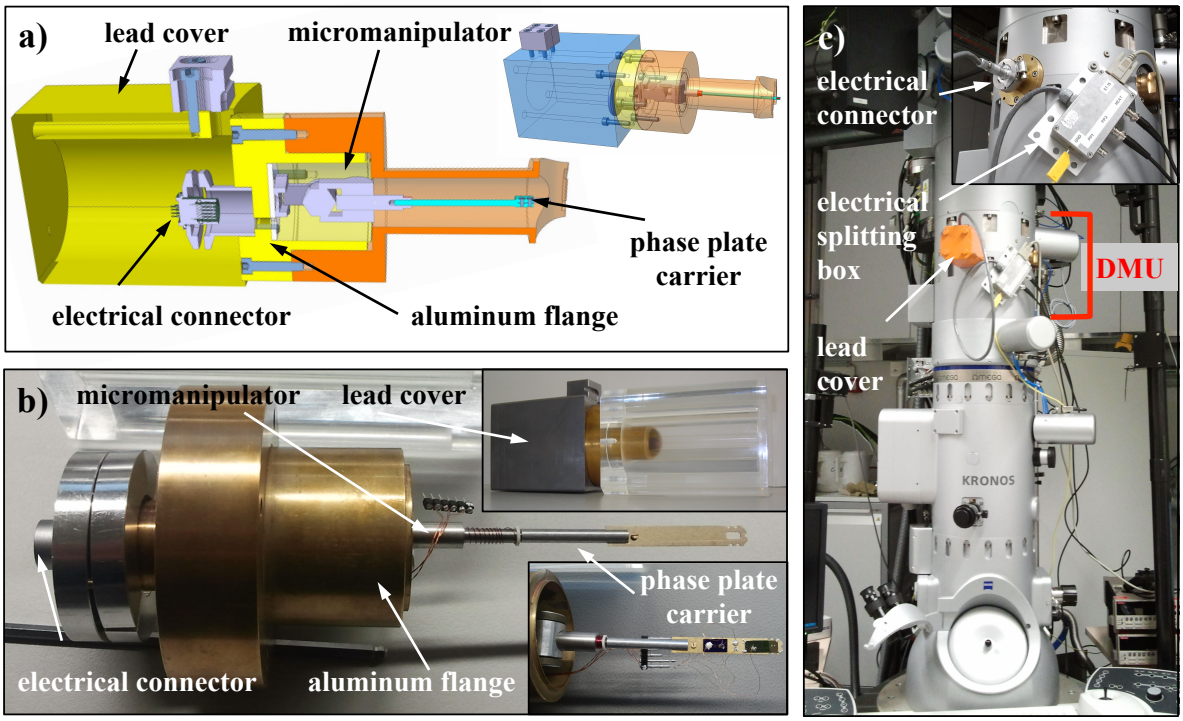

Figure 3.4: Phase plate holder system for the Zeiss Libra 200 DMU (KRONOS). Figure a) shows a CAD drawing of the system with its main components. Figure b) shows the complete fabricated system. In figure c) the microscope with mounted phase plate holder system, lead cover (orange) and electrical splitting box is shown. The position of the DMU is marked in red.

3.5 Installation and evolving working instruction for phase plate microscopy

As described in chapter 2 the Zach phase plate has to be inserted into a diffraction plane of the electron microscope. This is done by using phase plate holder systems as developed in this work and described in section 3.4. This holder system together with the Zach phase plate is inserted a) into the back focal plane of the objective lens when operated with the Zeiss EFTEM 923 or b) into the DMU when operated with the Zeiss Libra 200 DMU.

For the proper positioning of the phase plate, the microscope is first operated in low magnification mode. In this mode the phase plate carrier is driven into the beam path with the micro-manipulator. The notches at the front and the sides of the phase plate carrier visible in figure 3.3 a) and b) help to find the position of the phase plate aperture. When the phase plate aperture is centred on the fluorescence panel the user has to change to normal magnification mode and diffraction mode at the desired magnification for the following image acquisition. A small condenser aperture has to be inserted to provide

a sharp diffraction image with high spatial coherence and the camera length (CL) in diffraction mode should be set to the highest possible value to provide a large magnification of the phase plate structure. This facilitates the following positioning steps:
The zero order beam should now pass through the phase plate aperture. If this is not the case, this has to be corrected by driving the phase plate in/out and left/right with the help of the micro-manipulator. The phase plate tip has now to be positioned close to the zero order beam. However the user has to pay attention to not hit the tip with the intense zero order beam to prevent early contamination. Next phase plate and diffraction plane height have to be aligned. For this the edges of the phase plate tip have to be focused until they are visible as sharp edges. This is done by using the diffraction focus. Hereby the diffraction image of the sample is defocused and the zero order beam is blurred. To focus again the zero order beam and setting the diffraction plane at the same height as the phase plat tip, two possibilities have to distinguished, according to the used microscope. For the Zeiss EFTEM 923, where the phase plate is inserted into the back focal plane of the objective lens, the 3rd condenser lens is used to set this diffraction plane at the same height as the phase plate. For the Zeiss Libra 200 DMU, where the phase plate is inserted into the DMU, the adaption lens (ADL) of the C_S corrector is used for this purpose. The final fine positioning of the phase plate tip to the zero order beam is done by using the CCD camera with a software package that provides a live FFT image during a continuous image acquisition. The Friedel symmetric tip pair is visible in this live FFT image and has now to be placed as close as possible to the zero order beam at the image center. Furthermore both phase plate bars have to be aligned in one line. For this purpose TVIPS TemCam F416 (4096 x 4096 pixel) CMOS cameras with the software package EMMENU where use with the Zeiss EFTEM 923 as well as with the Zeiss Libra 200 DMU.

4 Application of the electrostatic Zach phase plate for TEM with conventional electron optics

In this chapter the first application of the electrostatic phase plate on biological samples is discussed. As samples a mouse diaphragm muscle embedded in epon and filamentous actin embedded in vitreous ice are used. The influence of phase plate geometry on image appearance is discussed, as well as practical factors influencing the usability of the electrostatic Zach phase plate in a microscope with conventional electron optics, using a Zeiss EFTEM 923.

4.1 Previous proof of principle for Zach phase plate application for TEM

In very first experiments, Schultheiss et al. [22] reported a proof of principle for the applicability of Zach phase plates in TEM. In the experiments it was shown that phase contrast imaging using a Zach phase plate is possible for material science samples. The following example taken from [38], was executed with a Zach phase plate applied to the Zeiss EFTEM 923 operated at 120 keV. On the basis of a wedge sample consisting of Si, Al_2O_3, C and Mo layers it was shown that by applying different voltages to the positioned Zach phase plate, a change in phase contrast is achieved. This is visible in the zoomed in regions from the C layer (figure 4.1) showing granular structures with diameters of 4 - 5 nm. The presence of the phase plate structure in the correct position in the back focal plane already changes the appearance of phase contrast (figure 4.1 c)), compared to the reference image of the same sample area without phase plate with a small defocus value of 350 nm (figure 4.1 b)). By applying different potentials of ± 0.4 V (figure 4.1 d)+e)), a relative phase shift of $\pm 0.2\pi$ is achieved.

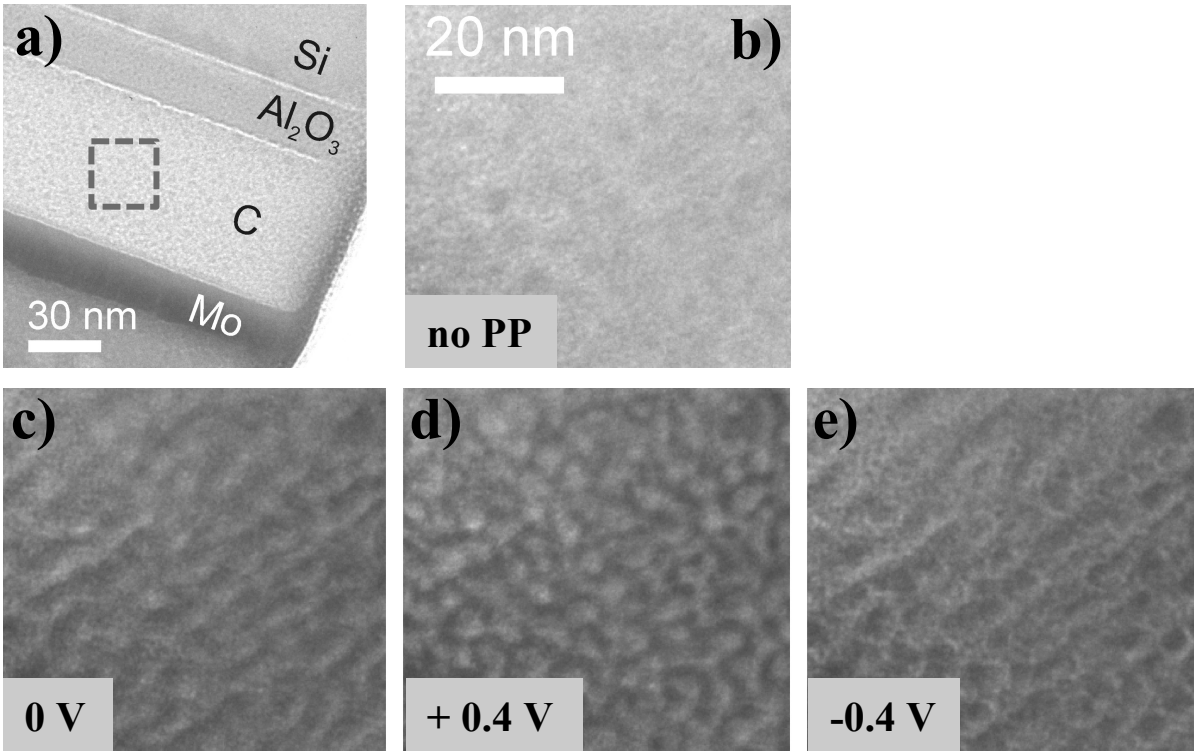

Figure 4.1: Images of a wedge sample consisting of Si, Al_2O_3, C and Mo layers taken from [38]. Figure a): overview of the wedge sample showing the different layers. Figure b): zoomed-in image of the C area, with a defocus of $\Delta z = 350$ nm, without inserted phase plate (PP). Figure c): same sample area with inserted phase plate but without applied potential (0 V). Figure d) and e): change in phase contrast due to application of ± 0.4 V.

4.2 Simulation of electrostatic potential

The electrostatic Zach phase plate produces a highly inhomogeneous electrostatic potential with a steep gradient as function of distance to the phase plate tip. This three dimensional potential distribution around the phase plate tip can be simulated using finite element methods. This is show in figure 4.2 a) and b). For the simulation the programs gmsh (three-dimensional finite element mesh generator) and getdp (general environment for the treatment of discrete problems) [39, 40] are used and self programmed algorithm using the software package MatLab (The Math Works, USA). A more detailed explanation of their functionality is given in Appendix A and B.

Due to the steep gradient of the electrostatic phase plate potential the amount of phase shift for the zero order beam depends on the distance to the phase plate tip. Furthermore this also results in a distance dependence for relative phase shifts between the zero order beam and spatial frequencies in its close vicinity. Owing to the relation $r = 1/q$ between distances r in position space and frequencies q in frequency space, this means, that the

larger the dimensions of an object, the smaller the radial distance of its corresponding spatial frequencies to the zero order beam. Hence, the smaller this distance, the smaller the induced relative phase shift by the phase plate.
The induced phase shift as function of distance to the phase plate tip can be calculated from the simulated three dimensional potential distributions and their subsequent integration along the beam path shown in figure 4.2. For the phase plate dimensions used for the experiment with the wedge sample a phase shift of $\pm 0.2\pi$ for an applied potential of ± 0.4 V was determined. Furthermore the Zach phase plate has no sharp defined cut-on frequency, from which onwards the relative phase shift between an ideal delta peak shaped zero order beam and the spatial frequency would be equal or larger then $\pi/2$, as shown in image 4.2 d) as red line. Instead it shows a soft cut-on frequency. The Gaussian shaped zero order beam itself also has a certain diameter and is positioned approximately at 500 nm from the phase plate tip in an ideal case*. For the used Zach phase plate geometries in the wedge sample experiment, frequencies near to the zero order beam in the range of $0.5 - 0.8$ nm^{-1} might show some problems for phase contrast imaging. This corresponds to an object size of 15 - 25 nm for an acceleration voltage of 120 keV and a focal length of 3.6 mm.
From these results several questions arise. What happens if objects in the diameter range of 15 - 25 nm or larger are imaged with this Zach phase plate? Is then an enhancement of phase contrast possible, even at higher acceleration voltages? How does the dimension of the phase plate structure affect the image as function of its distance to the zero order beam? The wedge sample consists of a layered structure that includes materials with a relative hight mass thickness compared to biological samples (mainly C, H, N, O). This leads already to a higher amplitude contrast. Furthermore the image series shown in figure 4.1 are not taken in-focus but with a small defocus. Is therefore a successful application of in-focus phase contrast imaging possible for weak phase objects such as biological samples embedded in vitreous ice? In order to answer this questions, different experiments are performed and described in the following.

* This value proved experimentally to be an optimal distance to prevent charging of the phase plate tip. From the simulations (figure 4.2) it is obvious, however, that a smaller distance would be advantageous, as then the zero order beam would be on a steeper gradient of the potential. This would result in a smaller cut-on frequency.

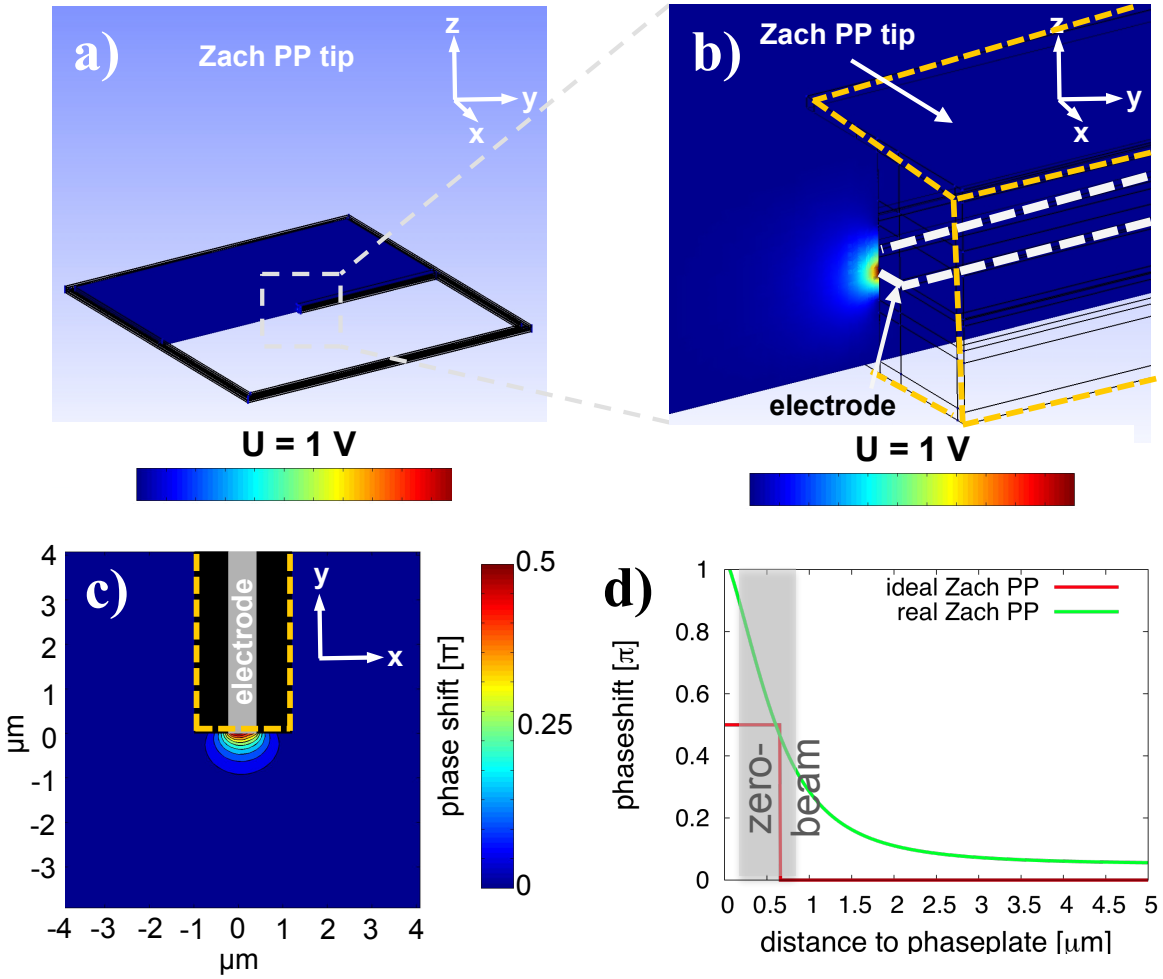

Figure 4.2: Overview of the 3D Zach phase plate model used for the images shown in figure 4.1. A clipped 3D potential distribution of a Zach phase plate is shown in figure a). The zoomed out 3D potential distribution around the tip with a range form 0 V to 1 V is shown in b). Figure c) shows the integrated potential along the z-direction. Figure d) shows the resulting phase shift as function of the distance to the phase plate tip (green line) and a hypothetical ideal phase shift as step function (red line).

4.3 Impact of phase plate positioning and analysis of phase contrast imaging on beam insensitive samples

4.3.1 Sample preparation, microscope and phase plate specifications

To answer the questions arising from the last section, experiments on different type of samples are performed. In the following sections each is described in more detail. All are executed with Zach phase plates installed in the Zeiss EFTEM 923 microscope, operated at 200 keV. This transmission electron microscope is equipped with a field emission gun (FEG), an incolumn omega energy filter and a cooling system for Cryo-TEM application. The objective lens has a focal length of 2.7 mm and spherical aberration C_S of 2.2 mm. Furthermore the microscope is equipped with a TVIPS TemCam F416 (4096 x 4096 pixel) CMOS camera, with a physical pixel size of 15.6 x 15.6 µm^2.
For the first experiment 70 nm sections containing ribosomes of a mouse diaphragm muscle all embedded in epon, fixed without osmium stain but post-stained with uranyl acetate are used as sample. The ribosomes have an average diameter of 25 nm, leading to a corresponding spatial frequency in Fourier space of q = 1/25 nm^{-1}. This sample is selected for first test applications, as it is relative beam insensitive compared to biological cryo samples embedded in vitreous ice. Therefore it can be used for longer image acquisition series of the same sample area without inducing any beam damage to the sample. This was a necessary first prototype experiment to study and develop the necessary steps and workflow for the phase plate alignment.
The used phase plate has the name "PP1" and the following dimensions: total tip width 2.8 µm, central electrode width 0.8 µm. The layer thickness are: Au top layer 120 nm, Al_2O_3 layer 100 nm, central electrode Au layer 40 nm, $Si_{3+x}N_{4-x}$ layer 200 nm, Au bottom layer 100 nm.
To give a better overview of the phase plate geometries for all phase plates operated in experiments presented in this work, the following table list the most important parameters. Phase plates are named with "PP1", "PP2" and "PP3". In the corresponding chapter the used phase plate is denoted with the respective name.

Table 4.1: Phase plates geometries for Zach phase plates used in experiments presented in this work.

phase plate name	**PP1**	**PP2**	**PP3**
microscope	EFTEM 923	EFTEM 923	Libra 200 DMU
layer thickness			
Au top layer	120 nm	150 nm	70 nm
Al_2O_3 layer	100 nm	100 nm	-
HfO_2 layer	-	-	100 nm
Au central electrode layer	40 nm	50 nm	75 nm
$Si_{3+x}N4 - x$ layer	200 nm	200 nm	100 nm
Au bottom layer	100 nm	150 nm	70 nm
total tip width	2.8 µm	1.3 µm	1.0 µm
central electrode width	0.8 µm	0.5 µm	0.14 µm

4.3.2 Experimental results

First the influence of the phase plate geometry and the distance between phase plate tip and zero order beam on the image formation is investigated. For these experiments no voltage is applied to the phase plate. Figure 4.3 a) shows an overview of the sample and three images of the zoomed in area at higher resolutions in b) - d), with their corresponding power spectra in e) - g), imaged with an under-focus value of 680 nm. Visible are ribosomes arranged as a string around the former position of the lipid membrane of rough endoplasmic reticulum. Due to the sample preparation method, without using osmium, membrane lipids are not preserved and no membrane is visible.

In the corresponding Power Spectra, the structure of the phase plate bar is visible as obstruction of the Thon rings. Due to the fact that the Power Spectra image is the square of the absolute value of the wave function, the bar of the phase plate is always visible twice at Friedel symmetric positions. However the bar obstructs the structure factors only from one side in the diffraction plane where it is installed.

In this image series the distance of the phase plate tip to the zero order beam is decreased from 670 nm in image b), to 320 nm in image c) and finally to 150 nm in image d). The structure factors corresponding to the diameter of the ribosomes at $q = 1/25\ nm^{-1}$ are indicated as orange dot in the corresponding power spectra 4.3 e) - g). In image 4.3 b) - d) it is visible that by reducing the distance between electrode tip and zero order beam the appearance of the ribosomes changes toward a topological structure with a shading in direction from left upper corner toward right lower corner. This topological appearance becomes more pronounced with smaller distance of the phase plate tip to the zero order beam. This is first visible in image 4.3 c) for the small feature, as their spatial frequencies are first affected by phase plate obstruction in the diffraction plane.

The topological appearance for the ribosomes start to become visible in image d). The orientation of the shadow is consistent with the orientation of the phase plate bar visible in the Power Spectra. In this Power Spectra images it is obvious that the electrode bar starts to obstruct parts of the structure factors at $q = 1/25$ nm^{-1} corresponding to the diameter of 25 nm of the ribosomes. The resulting topological sample appearance is called single sideband contrast [7]. Furthermore the Power Spectra show indications of charging on the phase plate tip, visible as light "white glowing" around the tip borders. It should again be noted, that the image series is recorded without applying any potential to the phase plate. However a displacement of the Thon rings is visible when decreasing the distance of phase plate tip to zero order beam. This can only be achieved and explained if already an electrostatic field at the phase plate tip exists. At present in this work it is assumed that already charging of the tip occurs if brought into close proximity of the intense zero order beam.

Next the influence on phase contrast when applying different potentials to the phase plate electrode is investigated. For this the same sample area is chosen and the distance of phase plate tip to zero order beam is 150 nm as in image 4.3 d). Image 4.4 a) - c) shows three images of the same sample position but with different applied potential values to the phase plate: a) U = +0.8 V, b) U = 0.0 V and c) U = -0.8 V. Images 4.4 d) - f) show the corresponding Power Spectra. By comparing images a) - c) only a slight change in contrast is visible as function of changing applied potential. This can be explained by the fact that single sideband contrast dominates the image. To visualize the pure change in phase contrast and to eliminate the dominant single sideband contrast, images are aligned to each other. Then images with applied voltage a) and c) are subtracted from image b) without applied voltage. These results are show in figure 4.4 j) and k). Image k) shows still some topological appearance, which might arise from insufficient alignment of the images before subtraction. Both images show bright ribosomes structures on dark background, which can now be interpreted as positive phase contrast.
Compared to the TEM images the corresponding Power Spectra in figure 4.4 d) - f) show a significant change in contrast transfer. The Thon ring positions have clearly changed as function of applied voltage. Images 4.4 g) - i) show rotational averaged radial line scans of the three power spectra in d) - f) (black lines). Also shown are the background subtracted rotational averaged line scans (doted grey lines) and the fitted 2D power spectra function (red lines), which includes the determined values for defocus and phase shift induced by the phase plate potential. The determination of defocus and phase shift are performed using the software package SPIDER and self programmed algorithm using the software package MatLab (The Math Works, USA). A more detailed explanation of their functionality is given in Appendix B and C. From this an under-focus of $\Delta z = 680$ nm and phase shifts

of $\phi_{\mathrm{PP},+0.8\mathrm{V}} = 0.25\pi$, $\phi_{\mathrm{PP},0.0\mathrm{V}} = -0.1\pi$ and $\phi_{\mathrm{PP},-0.8\mathrm{V}} = -0.63\pi$ are determined.
The different amount of induced phase shift at ± 0.8 V phase plate potential can be due to an increasing phase plate charging, occurring during image acquisition and depending on accumulated electron dose. The sequence of image acquisition in figure 4.4 is in the order a), b), c). This might be the reason for the phase shift offset $\phi_{\mathrm{PP},0.0\mathrm{V}} = -0.1\pi$ in image b) and the larger absolute value of phase shift in image c).
As indicated in image 4.3 e) by the orange dot, the spatial frequency at $\mathrm{q} = 1/25\ \mathrm{nm}^{-1}$ corresponding to the ribosome diameter are located at very close vicinity to the zero order beam. Due to this the relative phase shift between these frequencies and the zero order beam is clearly smaller than the determined phase shifts for the three different applied phase plate potentials. This leads to almost no change in phase contrast for the ribosome structures visible in figure 4.4. The reason for positive phase contrast visible in both subtracted images j) and k) results from the very similar contrast transfer characteristic for the images with applied phase plate potential of +0.8 V and -0.8 V in image g) and h), that are both subtracted form the image without applied voltage, respectively.

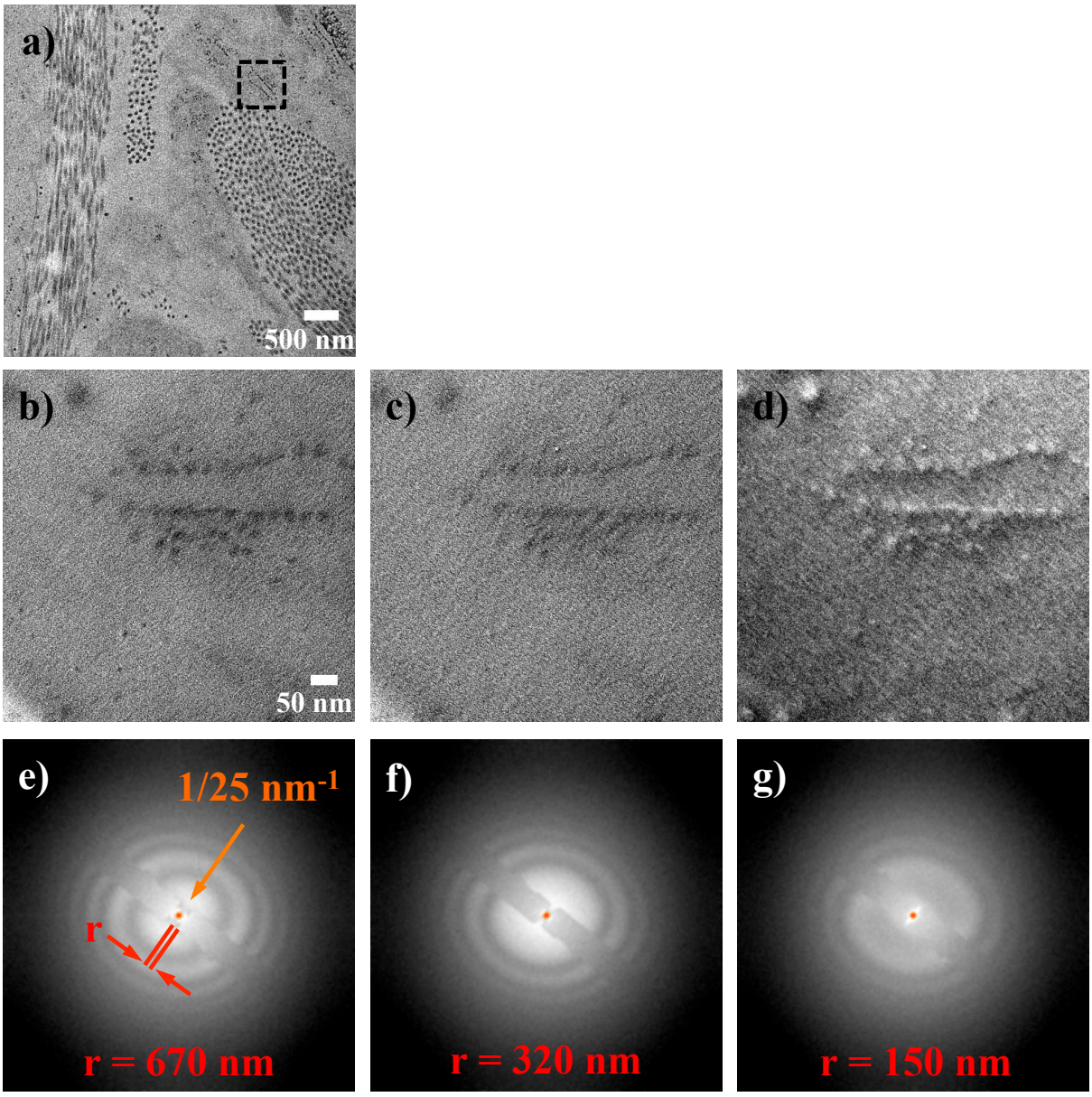

Figure 4.3: Ribosomes of a mouse diaphragm muscle embedded in epon, without osmium stain but post stained with uranyl acetate. Figure a): sample overview and zoomed out region. Figure b) - d): ribosomes of rough endoplasmic reticulum, imaged with inserted phase plate at different distances to the zero order beam. No voltage is applied to the phase plate. Figure e) - g): corresponding power spectra to images b) - d). Friedel symmetric phase plate rod pairs are visible as obstruction of the Thon rings, with distances of the tip to the zero order beam: e) r = 670 nm, f) r= 320 nm and g) r = 150 nm. A change in Thon ring radius is visible as function of distance r. Single sideband contrast arises in d) when the tip starts to obstruct part of the spatial frequencies at $q = 1/25$ nm^{-1} belonging to the ribosome diameter (orange dot) and visible as topological sample appearance. Sample prepared by I. Wacker and C. Bartels.

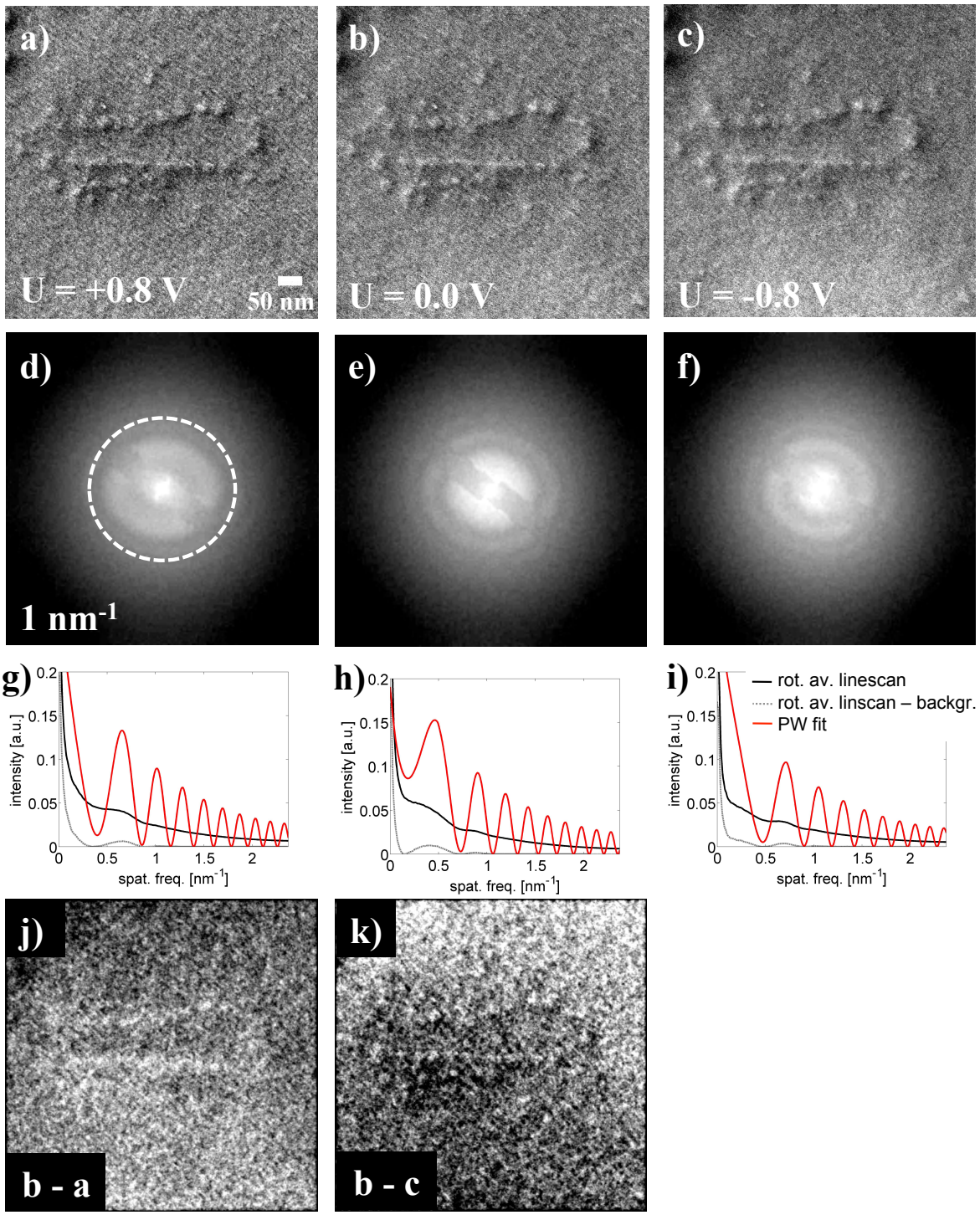

Figure 4.4: Ribosomes embedded in epon. Images acquired with inserted phase plate and applied potentials of a) +0.8 V, b) 0.0 V and c) -0.8 V. Image d) - f): corresponding power spectra. Image g) - i): rotational averaged line scans of power spectra. An under-focus of $\Delta z = 680$ nm and phase shifts $\phi_{\mathrm{PP},+0.8\mathrm{V}} = 0.25\pi$, $\phi_{\mathrm{PP},0.0\mathrm{V}} = -0.1\pi$ and $\phi_{\mathrm{PP},-0.8\mathrm{V}} = -0.63\pi$ are determined. Images j), k): subtracted images acquired from b)-a) and b)-c), showing change in phase contrast. Sample prepared by I. Wacker and C. Bartels.

4.4 Phase plate imaging with invertible phase contrast of frozen-hydrated filamentous actin

4.4.1 Sample preparation, microscope and phase plate specifications

In the following experiment filamentous actin from rabbit embedded into vitreous ice is used as sample*. After freezing in a Vitrobot Mark IV (FEI) the sample is imaged under cryo conditions using the Zeiss EFTEM 923 at an acceleration voltage of 200 keV.
For sample preparation the filamentous actin in buffer solution is applied to a TEM sample grid and shock frozen with a cooling rates of 10^7K/s [41, 42] by plunging it into liquid ethane. This high cooling rate ensures transformation from liquid water into vitreous ice and prevents the formation of cubic or hexagonal ice crystals [42]. The reservoir with liquid ethane is cooled down close to its freezing point at $-172°$C inside a liquid nitrogen bath at $-196°$C (boiling temperature of nitrogen). The plunging process is executed by using a guillotine like device (Vitrobot Mark IV, FEI). Here a tweezers holding the grid wetted with 3 µl of sample solution is shot into the ethane reservoir. For imaging the sample with TEM, the frozen grid has to be transferred into a cryo sample holder (Model 626, Gatan Inc., USA). The cryo holder tip is cooled by a liquid nitrogen reservoir at temperatures between $-160°$C and $-196°$C to maintain the ice in its vitrified state during microscopy session. For the sample transfer it is important that the sample is always surrounded by liquid or gaseous nitrogen. This is to prevent contaminations due to condensation of water on the grid.
The actin filaments consist of helical double-strand arrangement of protein actin monomers. Each actin monomer has a length of 5.5 nm, the helical actin filament has a diameter of 5 - 9 nm and the helix has a twist repeating every 35.7 nm (13/6 helix symmetry = 13 symmetry units per 6 times 360°) [43, 44]. As the diameter of this filaments is smaller then the diameter of the ribosomes from the former experiment by a factor of 2.8 - 5, the corresponding spatial frequencies of the filaments diameter in frequency space have a larger radial distance to the zero order beam and therefore suit better for Zach phase plate application with the Zeiss EFTEM 923.
The Zach phase plate used for this experiment is named "PP2". The corresponding dimensions are listed in table 4.1. A SEM image of this phase plate is shown in figure 4.5.

* Protein suspension was prepared by S. Fujita-Becker. Subsequent samples preparation was done by myself.

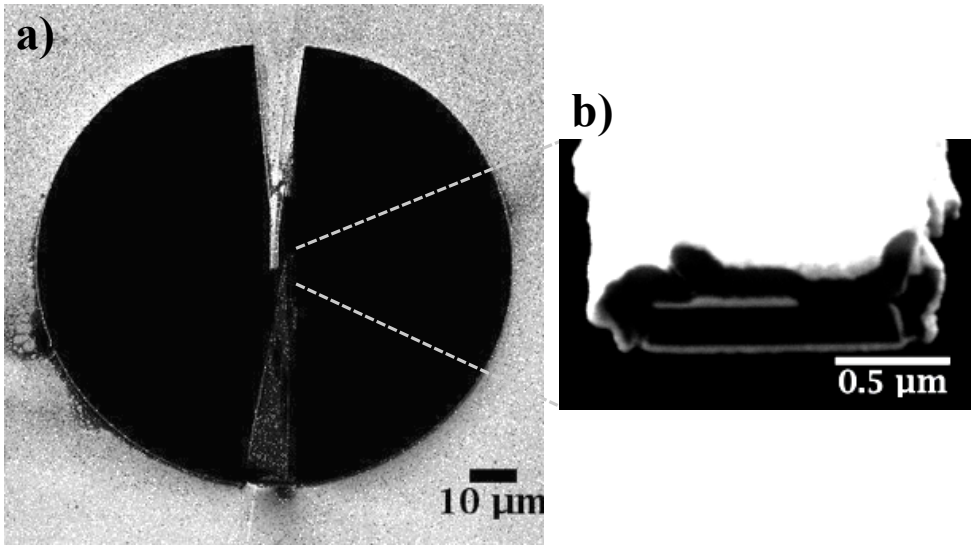

Figure 4.5: Figure a): SEM image of the phase plate used for Cryo-TEM with the Zeiss EFTEM 923 for the image acquisition of filamentous actin embedded in vitreous ice. Figure b): zoomed out phase plate tip showing the layered structure. Images acquired by S. Hettler, KIT.

4.4.2 Experimental results

For the phase contrast imaging with Zach phase plate, four images of the same sample area are acquired, shown in figure 4.6 a) - d). Each exposure was recorded with an electron dose of 15 $e^-/Å^2$. The first image a) is taken at an under-focus of 6.5 µm without inserted phase plate. This reference image gives an overview of all filaments present in the sample area. Figure 4.6 b) - d) are acquired in focus ($\Delta z = 0$ nm) and with positioned phase plate. In image b) no potential is applied to the electrode (0.0 V). Compared to image a) almost no filaments are visible, as expected for images acquired in focus. However filaments labelled with blue arrows, with an orientation from the left lower to the right upper corner of the image are still visible with good contrast. The spatial frequencies corresponding to the diameter structure of this helical filaments i.e. perpendicular to the filament, are arranged in the same direction as the obstructing phase plate tip in frequency space. This is visible in the corresponding Power Spectra in figure 4.6 f). Due to frequency obstruction in one half plane, single sideband contrast is the reason for the visibility of these filaments. In figure 4.6 c) and d) potentials of +0.9 V and -0.9 V are applied to the phase plate electrode. An inversion of contrast is now clearly visible. Filaments with an orientation from the upper left to the lower right corner, labelled with red arrows, without contrast in figure 4.6 b), are now visible with positive phase contrast in figure 4.6 c) and with negative phase contrast in figure 4.6 d). Filaments with perpendicular orientation show also a slight variation in contrast appearance, however, no inversion from positive to

negative phase contrast is visible. This is the result of dominant singe sideband contrast.

The change in phase contrast is examined in more detail for two exemplary filament sections, with perpendicular relative orientation. For this the mean intensity of all images are adjusted by shifting the histograms. The image regions for the line scans are aligned to each other and cut out. Then line scans are taken across filament structures. Each line scans is averaged over a line width of 1000 pixel. Figure 4.6 i) shows the two zoomed out regions for line scans and the change in phase contrast by applying +0.9 V, 0.0 V and -0.9 V to the phase plate. The corresponding line scan graphs for the three applied potentials are shown in figure 4.6 j) - l).

Filament No.1: line scans in the diagram shown in figure 4.6 j) for +0.9 V (red line) and -0.9 V (blue line) potential application shows both two main peaks with inverted amplitudes at the same distances. The direction of the peaks is inverted in the two line scans, showing the contrast inversion. Line scan for 0.0 V (green line) does not show any distinct peaks due to a contrast change in this area. The diagram in figure 4.6 k) compares line scans for -0.9 V (blue line) and the image acquired with 6.5 µm under-focus (black dotted line). Both line scans show a distinct peak in the region between 11 - 17 nm, whereas the line scan for the defocused image shows a higher amplitude, indicating higher contrast. The peak width is comparable for both line scans.

Filament No 2: all three line scans in the diagram shown in figure 4.6 l) for +0.9 V (red line), 0.0 V (green line) and -0.9 V (blue line) show two distinct peaks with inverted amplitudes at 15 nm and 20 nm, same amplitude hight and comparable width. The diagram in figure 4.6 m) comparing line scans for -0.9 V and under-focus of 6.5 µm shows again, that peak amplitude is slightly higher for the defocus image, but peak widths are comparable. Since figure 4.6 b) - d) are acquired in-focus, an identification of the phase shift ϕ_{PP} with the used algorithms is not possible. It is very probable that the phase shift is in the region of $\phi_{\mathrm{PP},\pm 0.8\mathrm{V}} = \pm\pi/2$ as indicated by the inverted contrast.

The effect of inverted phase contrast is also visible in the change of diffraction contrast in the area of crystalline ice, marked with green crosses in figure 4.6 a) - d). Due to defocusing in figure a) the crystalline area is seen as dark central intensity spot and to bright side maxima. In figure b) the side maxima are not visible any more, as the images acquired in focus. The contrast of the crystalline structure changes its contrast from bright contrast in figure c) to dark contrast in figure d) by applying opposite potentials values to the phase plate.

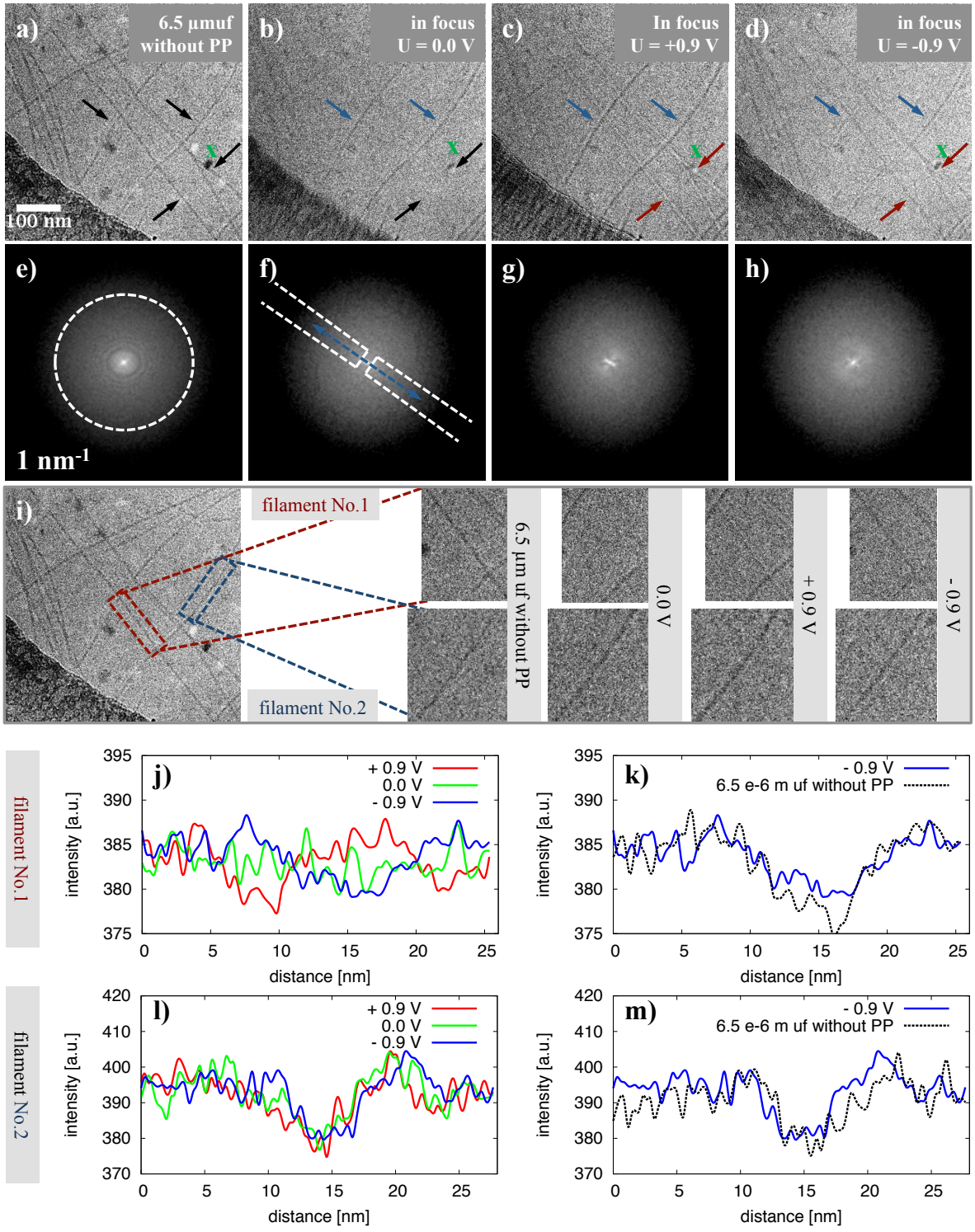

Figure 4.6: Filamentous actin embedded in vitreous ice. Sample imaged in a) without phase plate at 6.5 µm under-focus, with phase plate and applied voltage of b) U = 0.0 V, c) U = +0.9 V, d) U = -0.9 V. Corresponding power spectra are shown in e) - h). Line scan analysis of two rectangular oriented filament sections shown in i), are plotted in j) - m) for different applied phase plate potentials.

4.5 Discussion

The experiments presented in this chapter show that phase contrast imaging even with invertible phase contrast with the electrostatic Zach phase plate for biological samples embedded in epon or vitreous ice is possible. In this section the following point are discussed:

- influence of beam coherence on phase plate applicability
- contamination and its influence on lifetime of the phase plate
- influence of phase plate obstruction on image quality
- numerical correction of single sideband effect

4.5.1 Influence of beam coherence on phase plate applicability

For the application of the Zach phase plate in the Zeiss EFTEM 923 it is necessary to use a condenser aperture to produce a diffraction image with high spatial coherence in the back focal plane of the objective lens. This is necessary to provide a sharp and well-defined position of the zero order beam for an accurate phase plate positioning. Furthermore the used illumination angle should not be larger than 0.5 mrad to prevent fast phase plate tip contaminations by the spread and extension of the zero order beam. Hence illumination angles of 0.32 mrad and 0.2 mrad were used for the epon sections sample and the cryo sample.
As condenser aperture the Zeiss EFTEM 923 provides a 5-hole apertures with hole diameters of 600 µm, 300 µm, 150 µm,75 µm and 37 µm. Best performance is provided with the smallest aperture of 37 µm positioned in the center of the 5-hole aperture. However this aperture can only be used for nominal magnification of 75.000x or higher. The second aperture with opening diameter of 75 µm also still offers a diffraction image with adequate imaging conditions and can be used for minimum nominal magnification of 50.000x or higher. This larger aperture was used for both samples presented in this chapter. For a smaller nominal magnification the aperture limits the field of view. The three larger aperture of the 5-hole condenser aperture do not provide enough spatial coherence for the zero order beam and can therefore not be used for phase contrast imaging. Due to this phase contrast image acquisition for larger sample details then the ribosomes in the mouse diaphragm sample embedded in epon is not possible. Image acquisition of the collagen fibres in cross and longitudinal view as well as the adjoining cell nucleus in the right upper image corner would have been of interest. However their spatial frequencies have an even smaller distance to the zero order beam then the spatial frequencies of the

ribosomes. This would already result in lower phase contrast when using this particular Zach phase plate.
The spreading of the zero order beam in the diffraction plane for larger condenser aperture is also critical for aperture switching during one image acquisition session with aligned Zach phase plate. This aperture switching is needed for example in standard Cryo-TEM of singe particles. Here an overview image at low nominal magnification with large aperture is taken to choose the exact position for image acquisition at high magnification with smaller aperture. If the Zach phase plate is position at its proper place next to the zero order beam at e.g. a nominal magnification of 50.000x, a change to a smaller nominal magnification (e.g. 6000x) with aperture change results in a partially obstruction of the zero order beam by the phase plate tip due to the beam spreading. The consequences are a very fast contamination and charging of the phase plate tip and a resulting non interpretable image contrast, similar to a mixture between bright field and dark field contrast.

4.5.2 Contamination and lifetime of Zach phase plates

Lifetime of the used electrostatic Zach phase plates is very different and an average durability can not be indicated at the current state of technologies. As the electrostatic phase plates are still manufactured in one-off production, there are plenty of sources of error, which might cause early functional failure.
The phase plate PP1 used for the image acquisition of ribosomes embedded in epon in section 4.3 had a life time of 10 days of application, distributed over 2 month of installation time inside the microscope. The phase plate PP2 used for the image acquisition of the F-actin filament embedded in vitreous ice in section 4.4 had a life time of 25 days of application, distributed over 5 month of installation time inside the microscope.
When the phase plate begins to become unusable, the Power Spectra of the acquired images showed strong deformations of the Thon rings due to phase plate charging. Furthermore the leaking current between central electrode and grounded shielding layers was increased over ±40 µA at an applied voltage of ±0.2 V. This made the phase plate unusable for phase contrast imaging.
The number of application days compared to the installation time is relative small. One reason for this is the need for some regeneration days after the phase plate has been contaminated and charged by extensive use. This application period can have a duration between one and three days. The duration of a regeneration period depends whether the phase plate is adapted with an heating system for contamination reduction or not. If no heating system is adapted, the only possibility to reduce phase plate charging is to wait for some days until some of the contaminations on the phase plate have been removed by

the vacuum system of the microscope. The vacuum values in the vicinity of the phase plate should be better than 2.0 10^{-7} mbar. The use of an anti contaminator also helped to reduce the contamination effect. It was used in both phase plate experiments. The average regeneration time without heating system was one week. This process can only be repeated three to four times before the phase plate tip gets saturated with contamination. In this case the phase plate is not usable any more, because the contaminations at the tip form a conducting bridge between the central electrode an shielding outer layers. This leads to a increased leakage current between these layers and with this to an decreasing maximal applicable potential to the phase plate.
If the phase plate is adapted with a heating system the regeneration time is reduced to one to three days. In addition the overall life time was extended by a factor of 2 - 3. This was the case for the Zach phase plate "PP2" used for the image acquisition of F-actin filaments embedded in vitreous ice in section 4.4. Due to the heating process the breakdown voltage of the isolating layers of the phase plate are reduced, resulting again in a reduced maximal applicable phase plate potential. Observations during phase plate application showed that the regeneration of this material property takes one to three days. Hence a simultaneous use of the phase plate and the heating system is not possible. Furthermore, extensive and too fast heating rates can also damage the phase plate. Fractures can appear inside the material layers or parts of a layer can peel of completely.

4.5.3 Influence of spatial frequency obstruction by the phase plate structure

The positioning and the size of the phase plate structure have a large influence on image appearance resulting from spatial frequency obstruction. This influence is, of cause, best visible for large sample structures with small spatial frequencies. This is due to the larger fraction of obstructed Friedel symmetric spatial frequencies by the phase plate tip, compared to higher spatial frequencies with larger radial distance to the zero order beam. The results from phase contrast imaging of ribosomes embedded in epon show, that the used phase plate geometry does not match with the size of the sample. Due to the positioning of the phase plate as close as possible to the zero order beam, the corresponding spatial frequencies of the ribosomes are affected by single sideband contrast. The reached phase shift with highest applicable phase plate potentials is too small for an immediately visible change in phase contrast, as the spatial frequencies of the ribosomes are too near to the cut-on frequency of the phase plate and due to the dominance of single sideband contrast. By image subtraction a change in phase contrast is visible.
The Cryo-TEM phase contrast images of F-actin show that by reducing the phase plate dimension an inverted phase contrast can be produced by applying different potentials

to the phase plate electrode. The position of the phase plate tip relative to the filament orientation results in single sideband contrast for filaments arranged perpendicular to the phase plate. For this filament the single sideband contrast is dominant with regard to the phase contrast change.

However, the steep gradient of the spatial potential distribution producing a soft cut-on frequency for the Zach phase plate showed no negative influence on the phase contrast formation in the images acquired with PP1 or PP2. In contrast it proved to prevent edge artefacts as they show up for example when using film phase plates with a step like cut on frequency [29].

In general it can be said, that reducing the phase plate tip dimension reduces the relative amount of obstructed spatial frequencies in diffraction space and with this the single sideband contrast. The reduction of central electrode width reduces the cut-on frequency and allows the use of the phase plate when imaging larger objects. Due to technical limitation a further reduction of the tip width below 1 µm is not possible at this time. Hence an application of the phase plate to a magnified diffraction plane is a possibility for further improvement of phase contrast image acquisition.

4.5.4 Numerical correction of single sideband effect

The remaining single sideband contrast can theoretically be corrected by image processing. As the related frequencies are obstructed only from one side in diffraction space by the Zach phase plate bar, their information still remains in the not obstructed Friedel symmetric frequencies. Due to this the obstructed regions are not completely blocked out in the Power Spectra, but are visible with an reduced intensity by a factor of 2 in these regions. The numerical correction process for a Boersch phase plate is already described in [34]. The numerical correction process for a Zach phase plate is identical, expect that the correction has to be done for only one instead of three bars. According to [34] the blocking of spatial frequencies $q_{x,\mathrm{PP}}$ by the phase plate bar can be described as aperture function

$$A_{\pm}(q_{x,\mathrm{PP}}) = \frac{1}{2}\{1 \pm \mathrm{sign}(q_{x,\mathrm{PP}})\}. \tag{4.1}$$

with the sign function

$$\begin{aligned} \mathrm{sign}(q_{x,\mathrm{PP}}) &= -1 \qquad q_{x,\mathrm{PP}} < 0 \\ &= +1 \qquad q_{x,\mathrm{PP}} \geq 0. \end{aligned} \tag{4.2}$$

The single sideband affected contrast transfer function ($\mathrm{pCTF_{ssb}}$) is then described in 3D by

$$\begin{aligned} \mathrm{pCTF_{ssb}}(\mathbf{q}) &= \sin \mathrm{W_{PP}}(\mathbf{q}) + \mathrm{i}\ \mathrm{sign}(q_{x,\mathrm{PP}}) \cos \mathrm{W_{PP}}(\mathbf{q}) \\ &= \mathrm{i}\ \mathrm{sign}(\mathbf{q}) \exp\{-\mathrm{i}\ \mathrm{sign}(q_{x,\mathrm{PP}}) \mathrm{W_{PP}}(\mathbf{q})\}, \end{aligned} \tag{4.3}$$

whereas

$$W_{\mathrm{PP}}(\mathbf{q}) = \frac{\pi}{2} \left(C_{\mathrm{S}} \lambda^3 \mathbf{q}^4 + 2\Delta z \lambda \mathbf{q}^2 \right) + \phi_{\mathrm{PP}} \tag{4.4}$$

is the aberration function including the phase shift by a phase plate ϕ_{PP}.

For equation 4.3 the following relation holds:

$$\mid \mathrm{pCTF_{ssb}}(\mathbf{q}) \mid^2 = 1. \tag{4.5}$$

From equation 4.5 it appears that there is a constant signal transfer over the spatial frequency range affected by the phase plate bar. This is the reason why there are no Thon rings in the areas of Power Spectra where the phase plate bar is visible (c.f. figure 4.3 and figure 4.4). The phase contrast images can therefore be corrected for the single sideband contrast and the CTF by multiplying the phase plate affected spatial frequencies in Fourier space with the inverse function

$$\mathrm{pCTF_{ssb}}(\mathbf{q})^{-1} = -\mathrm{i}\ \mathrm{sign}(\mathbf{q}) \exp\{\mathrm{i}\ \mathrm{sign}(q_{x,\mathrm{PP}}) \mathrm{W_{PP}}(\mathbf{q})\}. \tag{4.6}$$

The non affected spatial frequencies have to be multiplied in Fourier space with the inverse function

$$\mathrm{pCTF}(\mathbf{q})^{-1} = \frac{1}{2} \sin^{-1} \mathrm{W_{PP}}(\mathbf{q}). \tag{4.7}$$

In the practical application of this correction procedure some problems arise: Firstly the exact position of the phase plate bar has to be determined from the Power Spectra images. Due to the low electron does used for image acquisition the signal to noise ratio is very low. This makes an automatic edge detection of the phase plate structure very difficult. The detection has to be estimated by a hand drawn mask, which also has some uncertainties. Until now all attempts for an numerical correction of phase contrast images with applied Zach phase plates have not been satisfying.

4.6 Conclusion

Electrostatic Zach phase plate imaging with tunable phase contrast on biological samples is demonstrated in this section. The application of the first electrostatic Zach phase plate and the imaging of ribosomes embedded in epon show that the phase plate dimensions are too large for sufficient relative phase shift of spatial frequencies belonging to object of this size. The frequencies are still located in the cut-on frequency band of the phase plate. In addition this leads to a dominant single sideband contrast in the images.
With smaller phase plate structure and smaller sample diameter tunable and invertible phase contrast imaging works very well. This is shown on the F-actin filaments embedded in vitreous ice. Also the soft cut-on frequency induced by the steep gradient of the spatial electrostatic potential distribution shows no negative influence on the contrast formation but prevents the formation of edge artefacts. However single sideband contrast still remains and dominates for filaments - and thus any structures - with perpendicular orientation to the phase plate bar.
The life time of the electrostatic phase plate could be extended by a factor or 2 - 3 by the use of a heating system for contamination reduction.
To reduce image artefacts by single sideband contrast the phase plate dimensions should be as small as possible. Furthermore the diffraction plane can be enlarged to reduce this unwanted effects.
Numerical correction of single sideband contrast is also theoretically possible. However processing attempts do not show satisfying results due to low SNR of the images and hence resulting difficulties in accurate phase plate edge detection in Power Spectra images (results not included into this thesis).

5 Adaptation and application of the electrostatic Zach phase plate for TEM with Diffraction Magnification Unit

In this chapter the first application of the electrostatic phase plate combined with a Diffraction Magnification Unit is discussed. First unexpected strong charging effects and prospects for reduction of this effects are analysed. Then the results for the application of a Zach phase plate for phase contrast imaging with the Diffraction Magnification Unit is presented. Afterwards the influence of different cover layers materials on phase plate charging reduction are discussed as well as the influence of projected potential distributions for different phase plates geometries on the expected phase shift.

5.1 Adaptation of phase plate design for application in Zeiss Libra 200 DMU

As shown in chapter 4 the electrostatic Zach phase plate works well for applying tunable phase contrast to biological sample embedded in vitreous ice. The remaining problems are the single sideband contrast for sample features oriented perpendicular to the phase plate bar and an insufficient relative phase shift for large objects like the ribosomes which spatial frequencies are affected by the soft cut-on frequency of the phase plate. To address these problems the phase plate tip can be reduced in width to obstruct less spatial frequencies. The other possibility is to use a magnified diffraction plane. In the following experiments both modifications are done. The tip width is reduced from 1.3 µm to 1.0 µm and the central electrode width from 500 nm to 140 nm. Due to technical limitations a further size reduction is currently not possible. Phase plates with thinner tips are currently mechanical unstable and brake during the manufacturing process. Also an enlargement of the phase plate aperture diameter above 90 µm with a tip width of 1 µm leads to mechanical instabilities. Phase plates with aperture diameters of 180 µm and 470 µm have

been produced and applied but both had large tip widths of 1.6 µm and 6.5 µm. To reduce the effect of the cut-on frequency, they are tested in the Zeiss Libra 200 DMU. Compared with the Zeiss EFTEM 923 this electron microscope provides a diffraction plane inside the DMU which is 6.1x times larger then the back focal plane of the objective lens in the Zeiss EFTEM 923. This magnification factor arises from a larger focal length of the objective lens by a factor of 1.7x (focal length EFTEM 923 = 2.7 mm, focal length Libra 200 DMU = 4.6 mm) and the combination of adaption lens with the diffraction magnification lens (figure 2.7), that images a second diffraction image inside the DMU with a magnification factor of 3.6x.

5.2 Contamination effects

During the first applications of the electrostatic Zach phase plate with the Zeiss Libra 200 DMU an enormous increase in contamination and charging effects was observed. These effects appeared straight from the first application day after mounting the phase plate into the microscope. Thus this contaminations could not be addressed only to hydrocarbons adhering to the tip during hitting it with the zero order beam but had to be present even before mounting the phase plate into the Zeiss Libra 200 DMU. These contaminations could also not be removed only by heating the phase plate with the adapted heating system. Different experiments for characterization and elimination of these increased charging effects are discussed in this section.

5.2.1 Sample preparation, microscope and phase plate specifications

In the following experiments a cross grating replica and negative stained bovine liver catalase crystals are used as samples. The cross grating replica (Plano Inc., Germany) consist of a structured carbon layer, covered with gold and palladium, placed on a copper sample grid. The cross line spacing is 2160 lines per mm.
For the sample preparation of the negative stained bovine liver catalase crystals, 1 µl of catalase crystals in buffer solution (SERVA, Germany) is pipetted onto a sample grid and stained twice by applying 5 µl of unbuffered 2% aqueous uranyl acetate solution and drying the grid with filter paper. As sample grid a Quantifoil Holy carbon film grid is used, with 200 Cu mesh, carbon film thickness of 10 - 20 nm, hole diameter of 0.6 µm and hole distance of 1 µm. As the catalase crystals fragments have an average size of 2 - 10 µm, they can be deposit onto the holy carbon film without any difficulty. The salt containing the heavy metal uranyl is deposit above the catalase crystals and builds a close surrounding layer. The proteins inside the catalase retain some water during the drying process of the uranyl salt. Due to the lower atomic numbers of the atoms in the sample

and the surrounding water, compared to the uranyl salt, more electrons pass through the sample region with a thin uranyl layer on top then through a region containing only uranyl salt. The higher scattering rate in the pure uranyl salt layer leads to bright appearance of the sample on a dark background [45].
The catalase crystal has two typical lattice spacings, $c_0 = (17.5 \pm 0.2)$ nm and $a_0 = (6.85 \pm 0.07)$ nm [46]. The corresponding diffraction spots are visible in the power spectra at $q_{c_0} = 1/17.5\ \text{nm}^{-1}$, $q_{a_0} = 1/6.85\ \text{nm}^{-1}$ and their integer multiples.
The Zach phase plate used for this experiment is called "PP3". The corresponding dimensions are listed in table 4.1. A SEM image of this phase plate is shown in figure 5.1. The charging effects reported in the following section are not limited to the phase plate "PP3", but where also observed with other phase plates mounted in the Zeiss Libra 200 DMU.

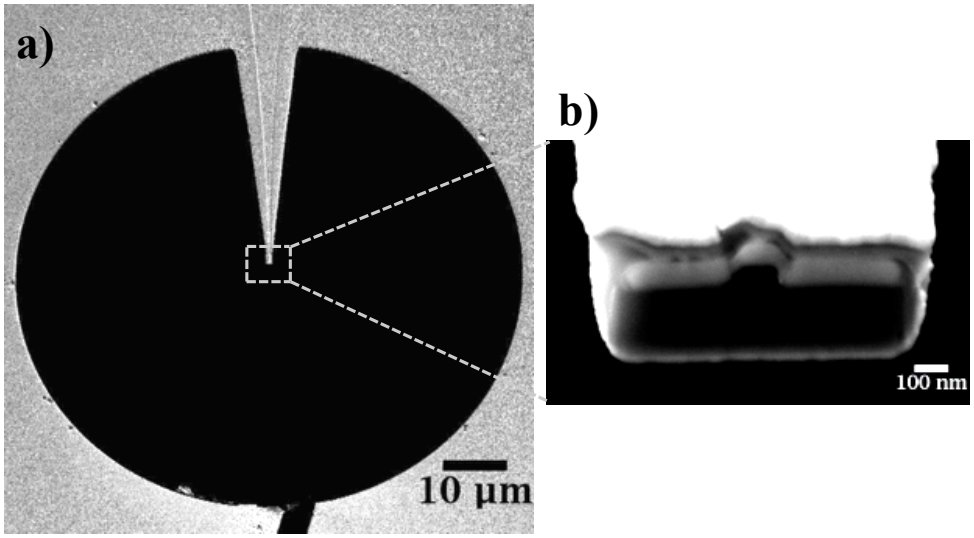

Figure 5.1: Figure a) SEM image of the phase plate "PP3" used with the Zeiss Libra 200 DMU for charging reduction experiments and for image acquisition of phase plate induced phase contrast images . Figure b) zoomed out phase plate tip. Images acquired by S. Hettler, KIT.

5.2.2 Experimental results

To reduce the amount of charging effects observed with the phase plates in the Zeiss Libra 200 DMU, when mounting the phase plate into the microscope without any pre-treatment, different pre-treatment steps are tested. All steps include plasma cleaning to remove superficial hydrocarbons contaminations. For plasma cleaning a Gatan Solarus Model 950 Advanced Plasma System, with an Argon flow rate of 35 sccm is used. Carbon coating is done with a Leica EM MED020, including an oscillating crystal unit (Leica EM QSG100) for layer thickness measurement.

- **Treatment 1:** the phase plate is cleaned with argon plasma for 5 minutes, at a radio frequency (RF) power of 50 W and a pressure of 9.3 Pa. Afterwards it is transferred and mounted into the microscope under ambient conditions.
- **Treatment 2:** the phase plate is cleaned with argon plasma for 60 minutes at a RF power of 50 W and a pressure of 9.3 Pa. This time transferred and mounted under N_2 gas atmosphere.
- **Treatment 3:** the phase plate is cleaned with argon plasma for 30 minutes at a RF power of 50 W and a pressure of 9.3 Pa, then coated from both sides with a 2.6 nm thick layer of amorphous carbon (a-C) and afterwards transferred and mounted into the microscope under ambient conditions.

Treatment 1 and 2, including only plasma cleaning and mounting under ambient conditions or under N_2 gas atmosphere do not reduce the charging effects or only slightly, but not sufficient enough. However treatment 3 including coating with amorphous carbon reduces the charging effect drastically. Figure 5.2 shows Power Spectra with changing charging effects for the three pre-treatment tests and for the application without any pre-treatment. The images show always the same phase plate "PP3". The treatment where applied consecutively, hence the initial conditions for each treatments 1, 2 and 3 are different.
Figure 5.2 a) shows sample and the corresponding Power Spectra for application of PP3 without any pre-treatment. Strong astigmatic aberrations of the Thon rings are visible.
Figure 5.2 b) shows sample and the corresponding Power Spectra after treatment 1. A astigmatic deformation of the Thon rings in the power spectra is stronger than in figure 5.2 a) and shows a butterfly shaped form. Due to the grade of Thon ring deformation, PP3 seams to be contaminated with even more hydrocarbons after treatment 1, than before treatment 1.
Figure 5.2 c) shows sample and the corresponding Power Spectra after treatment 2. Plasma cleaning for 60 minutes reduces clearly charging effects induced by hydrocarbons. However residual charging remains and is visible in the Power Spectra. This charging can also not be removed by additional heating of the phase plate system. Here the mounting under N_2 gas ambience does not contribute significantly to a reduced phase plate charging. This conclusion is based on the observation, that treatment 3 imaged in figure 5.2 d), shows better performance without mounting PP3 under N_2 gas ambience. However the mounting process under N_2 gas ambience did include steps, where PP3 had to be transported for short times through normal room air. This included the way between plasma cleaner and mounting box and the way between mounting box and microscope port. Due to this the effect of a N_2 gas ambience might be adulterant.

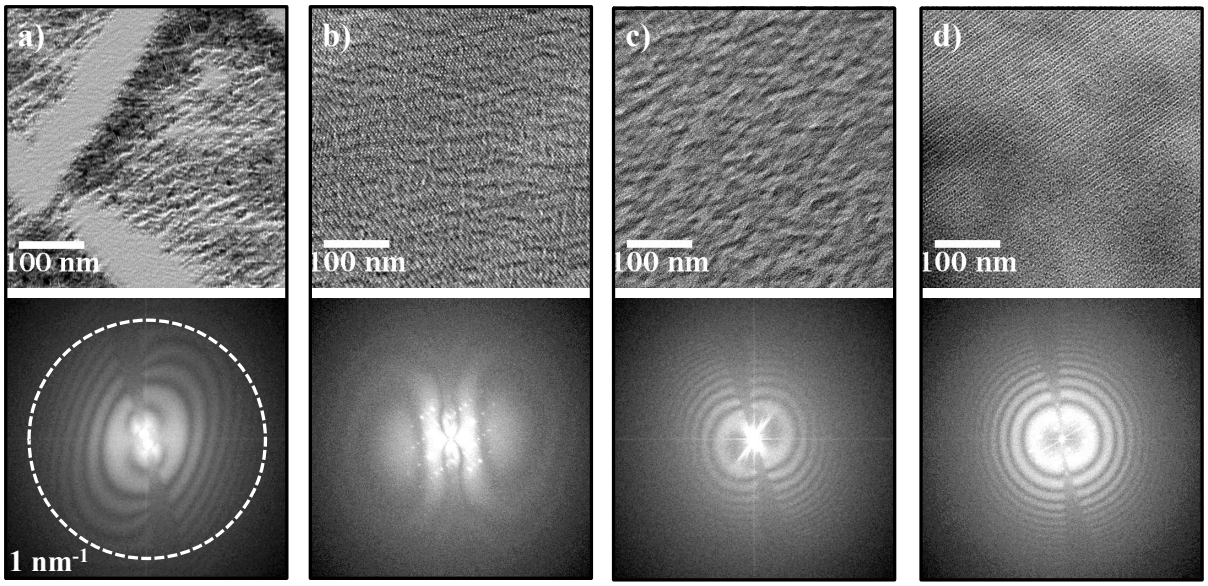

Figure 5.2: Images and corresponding Power Spectra for Zach phase plate PP3 application in the Zeiss Libra 200 DMU. Shown samples are a cross grating in a), catalase crystals in b) and d) and carbon layer of a Quantifoil grid in c). Defocus values are $\Delta z = 1$ µm in a) and b), $\Delta z = 2$ µm in c) and d). Figure a) without any pre-treatment. Figure b) after treatment 1: Ar plasma cleaning for 5 min., installation under ambient conditions. Figure c) after treatment 2: Ar plasma cleaning for 60 min., installation under N_2 gas ambient. Figure d) after treatment 3: Ar plasma cleaning for 30 min., 2.6 nm thick amorphous carbon (a-C) coating, installation under ambient conditions. Pre-treatments without a-C coating show still charging effect by deformations of the Thon rings in a) - c). a-C coating eliminates the charging effect and deformation of the Thon rings in d).

Figure 5.2 d) shows sample and the corresponding Power Spectra after treatment 3. Coating PP3 with amorphous carbon shows a significant reduction of charging effects in the Power Spectra. Astigmatism is removed. Only very small Thon ring deformations are left over at the immediate vicinity of the phase plate edges.

Charging does not only apply to the phase plate tip but also the phase plate aperture and the whole phase plate carrier system. Figure 5.3 a) shows an image of a catalase crystal acquired without a phase plate, at an under-focus of $\Delta z = 2$ µm and its corresponding Power Spectra in 5.3 b). No charging effects are visible. Figure 5.3 c) shows butterfly wings shaped Thon ring deformation when the phase plate tip of PP3 is located at a distance of 3.5 µm from the zero order beam. Figure 5.3 d) shows the influence on the Thon rings by driving the tip out from the center up to a distance of 22 µm. The aperture border has then a distance of 17 µm to the zero order beam. The butterfly wing shape changes toward a strong astigmatism. Figure 5.3 e) and g) show low magnification images of a sample grid with different distances of the phase plate carrier system from the image

center. The charging of the carrier system made of brass produces strong Thon ring deformations. This is shown in the Power Spectra in figure 5.3 f) and h). These are Power Spectra of images acquired at the same magnification and same area as image 5.3 a) but with the phase plate carrier system made of brass positioned as shown in image 5.3 g) and j). All images in figure 5.3 belong to the phase plate plasma cleaned for only 5 minutes (treatment 1).

As the whole phase plate system is affected by the charging effect, independent of the surface material, it is not clear what the sources for the charging effects are. Some possibilities are:

a) They arise from surface contaminations by hydrocarbons, deposit not only on the phase plate but also on the brass carrier plate.

b) The charging effect can also be produced by an additional electron accumulation above or around the phase plate, produced by knocking out secondary electrons with the zero order beam or scattered electrons due to the low work function of the surface materials (gold for the phase plate, aluminium and brass for the carrier system).

c) The charging effect occurs due to the formation of an very thin gold-oxide layer on top of the phase plate, which is an insulator and therefore cannot discharge any sticking charged contamination.

This proposals are discussed in more detail in section 5.4.1.

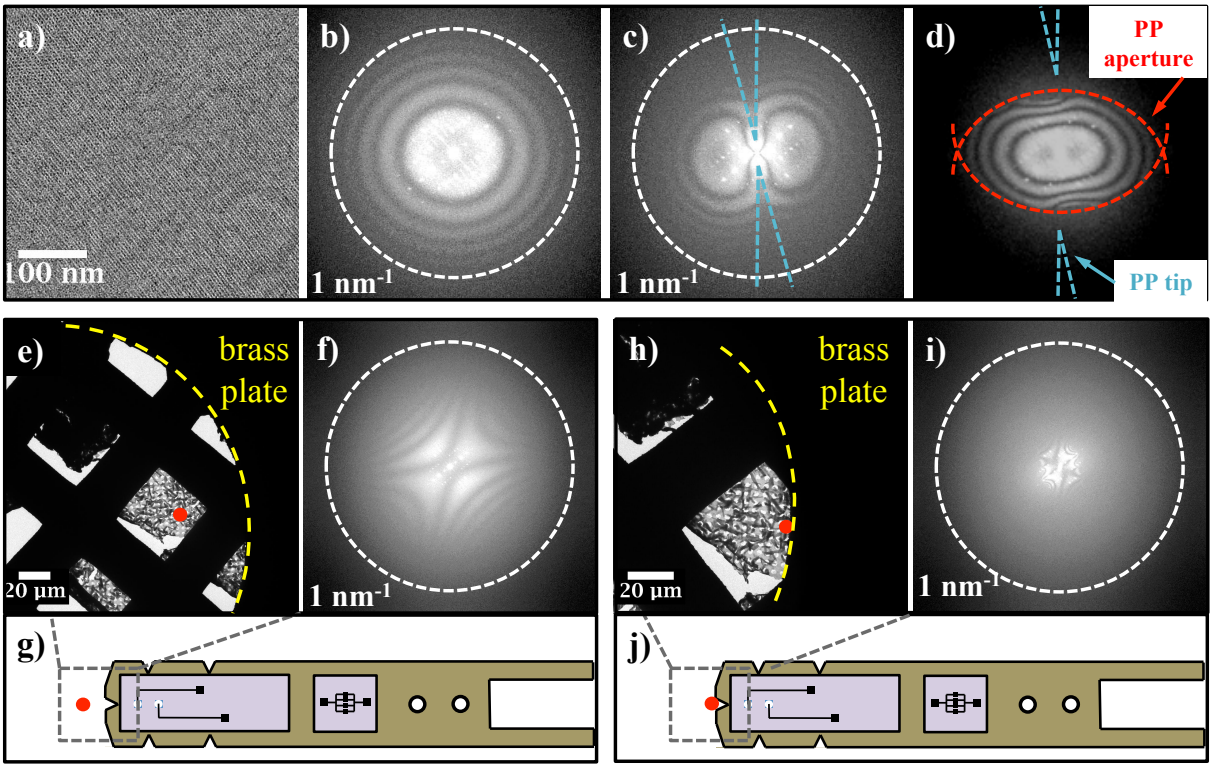

Figure 5.3: Charging effects on Zach phase plate PP3 used in the Zeiss Libra 200 DMU after treatment 1. a) shows negative stained catalase crystals used as sample. b) corresponding Power Spectra at 1 µm under-focus without inserting PP3 shows round Thon rings. c) same sample area but with inserted PP3 at 3.5 µm distance from the zero order beam, shows charging of the phase plate as "butterfly wings" deformation of the Thon rings. d) PP3 at a distance of 22 µm and aperture at a distance of 17 µm from the zero order beam. Charging still appears as elliptical Thon ring deformation. Also the brass phase plate carrier system induces Thon ring deformation due to charging. e)+g) and h)+j) shows distance of the brass plate from the sample area (red dot) for image acquisition. f)+i) show Power Spectra of images acquired at the same magnification as a) and in-focus. They demonstration the influence of the charged brass plate.

However the phase plate after treatment 3, which includes carbon coating, shoes an immediate elimination of the charging effects that appeared right after the phase plate installation. It is possible to work with this coated phase plate for approximately 2.5 hours at an electron dose of 22 $e^-/Å^2$ and 4 hours at an electron dose of 9 $e^-/Å^2$. After this time a second type of charging start to appear. Its source is assumed to be the surface contamination by hydrogen compounds still present in the microscope vacuum. These molecules are "guided" by the zero order beam due to their positive ionisation charge and adhere to the phase plate structure. Figure 5.4 shows images and Power Spectra of catalase crystals acquired in under-focus and focus with the inserted coated phase plate PP3. The reduced charging can be seen clearly in the Power Spectra. These secondary charging effects appearing after a longer exposer time can be removed by heating the system with the adapted heating system at 60 °C for approximately 12 - 18 hours with a following cooling phase of approximately 4 hours. A shorter heating time of 4 hours did not remove all contaminations. Charging effects were still visible. Heating was mostly done over night and the phase plate performance was tested the next day. Thus no experience regarding shorter heating times between 4 and 12 hours with a carbon coated phase plate is available yet.
After the carbon coating process, the central and shielding gold layers at the phase plate tip are not anymore electrically isolated from each other, but are connected by the conductive carbon layer. Thus no electrostatic potential can be build up at the tip. The phase plate tip has to be cut again to disconnect again this gold layers from each other. This is done by using a focused ion beam with Ga^+ ions for the cutting process. After demounting, cutting and a second installation into the Zeiss Libra 200 DMU, the carbon coated PP3 shows again a slightly increase in charging effects.
Phase plate exposure and subsequent heating in the microscope can be repeated several times. The effect of contamination reduction by heating is reduced slightly after every cycle. After about five cycles the carbon coated phase plated showed some charging effects even after 12 hours heating period. Every phase plate application period had a duration of about 3 - 5 hours. Four of five heating phases had a duration of 12 - 15 hours and one had a duration of 4 hours. In total the carbon coated phase plate PP3 showed a lifetime of approximately 20 hours during a total of 5 application days. Afterwards the heating system break down due to a short-circuit. Due to this a further application of this phase plate was not possible. It is most probable that the carbon coated phase plate can be used even beyond the 20 hours of application. After these encouraging results carbon coating of phase plates need to be investigated in more detail in future work.

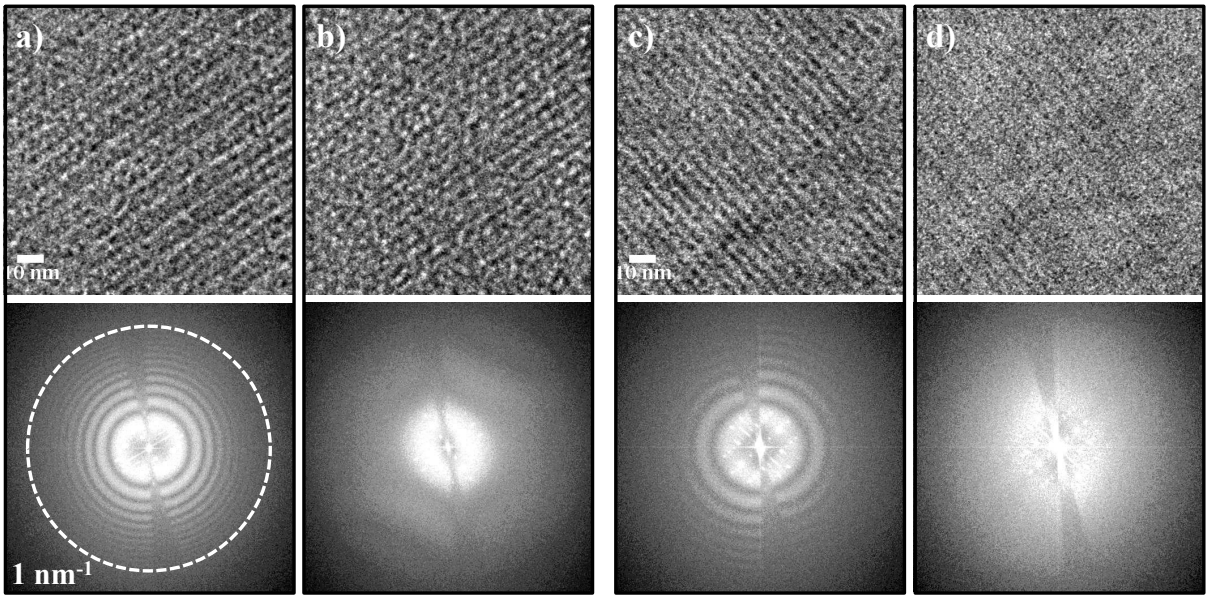

Figure 5.4: Charging effects on a-C coated Zach phase plate after longer exposure time and after heating for 18 hours. Figure a) and b) catalase crystals and corresponding Power Spectra after an application time of 3 hours. Figure a) at 2 µm under-focus, figure b) in-focus. Starting charging effects are best visible in-focus as astigmatic Thon ring deformation, which also influences the appearance of the crystals in the image b). Figure c) and d) catalase crystals and Power Spectra after heating for 18 hours at 60 °C. Figure c) at 1 µm under-focus, figure d) in-focus. Charging effects are removed. This is best visible in the constant contrast transfer of the focused Power Spectra in figure d), where no aberrations are visible as Thon ring deformations.

5.3 Zach phase plate imaging with a magnified diffraction unit

5.3.1 Sample preparation, microscope and phase plate specifications

After addressing the problem of contamination effects by coating the phase plate, experiments on phase plate imaging combined with a DMU for tunable phase contrast are carried out. Negative stained catalase crystals are used as sample. The sample preparation is the same as described in 5.2.1. Also the used phase plate and the corresponding dimensions and respective layer thickness are the ones listed in table 4.1 under "PP3".

5.3.2 Experimental results

For the phase contrast imaging several images of the same sample area are acquired, each with an electron dose of 22 $e^-/Å^2$. For comparison first an image without phase plate is acquired with 5.66 µm under-focus. Then the phase plate is positioned in the back focal

plane and images with applied phase plate potentials of 0, -2 and -4 V at an under-focus of 5.66 µm are acquired. Afterwards the phase plate position is corrected and images with applied phase plate potential of 0, 2 and 4 V are acquired. Figure 5.5 shows the effect of the applied potential on the catalase crystals contrast and the corresponding Power Spectra. Figure 5.6 shows line scan diagrams across a region of the crystal structure, marked as white box in figure 5.5 a) and line scan diagrams along the Power Spectra radii, in direction of the q_{a_0} (blue box in figure5.5 b)) and q_{c_0} (red box in figure 5.5 b)) catalase diffraction spots.
Compared to figure 5.5 a) without phase plate, the a_0 lattice spacing of the crystals appear better resolved in figure 5.5 c) by inserting the phase plate and potential of 0 V. Applying a potential of -2 V in figure 5.5 d) shows no significant change in the image appearance. A potential of -4 V decreases the contrast and the lattice spacings a_0 resolution. The lattice spacings c_0 appearance is not significantly influenced by the different applied potentials. In all three images a 3D-effect of the catalase crystals and especially of the granular carbon film at the border of the crystal area is visible. A shading from the right to the left side is also visible. The corresponding Power Spectra in figure 5.5 f) - h) show that inserting the phase plate leads to a significant Thon ring shift toward smaller ring radius. Applying -2 V and -4 V increases again the Thon ring radius. Furthermore a strong astigmatic distortion is visible in all three images. Here the longer principal axis is always perpendicular oriented to the phase plate bar and the shorter principal axes is parallel to the phase plate bar. At 0 V and -2 V in figure 5.5 f) and g) the Thon ring radii seem to favour an increased contrast transfer for some multiples of the q_{a_0} diffraction spots. This might be responsible for the increased crystal structure resolution in figure 5.5 c) and d). A positioning correction of the phase plate for the next potential series (0, 2, 4 V) visible in figure 5.5 i) - n), shows a strong influence on the a_0 lattice spacings resolution. This resolution is significantly decreased in figure 5.5 i) at 0 V compared to figure 5.5 c) at 0 V and becomes even worth in figure 5.5 j) and k) by applying 2 V and 4 V to the phase plate. The 3D-effect of the catalase crystals and the granular carbon film is still present but less pronounced. The contrast of the granular carbon film appears also decreased by increasing the applied voltage. Also the Power Spectra in figure 5.5 l) - n) show a strong change in Thon ring spacing and an increased distortion at the phase plate tip boarders. The astigmatic distortion is still present and has the same principal axis directions as in figure 5.5 f) - h). Again the application of 2 V and 4 V increases the Thon ring radius. The increase of Thon ring radii for the application of both, positive and negative potential to the phase plate electrode, is an unexpected effect. Expected is an increased Thon ring radius for positive applied potential and a decreased radius for negative applied potential.

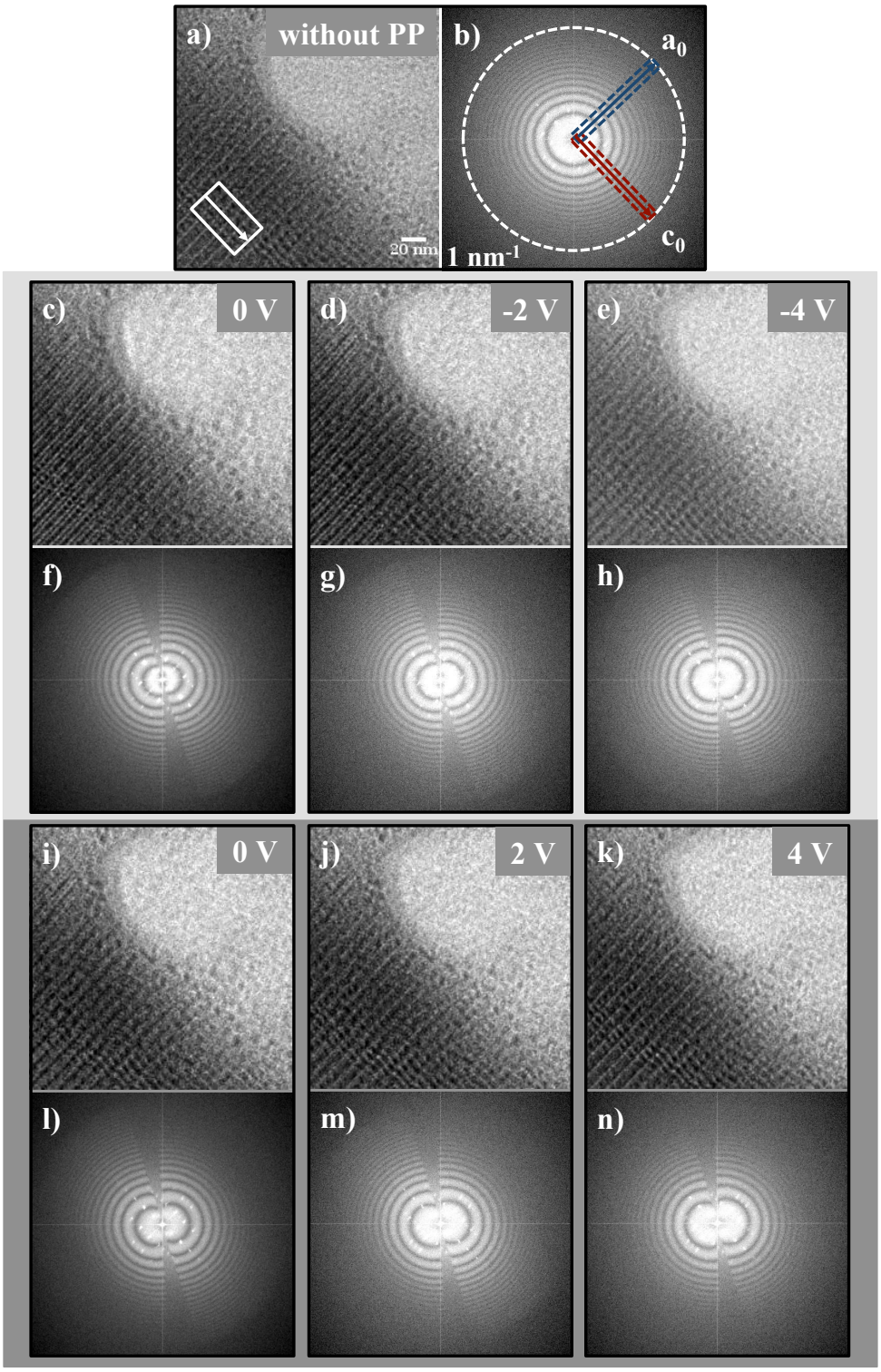

Figure 5.5: Negative stain catalase crystals imaged at $\Delta z = 5.66$ µm under-focus and Power Spectra. a) and b) without phase plate (PP), c) - h) with PP and potentials of 0, -2, -4 V. i) - n) with new positioned PP and potentials of 0, 2, 4 V. The white box in a) marks the region for the line scans shown in figure 5.6 a) + b). The blue and red box in b) marks the region for the line scans along the q_{a0} and q_{c0} diffraction spots, shown in 5.6 c) - f).

The significant reduction in Thon ring radius by inserting the phase plate without an applied potential indicates, that the phase plate has a positive charge offset, which is responsible for this Thon ring shift and the astigmatic distortions. This interpretation is also reinforced by the fact that for negative applied potential of -2 V in figure 5.5 h), no obvious change in contrast is visible compared to the application of 0 V in figure 5.5 g). Contrast change start to appear at -4 V in figure 5.5 i). However for positive applied potentials a change in contrast already is visible at 2 V in figure 5.5 c). This positive charge offset of the phase plate may be attributed to Ga^+ ion doping during the cutting process after carbon coating (cf. section 5.2).
This offset charge is predominant and thus prevents a significant contrast change for small spatial frequencies when changing the phase plate potential between 4 V and -4 V. This behaviour is clearly visible in figure 5.6 showing the line scan across the crystals, indicated as white box in figure 5.5 a) and line scans along the Power Spectra radii marked with blue and red boxes in figure 5.5 b). Here two line scans along the Power Spectra radii in direction of the spatial frequencies repetition of the catalase crystal lattice spacings q_{c_0} and q_{a_0} are made, instead of a rotational averaging the Power Spectra. This is done because of the strong astigmatism in the Thon rings.
The evaluation of the line scans along the Power Spectra radii in image 5.6 c) - f) show that a clear Thon ring phase shift starts to appear for spatial frequencies higher then 0.1 nm^{-1} in q_{a_0} direction and 0.12 nm^{-1} in q_{c_0} direction. For higher frequencies starting at 0.3 nm^{-1} it becomes visible, that the application of ± 4 V produces a phase shift of $\pi/2$ compared to 0 V application, in both direction. The frequency range where this phase shift start to appear is already influenced strongly by the damping envelope. This decreases the fraction of these frequencies to the contrast transfer and with this their influence on the image contrast appearance.
The arrows in c) - f) mark the q_{c_0} and q_{a_0} positions and their multiple values. In these frequency regions the contrast transfer for q_{c0}, q_{a0} and multiples is mostly even lower for the image with inserted phase plate at 0 V (black line), then for ± 2 V or ± 4 V (red and blue dotted lines). However the Power Spectra in figure 5.5 show that some of the higher order diffraction spots have an increased contrast transfer for 0 V and -2 V in f) and g). As the crystal structure appearance is also very sensitive on the phase plate positioning, the increased resolution for the a_0 lattice spacing visible in figure 5.5 c) and d) is not attributed only to a better contrast transfer of the crystal lattice spacings but is also due to single sideband contrast, affecting these frequencies.

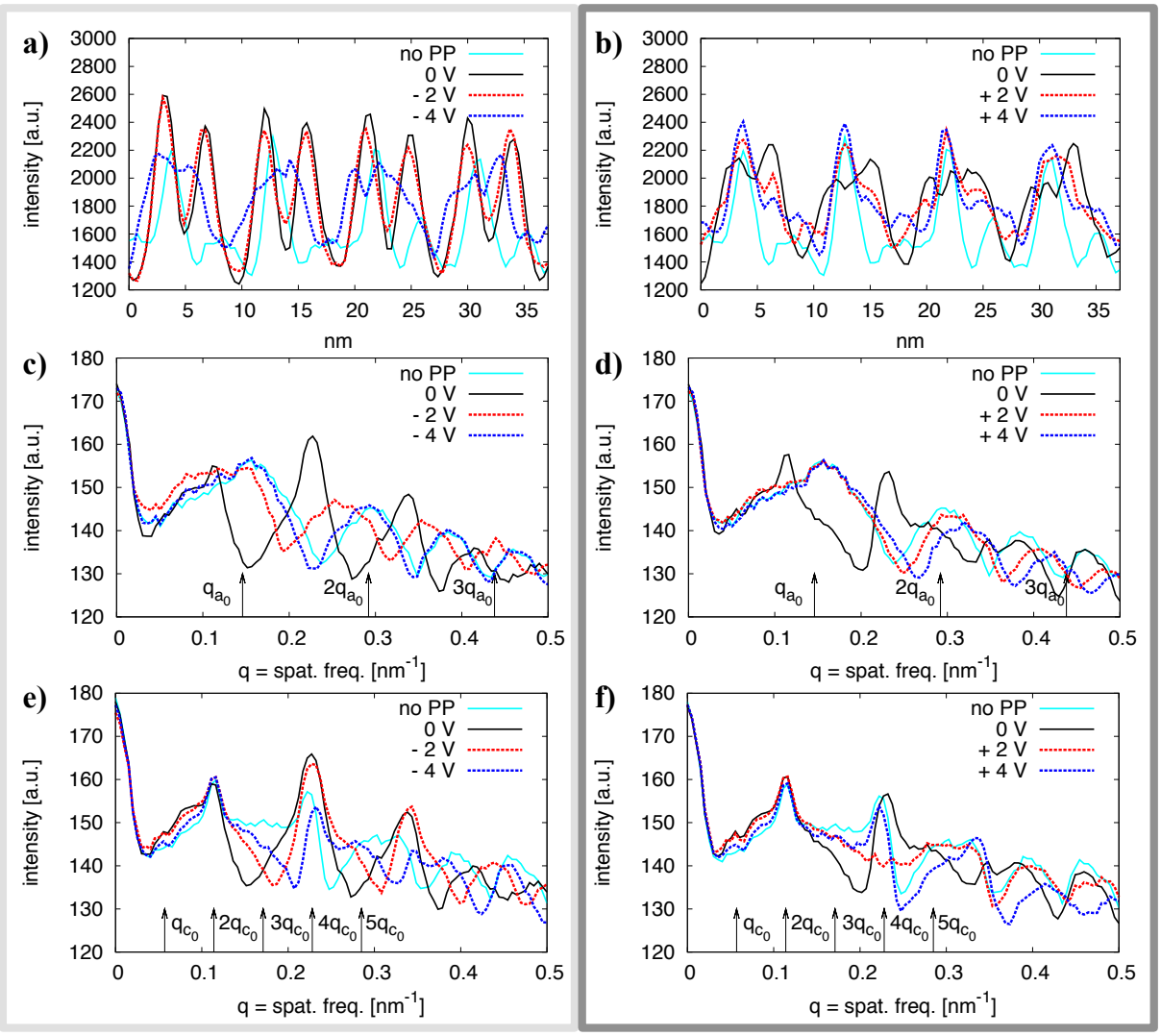

Figure 5.6: Line scans of image details, marked with a white box in image 5.5 a). Figure a) without phase plate (PP) and for applied potentials of 0, -2, -4 V. Figure b) without PP and for applied potentials of 0, 2, 4 V. Figure c) - f) line scans along Power Spectra radii, shown as red and blue box in figure 5.5 b). Figure c) + d) are along the q_{a0} reflections (blue box), e) + f) are along the q_{c_0} reflections (red box).

This experiment is repeated two times, whereby the phase plate position is corrected before every new potential series image acquisition. Here the distance of the tip to the zero order beam in perpendicular or parallel direction is slightly increased or decreased by approximately 100 nm steps by using the image tilt of the microscope. Potential between 0 V and +5 V or 0 V and -5 V are applied to the phase plate. Figure 5.7 shows rotational averaged line scans of the Power Spectra for applied potentials between 0 V and -5 V or 0 V and +5 V of these three different series, with slightly increased distance to the zero order beam. As example for the particular Thon ring distortion by phase plate charging, the Power Spectra for 0 V are also shown. The distance to the zero order beam slightly increases from series 1 to series 3. For the largest distance in series 3 (figure 5.7 e), f)) no change in phase shift is visible for different applied potentials. Even not for higher spatial frequency ranges, as is the case in a) and b). A more detailed analysis of this behaviour is discuses in section 5.4.2. The influence of the phase plate charging on the resulting distortion of the Power Spectra is always present but varies extremely in all three cases and seems not to be dependent from the distance of the phase plate to the zero order beam, as can be seen in figure 5.7 c) and d) for the intermediate distance. Reasons for this behaviour are discuses in section 5.4.1.

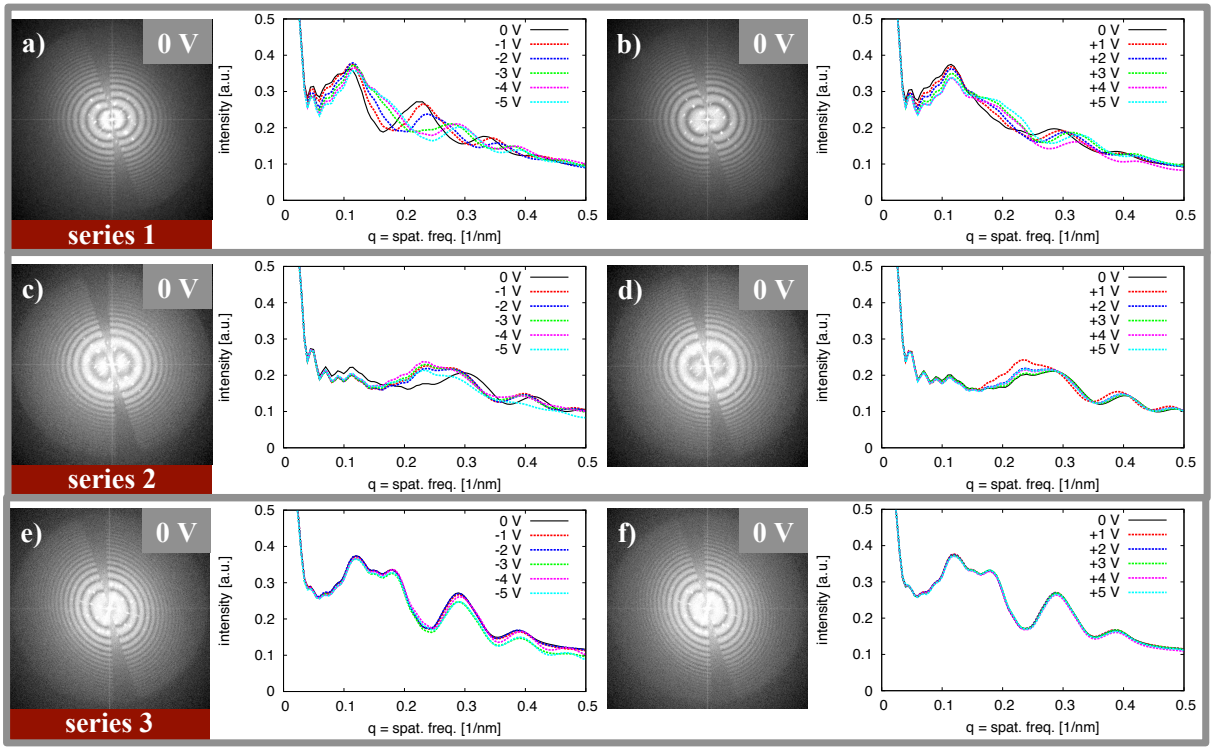

Figure 5.7: Rotational averaged line scans of Power Spectra for three different potential series, with slightly increased distance of the phase plate (PP) tip to the zero order beam. Power Spectra at 0 V show the particular Thon ring distortions. All images are acquired at $\Delta z = 5.66$ µm under-focus. Series 1 a) + b) with smallest PP distance shows strongest influence of different applied potentials on the resulting phase shift. Series 2 c) + d) with increased distance shows decreased phase shifts but clearly stronger charging effects. Series 3 e) + f) with the largest distance shows no impact on the phase shifts, however the smallest charging effects.

5.4 Discussion

The experiments recorded with the Zeiss Libra 200 DMU show that the application of a Zach phase plate with a DMU is much more sensitive on phase plate contamination and charging then in the application with the Zach EFTEM 923. The charging effect can be significantly reduced by coating the phase plate with a thin layer of amorphous carbon. A small change in the sample appearance can be seen by applying different potentials to the phase plate electrode, but is strongly dependent on the phase plate distance from the zero order beam and the occurring charging effects during the image acquisition. An inverted contrast is not achieved with the applied phase plate. In this section the following points are discussed:

- influence of carbon layers and other materials on phase plate charging
- influence of the projected potential for different phase plates geometries on the expected phase shift

5.4.1 Influence of phase plate coating

The coating of the phase plate with a thin amorphous carbon layer shows a significant reduction of charging effects. Additionally charging effects due to electron exposure during the application in the microscope can be removed by subsequent heating. After cutting the phase plate tip with the focused ion beam using Ga^+ ions, the phase plate showed a slightly increased charging. This is ascribed to the doping of the tip with Ga^+ ions during cutting. Here an alternative preparation method has to be established. A possibility would be to reduce the exposed surface of insulating layers at the phase plate tip by chemical etching. This would avoid or reduce the charging of these layers by the zero order beam. Moreover the originating gaps between the gold layers with a height of 100 - 200 nm would avoid a contact formation after coating the phase plate with a 2.6 nm thick carbon layer. The reasons for the differences of charging effects between the Zach phase plates used in an microscope with conventional optics compared to a microscope with DMU are not understood. The phase plate shown in figure 5.3 with extreme charging effects and without carbon coating was used in a Zeiss TEM 912, with 120 kV acceleration voltage at KIT for a comparison study. The phase plate was mounted without prior plasma cleaning but heated with the adapted heating system. Almost no charging effects where visible after a heating period of 12 hours.
Also the reasons for the significant differences in charging effect between the phase plate applied to a DMU without and with carbon coating are not totally clear. From the literature concerning nano and micro-scaled devices it is known that physisorbed layers

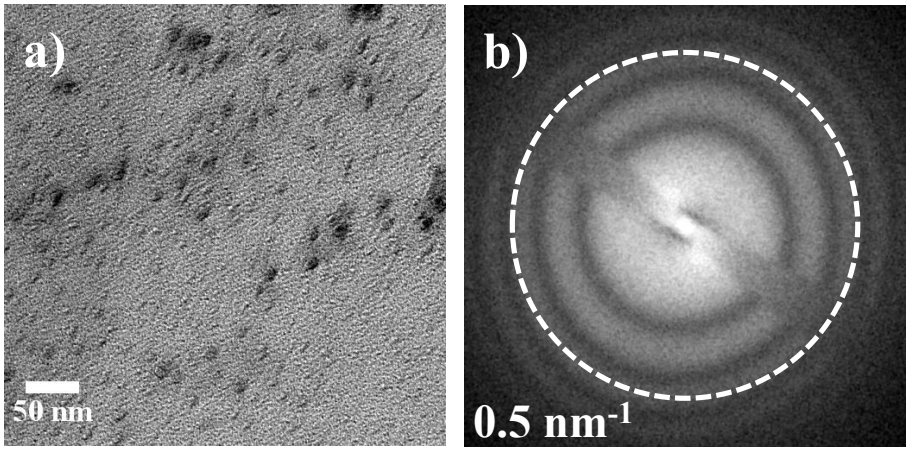

Figure 5.8: Application of a phase plate (PP) without a-C coating in a Zeiss TEM 912 at KIT. This PP showed strong charging effects as in figure 5.3 when operated in the Zeiss Libra 200 DMU. Before mounting into the Zeiss TEM 912 the PP was not plasma cleaned but heated at 50 °C for 12 hours. Figure a) sample consisting of CdSe nano particles. Figure b)corresponding Power Spectra. Almost no charging effects are visible. Charging is significantly reduced compared to the application in the Zeiss Libra 200 DMU. Image acquired by S. Hettler at KIT.

condense onto gold and other noble metals. This process appears in vacuum as well as under ambient conditions [47, 48]. At room temperature these contaminations consist mostly of hydrocarbons and water vapour [49–52]. The thickness of these contamination layers is affected by the pressure of the environment where the gold surface is stored and also on the gold surface appearance [53].

The clearly reduced contamination effects after treatment 3 including Ar plasma cleaning for a long exposure time of 60 minutes, confirms the reported effect that argon plasma can be used for removing organic and oxide contaminations [54]. It is also reported that argon plasma cleaning produce defects in gold surfaces, however only for argon environments with a pressure higher then 13 Pa [55]. As the plasma cleaning device used for the experiments described in this work was operated at only 9.3 Pa, defect formation on the gold surface is not expected.

Furthermore it is reported that the hydrocarbons and water vapour layers are very difficult to remove [56, 57] and that the layers start to grow again on gold surfaces, even after in situ plasma cleaning in ultra high-vacuum conditions of 10^{-6} Pa [56]. This is also in good agreement with the observed behaviour that contaminations where significantly reduced but not completely removed.

The physisorption of the hydrocarbons or water molecules on the gold surface is produced by the electrostatic interaction between induced and fluctuating dipoles due to Van der Waals forces or London dispersion force. Usually the binding energy for physisorption

is relatively low and is in the range of 4 to 40 kJ/mol. However this binding energy is strongly dependent on the adsorbing substrate. In the case of gold or every other conductive surface much higher binding energies can occur due to the interaction with image charges. This can be the reason, why charging could also not be removed by additional heating of the phase plate system.

The adsorbed hydrocarbons and water molecules are cracked during electron irradiation in the microscope, which results in polymerisation by cross-linking [58]. This leads to charge formation in this layer on the gold surface and with this to an induced charge in the metal surface. Due to this a very inhomogeneous electrical field is produced which affects the electrons passing near by this region. Furthermore secondary electrons are produced [58] that might be located around the phase plate structure causing an additionally fluctuation electrical field around the phase plate. This would lead to a positive charging of the phase plate, which is also in good agreement with the observation during the experiments.

Amorphous carbon has a lower secondary electron emission than gold [58,59]. Furthermore its conductivity is significantly lower than that of gold. Due to the disordered areas with sp^2 - graphen like and sp^3 - diamond like hybridization, there should be even areas with insulation character. Hence the binding energy for hydrocarbons or water molecules is less then for gold. Also the surface energy of carbon is smaller the that of gold [60], leading to less adhesion of molecules on carbon surfaces than on gold surfaces. This might explain why fewer hydrocarbons or water molecules adsorb to the carbon surface compared to the gold surface during the same exposure time to ambient conditions and why energy transfer due to heating is sufficient to remove the contamination from the carbon coated phase plate.

Furthermore it is reported that hydrocarbon reaction products are responsible for an increased resistance and with this to an increased charging effect [48] and not mobile physisorbed hydrocarbons. This is a further explanation why after an increased exposure time of the phase plate to the electrons in the electron microscope, the charging effect increases.

The assumption that the formation of a thin gold-oxide layer with low conductivity character could be the reason for the remaining charging, seems not to be correct. Due to the fact that gold is noble metal, an oxide does not arises from the exposure of gold to air, or due to a combustion process. However it can be produced by oxygen plasma treatment [61]. The only source where such an oxygen plasma could be in contact to the phase plate is the plasma cleaning process. Here remaining oxygen in the vacuum chamber after the evacuating process could be the source for the formation of oxygen plasma. However as the cleaning process is carried out using Ar plasma, this should remove emerging gold-oxide layers during the plasma cleaning process.

To prevent a reformation of hydrocarbons or water layers on the gold or carbon surface the phase plate would have to be packed into a non-reactive gas atmosphere. In this content it has been reported that continuous operation of MEMS (microelectromechanical systems) devices in a nitrogen environment immediately after plasma cleaning was the only procedure observed to indefinitely prolong device lifetime, meaning to ensure a low resistance of the gold contacts [48]. Also a repetitive cycling motion of a clean device in nitrogen may inhibit uptake of physisorbed hydrocarbon contaminants on the contacts.
The observations of mounting and transporting the phase plate under nitrogen ambiance did not show a reduction in contamination. This might be due to the fact that no closed nitrogen ambiance system could be used. The phase plate has to be transferred through ambient conditions between the plasma cleaner an the nitrogen box and later between the nitrogen box and the microscope. Furthermore the nitrogen concentration in the box could not be precisely measured and a contamination of the N_2 gas with oxygen, water and hydrocarbon molecules could not be excluded.
As the use of the phase plate in a nitrogen environment inside the microscope is not possible, another proposal for a further decrease of the contamination rate of the phase plate already under ambient conditions, is coating the phase plate with diamond like carbon instead of conventional amorphous carbon by sputtering. Diamond like carbon has a surface energies as low or even lower than PTFE (Teflon) [62], which is 18-20 mJ/m compared to 119 mJ/m for carbon and 1.5 J/m for gold [60, 63]. Furthermore it can be produced with a hydrophobic character. The electrical conductivity should be between the values for graphen and diamond, corresponding to its mixing ratio. Table 5.1 lists the surface energies and electrical conductivity values. These properties should decrease the adsorption of hydrocarbons and water molecules.

Table 5.1: Electrical conductivity and surface energies for gold, carbon, diamond like carbon and PTFE.

material	electrical conductivity σ [S/m]	surface energy [mJ/m]
gold	44.0 10^6	1.5 10^3
carbon	3 10^6	119
diamond like carbon	0 - 3 10^5	$\approx$ 18 - 20
PTFE (Teflon)	1 10^{-16}	18 - 20

5.4.2 Influence of the projected potential for different phase plates geometries on the expected phase shift

The results in figure 5.7 show that there are only significant influences on large spatial frequencies when potentials applied to the phase plate are varied. To enhance the influence

on small spatial frequencies the offset charge due to contaminations has to be eliminated. On the other hand it is noticeable that much higher potentials are necessary to overcome this offset charge and to induce a phase shift at higher spatial frequencies, then in the experiments performed in the Zeiss EFTEM 923 at the same acceleration voltage of 200 keV. To give an explanation to this effect simulations of the projected potential are done for the phase plate geometries used in experiments performed with the Zeiss EFTEM 923 and the Zeiss Libra 200 DMU, both at 200 keV acceleration voltage. For this simulation again the programs gmsh, getdp [39,40] and MatLab are used. Figure 5.9 a) - c) show cross sections in x-z direction through the 3D potential distributions for an applied potential of 3 V of the phase plate PP2 used in the Zeiss EFTEM 923 for the F-aktin experiments (cf. section 4.4), PP3 in the Zeiss Libra 200 DMU for the catalase crystal experiments (cf. section 5.3) and an optimized phase plate geometry usable for the Zeiss Libra 200 DMU. Figure 5.9 d) - f) show the projected potentials along z-direction with phase shift units π. Figure 5.9 g) shows this phase shift as a function of distance to the phase plate tip. The data refers to the direction indicated by the white dotted line in figure 5.9 f). PP2 in figure 5.9 d) has a relative wide electrode: tip width = 1.3 µm, central electrode width = 0.5 µm. The electrode inside PP3 in figure 5.9 e) is a significantly reduced compared to PP2: tip width = 1.0 µm, central electrode width = 0.14 µm. This reduction of the electrode width has also an effect on the range of influence of the projected potential. In figure 5.9 e) the potential distribution is very localized and reaches out only to a distance of 0.1 µm for a phase shift above $\pi/2$. In figure 5.9 d) the projected potential is more delocalised and reaches out to a distance of 0.3 µm for a phase shift above $\pi/2$. For an idealized zero order beam with a delta shaped peak the geometry in figure 5.9 e) with a very localized field would be ideal. Though under experimental conditions the zero order beam in the Zeiss Libra 200 DMU is not delta peak shaped but has a Gaussian distribution with an estimated "full width at tenth maximum" (FWTM) of 750 nm [22]. At the same time the potential distribution is four times smaller then in figure 5.9 a) for the experiments carried out with the Zeiss EFTEM 923. Due to this discrepancy in the size of zero order beam and the extension of the projected potential distribution, the zero order beam **is no longer** on the steep gradient of the projected potential but on the broad and flat field. This means that a relative phase shift of $\pi/2$ **can not** be produced. To overcome this problem the electrode geometry for the Zeiss Libra 200 DMU has to be changed for future experiments towards thicker electrodes along z-directions (direction of the incident electrons). By enlarging the height instead of the width an increased single sideband contrast is also avoided. However the projected potential distribution in the x-y plane is enlarged, as can be seen in figure 5.9 f). Here the projected potential distribution reaches out up to 0.6 µm for a phase shift above $\pi/2$. With this geometry a relative phase

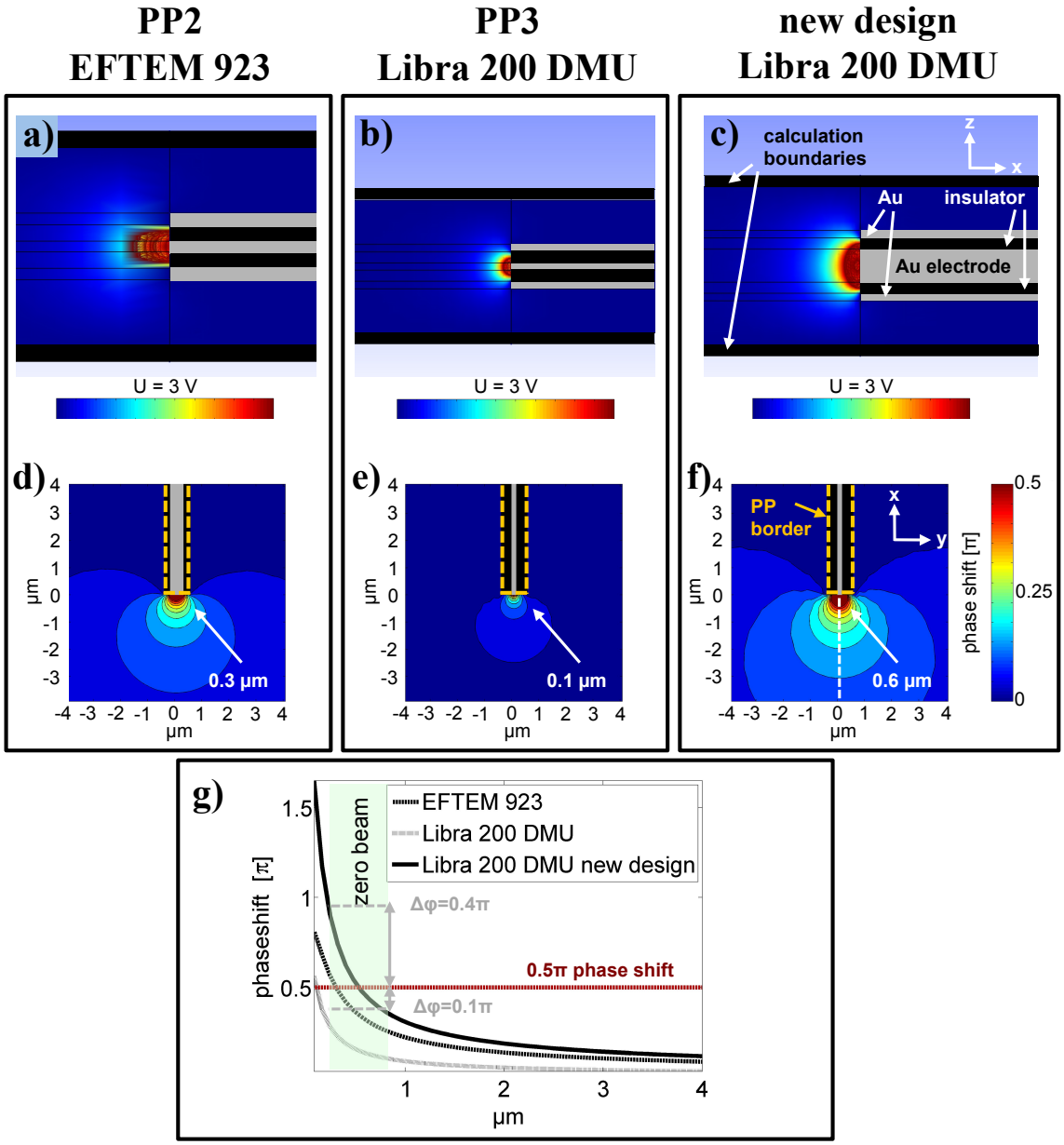

Figure 5.9: a) - c) cross sections in x-z direction through the 3D potential distribution for an applied potential of 3 V. d) - f) projected potentials with phase shift units π. All for Zach phase plates used in Zeiss EFTEM 923, Zeiss Libra 200 DMU and an ideal new design for the Zeiss Libra 200 DMU. g) phase shift as a function of distance to the phase plate tip, as indicated by the white doted line in f).

shift of $\pi/2$ for the zero order beam at a distance of 500 nm from the phase plate tip can be achieved, also visible in figure 5.9 g). As discussed in [22], due to the Gaussian shape of the zero order beam the majority of the electrons pass near the center, while only a fraction pass at the edge of the disk. Due to this the strongest phase shift variances of $\Delta\varphi = 0.4\pi$ for the zero order beam boarder facing the the phase plate tip and $\Delta\varphi = 0.1\pi$ for the boarder averting the tip should not influence the resulting phase contrast.

5.5 Conclusion

The appearance of very strong charging effects for Zach phase plates application with a DMU are shown and ways to significantly reduce them by coating the phase plate with amorphous carbon are presented. Coating with diamond like carbon should decrease the charging effect even more, due to its low surface energies reaching the values of PTFE. Its electrical conductivity depends on the mixture ratio of the sp^2 - graphen like and sp^3 - diamond like hybridization areas. Other materials with similar probabilities would also be usable. Furthermore the additional implementation of an anti contaminator in the DMU would also decrease the formation of charging contaminations during the phase plate use. The application of a charge reduced electrostatic Zach phase plate with a DMU show that the reduction of the electrode width and height, with regard to the Zach phase plate used in a conventional electron microscope, leads to an excessive decreasing gradient of the electrostatic potential distribution. The zero order beam is therefore not any more localized on the steep gradient area of the potential distribution but in the flat outer region. Thus the production of a relative phase shift of $\pi/2$ is no longer possible for the so far fabricated and tested phase plates. To avoid a broadening of the phase plate geometry and with this an increase in single sideband contrast, the phase plate electrode has to be enlarged in height but not in width. This leads to an enhanced range of influence of the **projected** potential. Thus the zero order beam can be positioned again on the step gradient of the projected potential and a relative phase shift of $\pi/2$ can be induced.
All this experimental results illustrate, that fundamental problems with charging and obstruction remain, as long as any object is placed in the diffraction plane. Therefore complementary new designs of obstruction free phase plates are needed.

6 Obstruction free phase contrast with the anamorphic phase plate

In this chapter the principle of an obstruction free electrostatic anamorphic phase plate is discussed. Its operating mode as well as necessary electron optical devices are explained. The influence of the aperture opening aspect ratio on image contrast is discussed as well as the influence on image contrast due to lateral mismatch of the phase plate with regard to the diffraction pattern. Furthermore a design evolution from the Zach phase plate to the anamorphic phase plate is presented, which includes the design of a double-Zach phase plate.

6.1 Design and operating mode of an anamorphic phase plate

The experiments with the Zach phase plate (ZPP) show that a phase contrast imaging with this type of phase plate is possible, even with invertible contrast when operated in a conventional microscope without DMU. Remaining problems are image artefacts due to single sideband contrast and charging effects. In contrast to this problems the highly inhomogeneous potential distribution produced by the ZPP has the great advantage of providing a **soft cut-on** range for spatial frequencies allocated at the steep gradient of the potential distribution. This avoids edge artefacts, which e.g. occur when using film phase plates or electrostatic Boersch phase plates. An ideal electrostatic phase plate would therefore provide the same inhomogeneous potential distribution but at the same time being free from any mechanical parts obstructing the beam path. As mentioned in chapter 1.3, Schröder et al. proposed an matter free electrostatic phase plate with anamorphic character [23]. Like the Zach phase plate, the anamorphic phase plate (APP) consists of a five layered structure. The central layer contains the gold electrodes for the induction of the electrostatic potential. They are surrounded from top an bottom by two insulating layers consisting of $Si_{3+X}N_{4-X}$ and HfO_2. Finally they are surrounded by two shielding gold layers. As described in chapter 5.4.1 the hole phase plate and carrier system should additionally be coated with a thin layer of amorphous carbon (a-C coating) or if

possible with diamond like carbon for charge reduction. Figure 6.1 shows the assembly of this five layered structure, the arrangement of the four electrodes in the central layer for two different operating modes and a SEM image of a first prototype produced by K. Schultheiss at KIT. The electrodes in the central layer are arranged in a rectangle array, with interruptions between each other and a slit like aperture opening in the center of the rectangle.

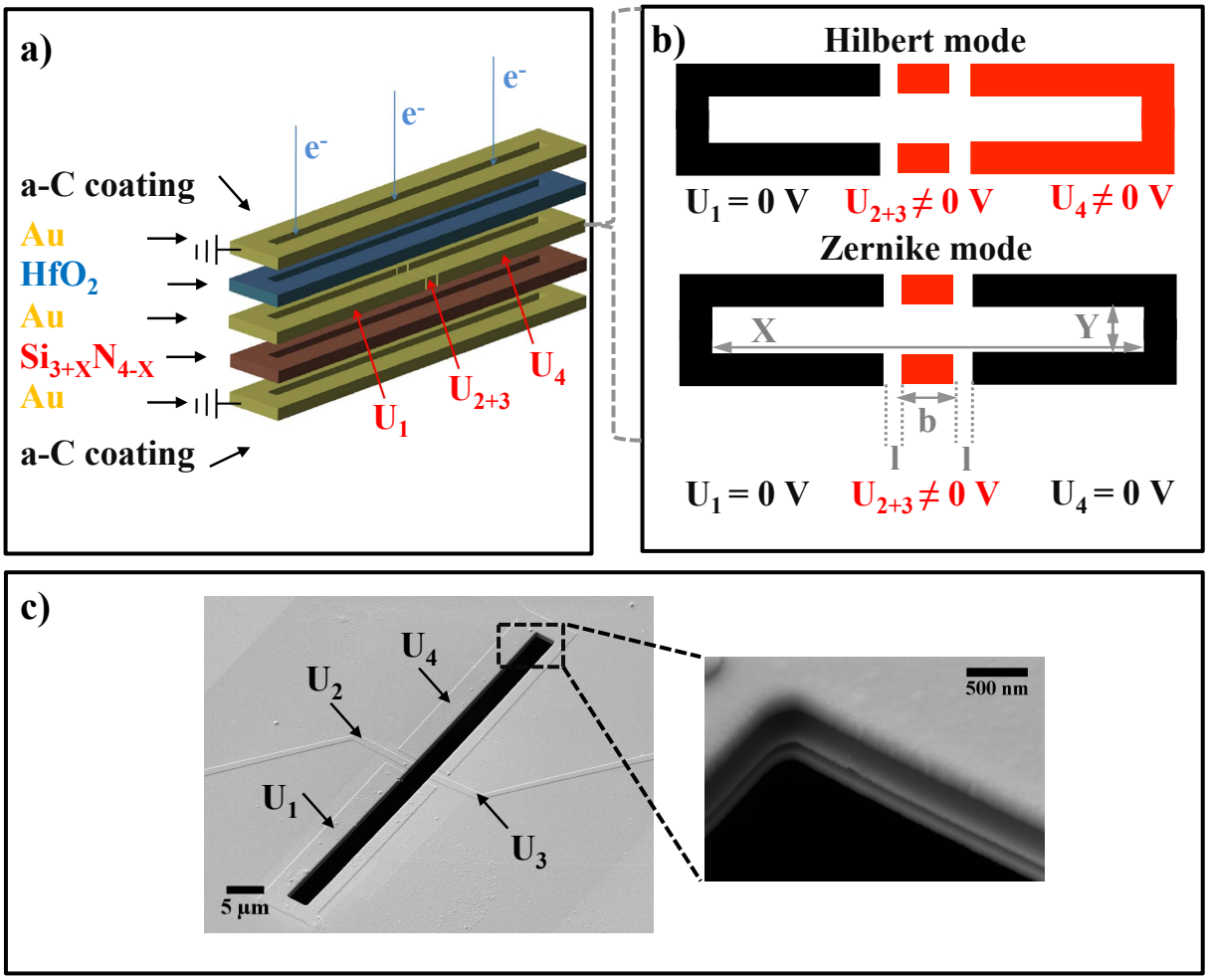

Figure 6.1: Figure a) five layered structure of an anamorphic phase plate (APP). Figure b) central electrode in Hilbert and Zernike mode. The four electrodes are named U_1, U_2, U_3, U_4. The ones with applied voltage are marked in red. Figure c) SEM image of a first prototype APP. The zoomed image shows the five layered structure.Images in c) acquired by K. Schultheiss, KIT [38].

All electrons in the diffraction plane have to pass through this aperture. Therefore the electron optics need also to provide this anamorphic beam shape. Thus for the usability of the APP an electron optical devise need to be implemented into the electron microscope that compresses the diffraction pattern along the spatial frequencies q_y and at the same time keeps or enlarges its extension along q_x. An electron optical lens system suitable for

this purpose contains quadrupole optics with similar arrangement as for the realisation of a $C_S - C_C$ corrector [64, 65] and is shown in figure 6.2.

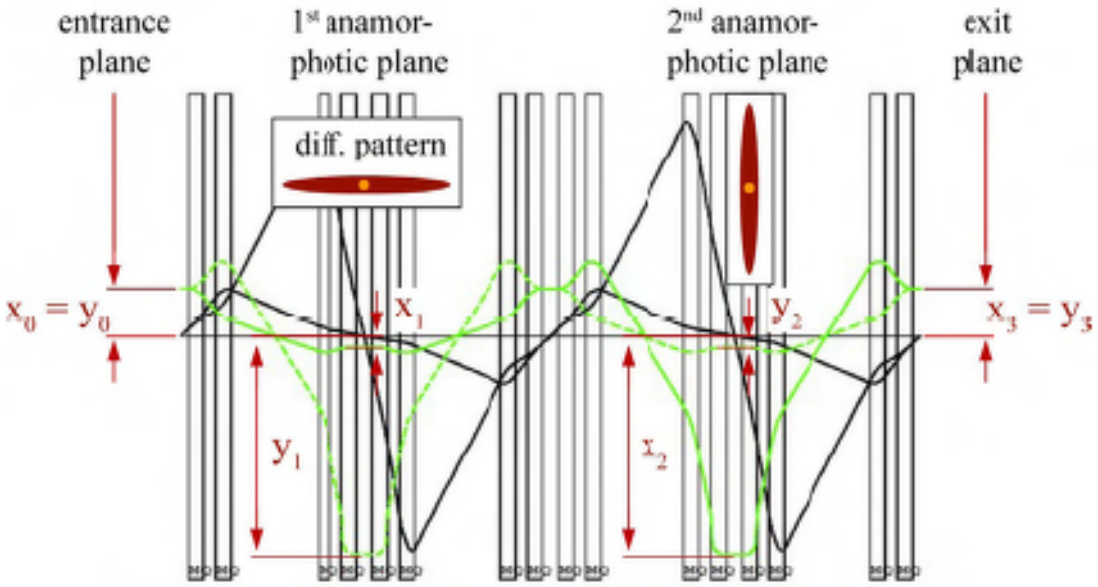

Figure 6.2: Ray path through a modified aberration corrector suitable for anamorphic phase plates. Image taken from [66]. The assembly of the 16 quadrupole lenses produce two anamorphic diffraction planes, oriented perpendicular to each other. The distance to the optical axes for the two main axes of the elliptical ray path are marked with green lines (solid for x-direction, dotted for y-direction). State of the art correctors can provide an anamorphic aspect ratio of 1:100.

As described in chapter 1.3 the APP can be operated in two ways, depending on the applied potential arrangement to the four central electrodes. Hilbert type phase contrast can be produced by applying a potential to the both middle electrodes and one of the side electrodes, keeping the remaining electrode at ground potential. This type of contrast is not discussed in detail, as it is not in relation to the contrast provided by the ZPP, which is the Zernike phase contrast. This Zernike type phase contrast can be produced with the APP by applying a potential to both middle electrodes and keeping both side electrodes at ground potential. However two crossed anamorphic phase plates in two different anamorphic diffraction planes are necessary for Zernike phase contrast. The corresponding electrode configuration is shown in figure 6.1 b).

6.2 Evolution from the Zach design to the anamorphic design

As described in section 6.1 the electrodes configuration of the APP should provide a highly anisotropic electrostatic potential in the central narrow slit aperture, with the same soft cut-on frequency as the ZPP. In the case of the APP the electrostatic potential shows a steep gradient in the gap region between the middle electrodes and the two electrodes positioned at the left and right side of the rectangle aperture. The gradient slop depends on the width of the gap between the electrodes.
For the Zernike mode its shape is comparable with the electrostatic potential distribution of the Zach phase plate. However the potential distribution of the APP has a constant potential between its two middle electrodes, and a steep gradient to the gap sides. The ZPP shows a steep gradient also in the direction parallel to its bar. The potential distribution of the APP is more favourable, as it ensures a constant phase shift independent of the distance of the zero order beam in parallel direction to the middle electrodes. Thus an even better agreement in the potential distribution arises for a comparison with a "double-Zach" phase plate (dZPP) consisting of two opposite arranged bars. The 3D potential distributions for all three phase plates can be seen in figure 6.3 . The calculation of the potential distributions is carried out using the programs gmsh and getdp [39, 40]. For the model of the APP the aperture opening is designed with an edge length ratio of 100:1. This is also called anamorphic ratio. On the basis of such 3D potential distributions, the resulting phase shift perpendicular to the middle electrode of the APP and perpendicular to the ZPP and dZPP tip are calculated. Figure 6.3 shows this induced phase shift for the APP and dZPP models and an assumed resolution of 1Å.
Due to the good agreement of the resulting phase shift as function of the perpendicular distance to the electrode between the APP and the dZPP, the latter model can be used for first tests in an electron microscope without the necessary anamorphic electron optics. Furthermore it is also usable with anamorphic electron optics and simplifies the beam alignment process due to its much wider aperture opening. The alignment procedure might be difficult for the very narrow aperture slit of the APP. Due to this the dZPP can be used for Zernike phase contrast in microscopes with or without anamorphic electron optics.

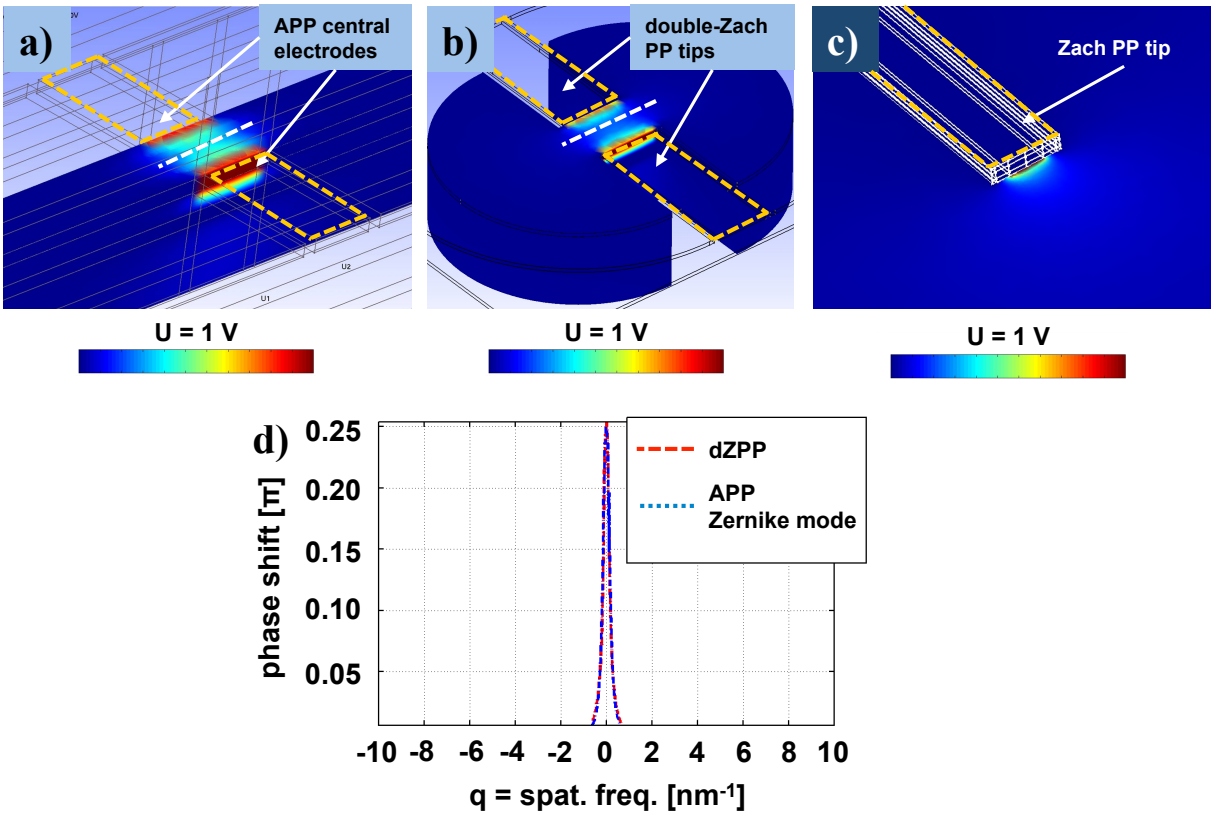

Figure 6.3: 3D potential distributions for a) anamorphic phase plate (APP) in Zernike mode, b) the double Zach phase plate (dZPP) and c) the Zach phase plate (ZPP). Figure d) shows the induced phase shift along the effective slit length (marked with dotted white line in a) and b)) of the APP and dZPP for an assumed resolution of 1Å at an anamorphic ratio of 100:1.

6.3 Simulations of in focus phase contrast for different anamorphic aspect ratios

Electron optics for aberration correctors provide an aspect ratio of 1:10 between the two main axes of the elliptical ray path in their anamorphic diffraction planes suitable for APPs. However as proposed in [67] this aspect ratio has to be increased at least to a ratio of 1:30. According to information of the manufacturer of aberration correctors CEOS, in the meantime aspects ration up to 1:100 are possible for these devices [68]. To detain an idea of the contrast generated by anamorphic phase plates in Zernike mode with different aspect ratios of their aperture opening, images where simulated for aspect ratios of 50:1, 75:1 and 100:1. Furthermore the influence on the contrast for a lateral shift of the elliptical electron beam with regard to the phase plate aperture is investigated. For this purpose the 3D potential distributions are calculated using gmsh and getdp, for phase plate geometries given in table 6.1.

Table 6.1: Dimensions of the central electrode of anamorphic phase plates with different aperture aspect ratios for the calculation of 3D potential distributions. The definition for the abbreviations are taken from figure 6.1 c).

aperture aspect ratio	50:1	75:1	100:1
X (µm)	50,0	75,0	100,0
Y (µm)	1,0	1,0	1,0
b (µm)	1,0	1,0	1,0
l (µm)	0,2	0,2	0,2

This 3D potential distributions are then used to calculate the projected potential along the electron ray path in z-direction and the resulting phase shift regarding equation 2.2. Simulations of the influence of these resulting phase shifts patterns are subsequent performed for the case of two crossed APPs in Zernike mode. Calculation of the projected potential as well as phase contrast image simulation are done by using MatLab, assuming an acceleration voltage of 200 keV, spherical aberration $C_S = 0$ nm, focal length $f = 2.7$ mm, defocus $\Delta z = 0$ nm and a pixel size of $ps = 0.2$ nm. As sample object a siemens star is used. This object provides the highest possible amount of different object sizes united in one image and with this also the highest amount of different spatial frequencies. Thus influences on spatial frequencies of the object by the phase shifting potential are best observed with this test object. Figure 6.4 shows the simulations for the APPs aperture opening with aspect ratios of 50:1, 75:1, 100:1 and a lateral misalignment of the zero order beam with regard to the middle APP electrodes of 0.0, 1.2 and 2.4 µm. With increasing aspect ratio of the aperture opening the frequencies range with high contrast transfer is enlarged. This is visible by the smaller radius of the central siemens star region with lower contrast. Furthermore a lateral shift between zero order beam and electrode shows a decreased influence on contrast reduction for increasing aspect ratio of the aperture opening. Both properties show that an aperture opening with maximal possible aspect ratio is preferable for the use of an APP with anamorphic electron optics.

As the object contrast for the application of an APP depends strongly on the position of the phase plate with regard to the diffraction pattern, this effect allows optimal alignment of the phase plate in transmission electron microscopes. To give an example on how this contrast change would affect a biological sample, simulations with an aperture aspect ratio of 100:1 where also performed using Myosin 2 as protein model input for the software package YamS [69, 70]. The simulations where done assuming an acceleration voltage of 200 keV, spherical aberration $C_S = 0$ nm, focal length $f = 2.7$ mm, defocus $\Delta z = 0$ nm and a Nyquist frequency $f_{Ny} = 0.2$ nm^{-1}. Image 6.5 shows the impact on the object contrast for lateral misalignments of the zero order beam with regard to the middle APP electrodes of 0.0, 1.2 and 2.4 µm. As expected the object contrast is reduced for an

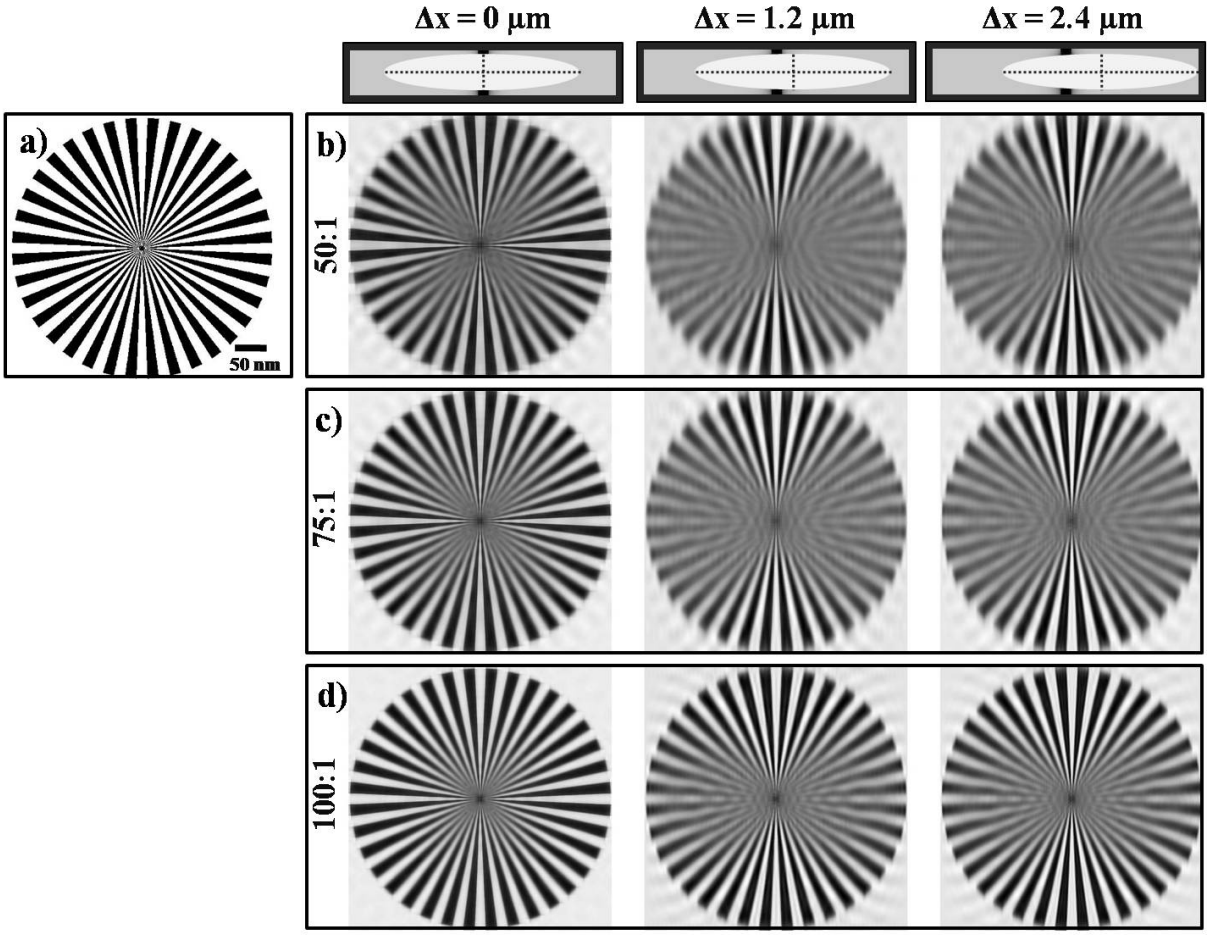

Figure 6.4: Image simulation for APP aperture opening with aspect ratios of b) 50:1, c) 75:1, d) 100:1 and a lateral misalignment of the zero order beam with regard to the middle APP electrodes of 0.0, 1.2 and 2.4 µm. Image a) shows the original siemens star. Used parameters are: acceleration voltage U = 200 keV, spherical aberration C_S = 0 nm, defocus Δz = 0 nm and a pixel size of ps = 0.2 nm. Best contrast transfer, even for lateral misalignment is achieved for an aperture aspect ratio of 100:1.

increasing lateral mismatch of the zero order beam to the middle electrodes, visible also in the corresponding line scan in figure 6.5 d).

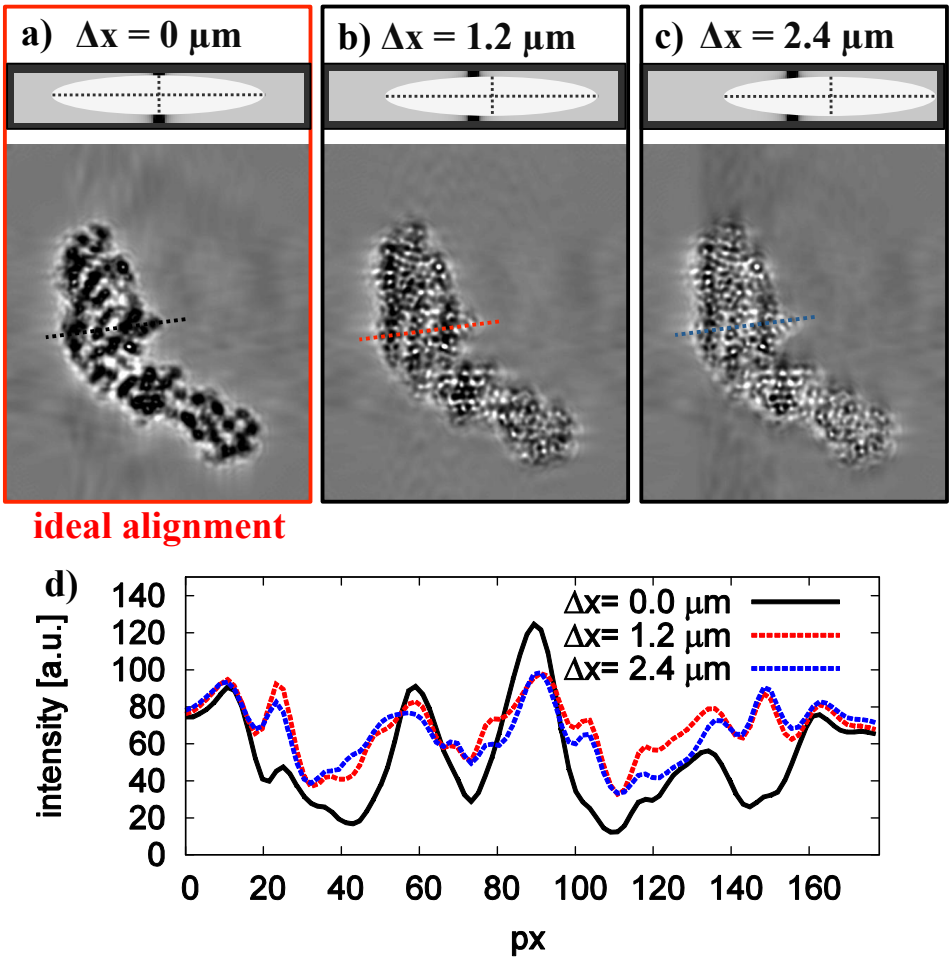

Figure 6.5: Influence of misalignment between zero order beam and middle APP electrodes. Object contrast is reduced between a) perfect aligned beam $\Delta x = 0.0$ µm, b) lateral shift of $\Delta x = 1.2$ µm and c) lateral shift of $\Delta x = 2.4$ µm. The decrease in image intensity is visible in d) as line scan. The region for the line scan is indicated by a red dotted line in b). This influence on the object contrast can be used as indicator for the phase plate alignment.

6.4 Conclusions

In this chapter the idea of an anamorphic phase plate (APP) is presented. Compared to other types of phase plates, it has the advantage of providing an obstruction free design, allowing all electrons to pass the phase plate without loss of information. By this no obstruction of frequencies or appearance of single sideband contrast occurs, which is not the case for the electrostatic Zach or Boersch phase plate. Furthermore there is no coherence loss as for film phase plates. This APP can be used in Hilbert or Zernike imaging mode. In both cases it works with a highly inhomogeneous electrostatic potential. This potential still provides a "soft cut-on" frequency range between the areas with relative phase shift of $\pi/2$ to each other, which avoids edge artefact. The APP has to be used within an anamorphic diffraction plane provided by corresponding electron optics with similar assembly as $C_S - C_C$ correctors. It is shown by image simulations for Zernike mode, that a highest possible aspect ratio of the APP aperture opening and the elliptical electron beam shape shows the best results for phase contrast transfer. Even contrast reduction due to lateral displacements of the elliptical electron beam is reduced by a maximized aspect ratio for the two main axes of the elliptical beam. State of the art $C_S - C_C$ correctors allow an aspect ratio of 100:1. Furthermore the obvious contrast dependency on a lateral mismatch between phase plate and elliptical diffraction pattern can be used for the phase plate alignment. A double Zach phase plate (dZPP) consisting of two parallel arranged Zach rods facing each other, shows a very similar electrostatic potential distribution as the APP in Zernike mode, with the same soft cut-on behaviour in the steep gradient area. As a result of this good agreement the dZPP should in future be used for first preliminary experiments in a microscope without anamorphic electron optics and also for testing the alignment procedure in an anamorphic diffraction plane, which should be simplified by the fact, that its aperture opening is wider than that of an original anamorphic phase plate. It should be noted, that it might also be advantageous to use this "open aperture" design even for an anamorphic optics in case of a dZPP -like system. Only the Hilbert - like phase plate needs the narrow, horseshoe like design, which ma cause obstruction problems during alignment.

7 Discussion and outlook

7.1 Current achievements in phase plate TEM

The application of TEM on samples consisting of light atoms - so called weak phase objects such as polymers or frozen hydrated biological specimens - has some essential limits regarding the amount of information that can be extracted from an image. Firstly, most samples are very beam sensitive and suffer from radiation damage. This requires the use of low electron dose which leads to a poor signal to noise ratio (SNR). Secondly the samples and the surrounding material, which is mostly amorphous ice, consist of elements with very similar low atomic numbers, which leads also to a low SNR. The sample information is mainly contained in their phase contrast.

Worldwide there are currently six groups doing research on the development on film or electrostatic phase plates for the contrast improvement in TEM. Nagayama et al. and Danev et al. could show the first realisation and application of Zernike and Hilbert film phase plates [29] and also further applications on biological systems [71] and on single particle analysis [72]. Application of Zernike film phase plates on single particle analysis and tomography of frozen hydrated samples was also demonstrated by Murata et al. [73]. The first realization and application of electrostatic Boersch phase plates was reported by Majorovits et al. [17]. Its application in a transmission electron microscope with a DMU was currently reported by Walter et al. [74]. An other type of phase plates exploiting the single sideband contrast was reported by Bujisse et al. [36]. Also a phase plate using a focused continuous-wave laser was proposed by Müller et al. [75]. From all these phase plates the Zernike film phase plate was the only one that showed reasonable results on the application of frozen-hydrated biological samples. But the film phase plate has the drawback of providing only a constant phase shift for a positive phase contrast image. The extend of the phase shift and therefore the image contrast improvement thereby depends on the acceleration voltage of the microscope and the corresponding film thickness. Tunable phase contrast, allowing the acquisition of images with **positive and / or negative** phase contrast is only possible by applying variable electrostatic fields. However this had not been reported until now, in work presented here, for any electrostatic phase plate applied for in-focus imaging of frozen-hydrated biological samples. The work

presented here demonstrates for the first time the in-focus image acquisition for frozen-hydrated biological samples with tunable, with the meaning of positive and negative phase contrast by the application of an electrostatic Zach phase plate.

7.2 Zach phase plate imaging with tunable phase contrast of frozen hydrated samples with conventional electron optics

In this work it could be shown, that in-focus phase contrast imaging with an electrostatic Zach phase plate is possible. Furthermore a contrast inversion can be induced, whereby the amount and the sign of phase shift is variable. This enables for the first time in-focus image acquisition of weak phase objects with tunable, increased contrast and less resolution loss then by applying the standard defocusing technique for contrast improvement. In comparison to film phase plates, the electrostatic Zach phase plate has the advantage of providing the mentioned tunable phase shift and higher resolution, as it avoids coherence loss due to additional scattering events in the film material. Compared to the electrostatic Boersch phase plate, the Zach phase plate has the advantage of avoiding the obstruction of a wide spatial frequency band by mechanical parts. Information of spatial frequencies blocked from one side in the diffraction plane by the Zach phase plate rod can be in principle be reconstructed due to Fiedel symmetry.

Simulations of the 3D potential distribution of the Zach phase plate showed that the potential has a very steep gradient next to the phase plate tip, followed by an almost homogeneous potential distribution with increased distance to the tip. The zero order beam is positioned next to the tip on the inhomogeneous gradient of the potential distribution. This showed no negative influences on in-focus phase contrast imaging. The steep potential gradient at the tip even showed the benefit of providing a "soft cut-on frequency". This therm describes the gradual change in the amount of relative phase shift between the zero order beam, being phase shifted by an amount of $\pi/2$, and spatial frequencies of scattered electrons. Edge artefacts due to sharp potential boarders, as appearing by the use of film phase plates, are avoided.
In addition it has been shown, that for an optimal use of the Zach phase plate a condenser aperture needs to be used that is small enough in diameter to provide sufficient spatial coherence for the zero order beam in the diffraction plane, where the phase plate is mounted. This limits the maximal sample size that can be used for Zach phase contrast imaging. Switching between different nominal magnification and condenser apertures during a microscopy session results in a partial obstruction of the zero order beam at low

nominal magnifications combined with a large aperture, due to the low spatial coherence and with this spreading of the zero order beam.

A disadvantages of the Zach phase plate, as for all other know electrostatic phase plates, is the production of single sideband (ssb) contrast due to an one-sided obstruction of Friedel symmetric spatial frequencies in the diffraction plane by mechanical parts. For the Zach phase plate the appearance of ssb contrast depends on the orientation of the object with respect to the phase plate rod. It could be shown that the influence of ssb contrast can be reduced by minimizing the dimensions of the Zach phase plate rod. Technical limitations allowed a reduction of the tip width down to 1 µm.

The life time of the Zach phase plate used in an electron microscope with conventional electron optic could be significantly increased by adapting a heating system to the phase plate. Heating the phase plate for approximately 12 hours at 60 °C removed contaminations and charging effects that appeared after electron exposure of the phase plate during its application. This heating proses can be repeated multiples times. It was shown however, that heating system and phase plate can not be used at the same time. Heating causes a reduction of the breakdown voltage of the isolating layers inside the phase plate, leading to a reduced maximally applicable phase plate potential.

Images can be corrected for ssb contrast by multiplying them in Fourier space with the inverse of their ssb affected contrast transfer function (CTF_{ssb}). The application of this correction procedure showed only very unsatisfying results. Reasons where a low SNR in images of frozen-hydrated samples, due to their dose sensitivity and remaining edge artefacts in the corrected images. The low SNR avoids an accurate determination of the phase plate boarders in the corresponding Power Spectra for the necessary masking procedure. Smoothing the mask with a Gaussian filter did not avoid the edge artefacts. Here an enhanced algorithm for the phase plate tip tracking in the Power Spectra images is necessary. Such an algorithm can also be used for an automated positioning control of the phase plate during its application. This would significantly reduce radiation damage on the sample due to shorter exposure times for phase plate alignment.

An interesting possibility results from the ability to apply different phase shifts to the zero order beam with the Zach phase plate: the exit wave reconstruction described in Gamm et al. [76] can theoretically be applied to Zach phase contrast images. This means that the whole phase information as well as amplitude information can be reconstructed, which is not provided by conventional single images in TEM. This reconstruction procedure is applicable for arbitrary object exit wave functions and also for non-linear image formation. Three images with different relative phase shifts $\phi_{PP} = -\pi/2,\ 0,\ +\pi/2$ between

the unscattered zero order beam and the scattered electrons are required. By subtracting the images from each other, the complex image wave function can be calculated. A subsequent CTF correction enables the calculation of the exit wave function. Further essential requirements for the successful application of this reconstruction technique are

- a highest possible contrast difference (= phase shift difference) between the three images for maximal information recovery.
- an optimal alignment of the three images before the subtraction procedure
- an optimal parameter evaluation of the phase contrast transfer function ($pCTF_{PP}$), including spherical aberration C_S, defocus Δz and phase shift ϕ_{PP}.
- a sufficiently high SNR in all three images
- an image area containing only vacuum as a reference for scaling the amplitude of the unscattered wave to the value one.

Especially the last two points make the successful application of the reconstruction procedure very difficult for phase contras images of frozen-hydrated samples. Acquired images showed mostly too low SNR. Therefore an optimal alignment using cross correlation was not applicable. Manual alignment could also not optimally be applied. Images of frozen-hydrated samples usually do not include vacuum regions, necessary for scaling. However, assuming an amplitude contrast of less then 10 % for thin ice layer without sample [1], such an image area could be used for scaling the amplitude of the unscattered wave to one.

7.3 Zach phase plate imaging with a diffraction magnification unit

The adaptation of the Zach phase plate for an electron microscope with diffraction magnification unit (DMU) reduces the amount of ssb contrast in the recorded images. This results in an increased diffraction plane dimension, where less spatial frequencies are obstructed by the phase plate rod. The phase plate tip width has still its minimal width of 1 µm. Here the width of the central electrode was also reduced to 0.14 µm.
It was shown experimentally and in simulations, that the excessive reduction of the Zach phase plate dimensions, and in particular the central electrode width results in an insufficient extension of the spatial potential distribution at the phase plate tip. The gradient of the potential fall-off is much steeper for the same applied potential to the phase plate

then for a phase plate with a larger central electrode. Higher potential values have to be applied to the phase plate with minimized central electrode to achieve a lager lateral extension of its electrostatic potential distribution. This is hampered by the low breakdown voltage of the insulating layers inside the phase plate. Due to this, even after the nearest possible positioning of the phase plate, the zero order beam is not located anymore on the steep gradient region of the electrostatic potential distribution, but already on the flat homogeneous part. This avoids the formation of a relative phase shift between the zero order beam of unscattered electrons and the scattered electrons. To overcome this problem, the electrode has to be enlarged in it height. This enables the application of higher potentials to the phase plate and at the same time reduces the breakdown voltage of the insulating layer. With this the electrostatic potential distribution provides a sufficient large spatial extension of its steep gradient area next to the phase plate tip to induce a phase shift of $\pi/2$ to the Gaussian shaped zero order beam.

Contamination and subsequent charging effects of the Zach phase plate are significantly more distinctive in the electron microscope with DMU compared to the application in the electron microscope with conventional electron optics. This arises from the increased relative dimension ratio between the diffraction plane and the phase plate tip inside the DMU, hence resulting in a better visibility of these effects.

A reason for these charging effects could be the strong adsorption of hydrocarbons to the gold surface of the phase plate due to its high surface energy. These charging effects cannot be eliminated by only heating the phase plate after its installation into the DMU. Previous argon plasma cleaning also does not remove all contaminations. However coating the phase plate with amorphous carbon decreases the charging effect significantly. Additional heating of the phase plate after an application session and electron exposure removed all new arising charging effects.

It is proposed that coating the phase plate with diamond like carbon instead of conventional amorphous carbon should reduced contamination effect even better. This is due to the low surface energy of diamond like carbon, which is comparable with the one of PTFE (Teflon), resulting in low adhesion of hydrocarbons on the surface. The electrical conductivity depends on the mixture ratio of sp^2 - graphen like and sp^3 - diamond like hybridization areas. It should be still high enough to discharge arising charge accumulations due to ionization of hydrocarbons by electron exposure. Furthermore the installation of an anti-contaminator in the DMU should additionally reduce the contamination of the phase plate during its application.

7.4 The obstruction free anamorphic phase plate

Here the idea of an obstruction free electrostatic phase plate is presented. The applicability, regarding its anisotropic and inhomogeneous potential, was for the first time experimentally verified. This phase plate is free of any mechanical parts that could block spatial frequencies in the diffraction plane where it is mounted. The benefits of this design are the absence of single sideband artefacts and less charging effects due to contamination produced by irradiation of mechanical parts with the zero order beam. For its application an electron microscope with anamorphic electron optic is needed. This means that it provides two diffraction planes, perpendicular to each other, where the ray path has an elliptical shape. Hence all electrons can pass through the elongated or anamorphic aperture opening of the anamorphic phase plate (APP) installed in this planes.
Simulations of the 3D electrostatic potential distribution of the APP where presented and compared to the ones of the Zach phase plate (ZPP) and a double Zach phase plate (dZPP). It was shown that the APP has a very similar beneficial inhomogeneous potential distribution in the near vicinity of its central electrodes as the ZPP. The anamorphic design will still provide a beneficial "soft cut-on" frequency between phase shifted electrons and not affected electrons. The 3D potential distribution of the dZPP and the APP showed even more similarities. Therefore the dZPP is usable for preliminary research with conventional electron optics. At the same time it can be used with anamorphic electron optics for a simplified alignment process due to its wider aperture opening compared to that of the APP.
Furthermore it could be shown that a typical maximal aspect ratio of 100:1 of the APP aperture opening and the main axis of the elliptical shaped electron beam leads to the best results in phase contrast transfer. Also contrast transfer reduction due to lateral displacement between the ray path an the APP is reduced.

7.5 Outlook on future phase plate projects

For a future successful application of the Zach phase plate in the Zeiss Libra 200 DMU, two main problems have to be overcome.
Firstly, the surface charging effects have to be eliminated. Here the manufacturing process of the phase plate has to be upgraded by an additional coating process with diamond like carbon and experimental tests have to be done. Furthermore the microscope should be equipped with an anti-contaminator in the DMU for further contamination reduction.
Secondly, the design of the central electrode has to be changed. A higher layer thickness will provide larger spatial extension of the inhomogeneous potential at the vicinity of the phase plate tip. At the same time this enables the application of higher potentials to

the phase plate and provides again the possibility of inducing a relative phase shift of $\pi/2$ between the zero order beam and the scattered electrons.
Currently the most promising prospects of success for the use of tunable electrostatic phase plates can be expected from the anamorphic phase plate. The studies presented in this work answered posed objections such as applicability of anisotropic and inhomogeneous electrostatic potentials or effects of "soft cut-on" frequency bands. All experiments with the Zach phase plate indicate, that the simulated potential of the anamorphic phase plate will be applicable to routine phase plate contrast improvement. Hence the manufacturing of an electron microscope with anamorphic electron optic would be very desirable.

Appendix A: Gmsh and GetDP

A.1 Gmsh: a three-dimensional finite element mesh generator with built-in pre- and post-processing facilities

The following description of the Gmsh software is cited from [77]:
"Gmsh is a 3D finite element grid generator with a build-in CAD engine and post-processor. Its design goal is to provide a fast, light and user-friendly meshing tool with parametric input and advanced visualization capabilities. Gmsh is built around four modules: geometry, mesh, solver and post-processing. The specification of any input to these modules is done either interactively using the graphical user interface or in ASCII text files using Gmsh's own scripting language."
An exemplary Gmsh data text file for the specification of a Zach phase plate is shown in the following:

```
//Zach_Kronos_3D_2012/Elektr_500nm_Steg_1mum_Hoehe_65nm/
//Pot_3V/Zach_Kronos_3D.geo
//3D model for Zach PP in Zeiss Libra 200 DMU.
Include "parameters_ZachKronos_3D.pro";
//*** Allg. Parameter ***
Geometry.Color.Points = Blue;
Geometry.Color.Lines = Black;
Mesh.Color.Points = {255,0,0};
// ***Parameters for size of mesh elements ***
// ****************************************
lc1= 0.1;       //0.04
Mesh.CharacteristicLengthFactor = 6.1;
//variable
//*** Parameters for phase plate dimensions***
//*** can be modified***
//****************************************
 // mum = 1e-6; //(for displaying in Micrometers)
 A1 = -0.25;    //left side electrode
 A2 = 0.25;             //right side electrode
 B1 = -0.195;   //left side insulator
 B2 = 0.195;    //right side insulator
 C1 = -0.055;   //left side ground electrode
 C2 = 0.055;    //right side ground electrode
 D1 = 43.5;         //left side length of electrode (pos. y-direction!)
 D2 = 43.5;         //right side length of electrode(pos. y-direction!)
```

```
E1 = -43.5;    //left side of upper box width
E2 = 43.5;        //right side of upper box width
F1 =-87;             //left side of ox height //(neg. y-direction!)
F2 = -87;            //right side of box height //(neg. y-direction!)
G1 = A1+B1+C1+E1; //left side of lower Box width
G2 = A2+B2+C2+E2; //right side of lower Box width
H = 1;         //overall thickness of ground
I = 1;         //overall thickness of border
//***Hoehen der Volumeschichten in Muekrometer***
h  = 0.065;    //Hoehe der zentralen Elektrode - variabel!!!
k1 = 0.1;      //Hoehe der Isolatorschicht Oben (HfO)
k2 = 0.1;      //Hoehe der Isolatorschicht Unten (SiN)
l1 = 0.07;     //Hoehe der Erdungsschicht Oben
l2 = 0.07;     //Hoehe der Erdungsschicht Unten
m1 = 0.4;      //Hoehe des Vakuums Zwischenraum Oben
m2 = 0.4;      //Hoehe des Vakuums Zwischenraum Unten
n1 = 0.1;      //Hoehe der Aussen Erdung Oben
n2 = 0.1;      //Hoehe der Aussen Erdung Unten
//***fuer transfinite mesh***
N =26;         //li,re auessere senkr. Seite des Loches
NN=13;         //li,re innere senkrechte Seite des Loches
O = 26;    //li,re untere waagrechte Seiten des Loches
OO = 13;       //li,re obere waagrechte Seiten des Loches
P = 3;         //Breite des Ground an der Spitze
Q = 18;        //Breite Boarder an der Spitze /Isolator
R = 6;         //Elektrode
//***Layer Anzahl fuer extrude***
Zc=10; //center layers , Elektrode
Z= 5;
Zz=10; //layers fuer Vakuum Zwischenraum
/****  END HEADER      *****

//***inner box border ***
Point (1) = {0, 0, 0, lc1};                    //CENTER
Point (2) = {A1, 0, 0, lc1};
Point (3) = {A1+B1, 0, 0, lc1};
Point (4) = {A1+B1+C1, 0, 0, lc1};
Point (5) = {A1+B1+C1, D1, 0, lc1};
Point (6) = {A1+B1+C1+E1, D1, 0, lc1};
Point (7) = {A1+B1+C1+E1, D1+F1, 0, lc1};
Point (8) = {0, D1+F1, 0, lc1};//lower symmetry center
Point (9) = {A2+B2+C2+E2, D2+F2, 0, lc1};
Point (10) = {A2+B2+C2+E2, D2, 0, lc1};
Point (11) = {A2+B2+C2, D2, 0, lc1};
Point (12) = {A2+B2+C2, 0, 0, lc1};
Point (13) = {A2+B2, 0, 0, lc1};
Point (14) = {A2, 0, 0, lc1};
// *** outer box border ***
Point (15) = {A1, D1, 0, lc1};
Point (16) = {A1, D1+H, 0, lc1};
Point (17) = {A1+B1, D1, 0, lc1};
Point (18) = {A1+B1, D1+H, 0, lc1};
Point (19) = {A1+B1+C1+E1-H, D1+H, 0, lc1};
Point (20) = {G1-H, D1+F1-H, 0, lc1};
Point (21) = {0, D1+F1-H, 0, lc1};//lower symmetry center
Point (22) = {G2+H, D2+F2-H, 0, lc1};
Point (23) = {A2+B2+C2+E2+H, D2+H, 0, lc1};
```

```
Point (24) = {A2+B2, D2+H, 0, lc1};
Point (25) = {A2+B2, D2, 0, lc1};
Point (26) = {A2, D2, 0, lc1};
Point (27) = {A2, D2+H, 0, lc1};
//*** closing box ***
Point (28) = {G1-H-I, D1+H+I, 0, lc1};
Point (29) = {G1-H-I, D1+F1-H-I, 0, lc1};
Point (30) = {G2+H+I, D2+F2-H-I, 0, lc1};
Point (31) = {G2+H+I, D2+H+I, 0, lc1};
// *** Lines ***
Line(1) = {1, 2}; Line(2) = {2, 3}; Line(3) = {3, 4};
Line(4) = {4, 5}; Line(5) = {5, 6}; Line(6) = {6, 7};
Line(7) = {7, 8}; Line(8) = {8, 9}; Line(9) = {9, 10};
Line(10) = {10, 11}; Line(11) = {11, 12}; Line(12) = {12, 13};
Line(13) = {13, 14}; Line(14) = {14, 1}; Line(15) = {2, 15};
Line(16) = {15, 16}; Line(17) = {16, 27}; Line(18) = {27, 26};
Line(19) = {26, 14}; Line(20) = {3, 17}; Line(21) = {17, 18};
Line(22) = {18, 19}; Line(23) = {19, 20}; Line(24) = {20, 21};
Line(25) = {21, 22}; Line(26) = {22, 23}; Line(27) = {23, 24};
Line(28) = {24, 25}; Line(29) = {25, 13}; Line(30) = {28, 29};
Line(31) = {29, 30}; Line(32) = {30, 31}; Line(33) = {31, 28};
//*** Plane Surfaces ***
//***Electrode***
Line Loop(37) = {14, 1, 15, 16, 17, 18, 19};Plane Surface(38) = {37};
//***Ground***
Line Loop(39) = {3, 4, 5, 6, 7, 8, 9, 10, 11, 12, -29, -28, -27, -26,
 -25, -24, -23, -22, -21, -20}; Plane Surface(40) = {39};
//***Border***
Line Loop(41) = {33, 30, 31, 32};
Line Loop(42) = {22, 23, 24, 25, 26, 27, 28, 29, 13, -19, -18, -17,
-16, -15, 2, 20, 21}; Plane Surface(43) = {41, 42};
//***Vacuum***
Line Loop(44) = {4, 5, 6, 7, 8, 9, 10, 11, 12, 13, 14, 1, 2, 3};
Plane Surface(45) = {44};
/*************************
***Center Part / Electrode***
*************************/
Extrude {0,0,h}{Surface{38};Layers{Zc};}//VElectrode(1)
Extrude {0,0,h}{Surface{40};Layers{Zc};}//VGround(2)
Extrude {0,0,h}{Surface{43};Layers{Zc};}//VBorder(3)
Extrude {0,0,h}{Surface{45};Layers{Zc};}//VVacuum(4)
//***physical surfaces***
PSElectrode=368; Physical Surface(PSElectrode)= {61, 65,
69, 86,85, 38, 73, 81, 77};
PSGround=369; Physical Surface(PSGround) = {111, 115, 187,
183, 179, 175, 171, 167, 163, 159, 155, 151, 147, 143,
139, 135, 131, 127, 123, 119, 40, 188};
PSBorder=370; Physical Surface(PSBorder) = {183, 234, 65,
69, 73, 77, 81, 258, 147, 151, 155, 159, 163, 167, 171,
175, 179, 210, 222, 218, 214, 291, 43};
PSVacuum=371; Physical Surface(PSVacuum)={107,234,61,57,
258, 143, 139, 135, 131, 127, 123, 119, 115,111,363,45};
//***physical volumes***
PVElectrode=372; Physical Volume(PVElectrode) = {1};
PVGround=373; Physical Volume(PVGround) = {2};
PVBoarder=374; Physical Volume(PVBoarder) = {3};
PVVacuum=375; Physical Volume(PVVacuum) = {4};
```

```
//***Transfinite Mesh Vacuum Center Part (4)***
Transfinite Line {6,9} = N; Transfinite Line {4,-11} = N Using Progression 1.2;
Transfinite Line {-7,8} = O; Transfinite Line {5,10} = O;
Transfinite Line {3,12} = P; Transfinite Line {2,13} = Q;
Transfinite Line {1,14} = R; Transfinite Volume {1} ={6,7,9,10,63,67,75,79};
/*********************************************
*Isolatorschicht unten und oben drueber
*********************************************/
//*** Isolator Oben***
Extrude {0,0,k1}{Surface{363};Layers{Z};}//VVacuumOben(5)
Line Loop(448) = {103, 192, -48, -47, 198, 94, 95,
96, 97, 98, 99, 100, 101, 102};
Line Loop(449) = {186, 187, 188, 189};
Plane Surface(450) = {449, 448};
Extrude {0,0,k1}{Surface{450};Layers{Z};}//VBorderOben(6)
Extrude {0,0,k1}{Surface{184};Layers{Z};}//VGroundOben(7)
//***physical surfaces***
PSVacuumIsoOben=645; Physical Surface(PSVacuumIsoOben) =
{398, 394, 446, 442, 438, 434, 430, 426, 422, 418, 414,
410, 406, 402, 447, 363};
PSBorderIsoOben=646; Physical Surface(PSBorderIsoOben) =
{493, 489, 541, 442, 438, 434, 430, 521, 517, 513, 509,
505, 501, 497, 542, 450, 473, 485, 481, 477};
PSGroundIsoOben=647; Physical Surface(PSGroundIsoOben) =
{489, 541, 446, 394, 398, 402, 406, 410, 414, 418, 422,
426, 521, 517, 513, 509, 505, 501, 497, 493, 644, 184};
//***physical volumes***
PVVacuumIsoOben=648;Physical Volume(PVVacuumIsoOben)={5};
PVBorderIsoOben=649;Physical Volume(PVBorderIsoOben)={6};
PVGroundIsoOben=650;Physical Volume(PVGroundIsoOben)={7};
// ***Isolator Unten***
Extrude{0,0,-k2}{Surface{45};Layers{Z};}//VVacuumUnten(8)
Line Loop(723) = {22, 23, 24, 25, 26, 27, 28, 29, 13,
14, 1, 2, 20, 21};
Plane Surface(724) = {41, 723};
Extrude{0,0,-k2}{Surface{724};Layers{Z};}//VBorderUnten(9)
Extrude{0,0,-k2}{Surface{40};Layers{Z};}//VGroundOben(10)
//***physical surfaces***
PSVacuumIsoUnten=919; Physical Surface(PSVacuumIsoUnten)=
{697, 693, 689, 685, 681, 677, 673, 669, 721, 717, 713,
709, 705, 701, 45, 722};
PSBorderIsoUnten=920; Physical Surface(PSBorderIsoUnten)=
{795, 799, 803, 807, 811, 815, 763, 767, 717, 713, 709,
705, 787, 791, 747, 759, 755, 751, 816, 724};
PSGroundIsoUnten=921; Physical Surface(PSGroundIsoUnten)=
{763, 767, 721, 669, 673, 677, 681, 685, 689, 693, 697,
701, 787, 791, 795, 799, 803, 807, 811, 815, 40, 918};
//***physical volumes***
PVVacuumIsoUnten=922;Physical Volume(PVVacuumIsoUnten)={8};
PVBorderIsoUnten=923;Physical Volume(PVBorderIsoUnten)={9};
PVGroundIsoUnten=924;Physical Volume(PVGroundIsoUnten)={10};
//***Transfinite Mesh ***
//***Vacuum Isolator Oben (5)***
Transfinite Line {87,90} = N; Transfinite Line {85,-92} = N Using Progression 1.2;
Transfinite Line {88,89} = O; Transfinite Line {86,91} = O;
Transfinite Line {84,93} = P; Transfinite Line {192,198} = Q;
Transfinite Line {48,47} = R; Transfinite Volume {5} ={67,71,75,79,159,155,151,147};
```

```
//***Vacuum Isolator Unten (8)***
Transfinite Line {654,657} = N; Transfinite Line {652,-659} = N Using Progression 1.2;
Transfinite Line {655,656} = O; Transfinite Line {653,658} = O;
Transfinite Line {665,660} = P; Transfinite Line {664,661} = Q;
Transfinite Line {663,662} = R; Transfinite Volume {8} ={259,255,251,247,8,9,10,11};
/*****************************
*Erdungsschichten oben und unten
*****************************/
// ***Erdungsschicht Oben***
// ***Vacuum****
Extrude {0,0,l1}{Surface{447};Layers{Z};}
//VVacuumErdOben(11)
PSVacuumErdOben=997;Physical Surface(PSVacuumErdOben)=
{995, 991, 987, 983, 979, 975, 971, 967, 963, 959,
955, 951, 947, 943, 996, 447};
PVVacuumErdOben=998;Physical Volume(PVVacuumErdOben)={11};
//***Erdung selbest**
Line Loop(999) = {452, 453, 454, 455};
Line Loop(1000) = {378, 379, 380, 381, 382, 383, 384,
385, 386, 387, 388, 389, 390, 377};
Plane Surface(1001) = {999, 1000};//SErdungOben
Extrude{0,0,l1}{Surface{1001};Layers{Z};}//VErdOben(12)
PSErdOben=1094; Physical Surface(PSErdOben) =
{1024, 1036, 1032, 1028, 967, 963, 959, 955, 951, 947, 943,
995, 991, 987, 983, 979, 975, 971, 1093, 1001};
PVErdOben=1095;Physical Volume(PVErdOben) = {12};
//***Erdungschicht Unten***
//***Vacuum***
Extrude{0,0,-l2}{Surface{722};Layers{Z};}
//VVacuumErdUnten(13)
PSVacuumErdUnten=1168; Physical Surface(PSVacuumErdUnten)=
{1166, 1162, 1158, 1154, 1150, 1146, 1142, 1138, 1134,
1130, 1126, 1122, 1118, 1114, 722, 1167};
PVVacuumErdUnten=1169;
Physical Volume(PVVacuumErdUnten)={13};
//***Erdung selbest***
Line Loop(1170) = {726, 727, 728, 729};
Line Loop(1171) = {653, 654, 655, 656, 657, 658, 659, 660,
661, 662, 663, 664, 665, 652};
Plane Surface(1172) = {1170, 1171}; //SErdungUnten
Extrude {0,0,-l2}{Surface{1172};Layers{Z};}
//VErdUnten(14)
PSErdUnten=1265; Physical Surface(PSErdUnten) =
{1118, 1114, 1166, 1162, 1158, 1154, 1150,1146,1142,1138,
1134, 1130, 1126, 1122, 1195, 1207, 1203,1199,1172,1264};
PVErdUnten=1266; Physical Volume(PVErdUnten) = {14};
//***Transfinite Mesh ***
//***Vakuum Erdung Oben (11)***
Transfinite Line {377,-384} = N Using Progression 1.2;
Transfinite Line {379,382} = N; Transfinite Line {388,387} = R;
Transfinite Line {380,381} = O; Transfinite Line {378,383} = O;
Transfinite Line {390,385} = P; Transfinite Line {389,386} = Q;
Transfinite Volume{11}={147,151,155,159,371,367,363,359};
//***Vakuum Erdnung Unten (13)***
Transfinite Line {1097,-1104} = N Using Progression 1.2;
Transfinite Line {1099,1102} = N; Transfinite Line {1108,1107} = R;
Transfinite Line {1100,1101} = O ; Transfinite Line {1098,1103} = O;
```

```
Transfinite Line {1110,1105} = P; Transfinite Line {1109,1106} = Q;
Transfinite Volume{13} = {435,431,427,423,259,255,251,247};
/*********************************
* Vakuum Zwischenraum Oben / Unten
*********************************/
//*** Vakuum Oben***
//***Vacuum***
Line(1267) = {351, 375};
Line Loop(1268) = {1267, -932, -931, -930, -929,-928, 927};
Plane Surface(1269) = {1268};
Extrude {0,0,m1}{Surface{1269};Layers{Zz};}
//VVakuumZRaumOben(15)
PSVacuumZRaumOben=1307;
Physical Surface(PSVacuumZRaumOben)=
{1281, 1285, 1289, 1293, 1297, 1301, 1305, 1306, 1269};
PVVacuumZRaumOben=1308;
Physical Volume(PVVacuumZRaumOben)={15};
//**Erdung***
Line Loop(1309) = {1003, 1004, 1005, 1006};
Plane Surface(1310) = {1309, 1268};
Extrude {0,0,m1}{Surface{1310};Layers{Zz};}
//VErdungZRaumOben(16)
PSErdZRaumOben=1368; Physical Surface(PSErdZRaumOben) =
{1326, 1338, 1334, 1330, 1305, 1281, 1285, 1289, 1293,
1297, 1301, 1367, 1310};
PVErdZRaumOben=1369;Physical Volume(PVErdZRaumOben)={16};
//*** Vakuum Unten***
//***Vacuum***
Line(1370) = {411, 435};
Line Loop(1371)={1370, -1103, -1102, -1101, -1100,
 -1099, -1098};
Plane Surface(1372) = {1371};
Extrude {0,0,-m2}{Surface{1372};Layers{Zz};}
//VVakuumZRaumUnten (17)
PSVacuumZRaumUnten=1410;
Physical Surface(PSVacuumZRaumUnten)= {1384, 1388,
1392, 1396, 1400, 1404, 1408, 1372, 1409};
PVVacuumZRaumUnten=1411;
Physical Volume(PVVacuumZRaumUnten)={17};
//**Erdung***
Line Loop(1412) = {1174, 1175, 1176, 1177};
Plane Surface(1413) = {1412, 1371};
Extrude {0,0,-m2}{Surface{1413};Layers{Zz};}
//VErdungZRaumUnten (18)
PSErdZRaumUnten=1471;
Physical Surface(PSErdZRaumUnten)={1429,1441,1437,1433,
1408, 1384, 1388, 1392, 1396, 1400, 1404, 1413, 1470};
PVErdZRaumUnten=1472;
Physical Volume(PVErdZRaumUnten) = {18};
//***Transfinite Mesh ***
//***Vakuum ZRaum Oben (15)***
Transfinite Line {928,931} = N; Transfinite Line {929,930} = O ;
Transfinite Line {927,932,1267} = O ;
Transfinite Volume {11}={359,363,367,371,475,479,483,487};
//***Vakuum ZRaum Unten (17)***
Transfinite Line {1379,1376} = N; Transfinite Line {1378,1377} = O ;
Transfinite Line {1380,1375,1374} = O ;
```

```
Transfinite Volume {17}= {519,515,511,507,431,427,423,419};
//***Aussen Erdung Oben / Unten***
//*** Erdung Oben ***
Line Loop(1473) = {1312, 1313, 1314, 1315};
Plane Surface(1474) = {1473};
Extrude {0,0,n1}{Surface{1474};Layers{2};}
//VAussenErdungOben(19)
PSAusErdOben=1497;
Physical Surface(PSAusErdOben) = {1483, 1495, 1491, 1487, 1496, 1474};
PVAusErdOben=1498;Physical Volume(PVAusErdOben)={19};
//*** Erdung Unten ***
Line Loop(1499) = {1416, 1417, 1418, 1415};
Plane Surface(1500) = {1499};
Extrude {0,0,-n2}{Surface{1500};Layers{2};}
//VAussenErdungUnten (20)
PSAusErdUnten=1523;
Physical Surface(PSAusErdUnten)={1521, 1517, 1513, 1509, 1522, 1500};
PVAusErdUnten=1524;Physical Volume(PVAusErdUnten)={20};
```

This is the additional data file parameters_ZachKronos_3D.pro:

```
//This is : parameters_ZachKronos_3D.pro
PSElectrode=368;                    //Zentraler Teil
PSGround=369;
PSBorder=370;
PSVacuum=371;
PVElectrode=372;
PVGround=373;
PVBoarder=374;
PVVacuum=375;
PSVacuumIsoOben=645;     //Isolator Oben
PSBorderIsoOben=646;
PSGroundIsoOben=647;
PVVacuumIsoOben=648;
PVBorderIsoOben=649;
PVGroundIsoOben=650;
PSVacuumIsoUnten=919;    //Isolator Unten
PSBorderIsoUnten=920;
PSGroundIsoUnten=921;
PVVacuumIsoUnten=922;
PVBorderIsoUnten=923;
PVGroundIsoUnten=924;
PSVacuumErdOben=997;     //ErdungOben
PSErdOben=1094;
PVVacuumErdOben=998;
PVErdOben=1095;
PSVacuumErdUnten=1168;   //Erdung Unten
PSErdUnten=1265;
PVVacuumErdUnten=1169;
PVErdUnten=1266;
PSVacuumZRaumOben=1307; //ZwischenRaum Oben
PSErdZRaumOben=1368;
PVVacuumZRaumOben=1308;
PVErdZRaumOben=1369;
PSVacuumZRaumUnten=1410;//ZwischenRaum Unten
PSErdZRaumUnten=1471;
PVVacuumZRaumUnten=1411;
```

```
PVErdZRaumUnten=1472;
PSAusErdOben=1497;              //Aussere Erdung Oben (*)
PVAusErdOben=1498;
PSAusErdUnten=1523;             //Aussere Erdung Unten
PVAusErdUnten=1524;
```

A.2 GetDP: a General environment for the treatment of Discrete Problems

The following description of the GetDP software is cited from [78]:
"GetDP is a general finite element solver using mixed elements to discretize de Rham-type complexes in one, two and three dimensions. The main feature of GetDP is the closeness between the input data defining discrete problems (written by the user in ASCII data files) and the symbolic mathematical expressions of these problems.
An assembly of computational tools (or objects) in GetDP leads to a problem definition structure, which is a transcription of the mathematical expression of the problem, and forms a text data file: the equations describing a phenomenon, written in a mathematical form adapted to a chosen numerical method, directly constitute data for GetDP.
The resolution of a discrete problem with GetDP requires the definition, in a text data file, of the GetDP objects listed (together with their dependencies) in the following figure and table."

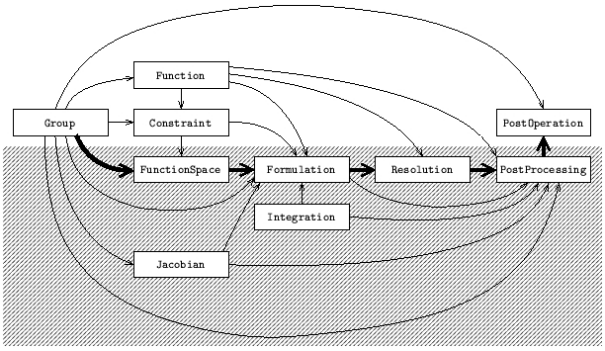

Figure A.1: GetDP objects together with their dependencies. Image and table taken from [78].

Group	-
Function	Group
Constraint	Group, Function, (Resolution)
FunctionSpace	Group, Constraint, (Formulation), (Resolution)
Jacobian	Group
Integration	-
Formulation	Group, Function, (Constraint), FunctionSpace, Jacobian, Integration
Resolution	Function, Formulation
PostProcessing	Group, Function, Jacobian, Integration, Formulation, Resolution
PostOperation	Group, PostProcessing

" The gathering of all these objects constitutes the problem definition structure, which is a copy of the formal mathematical formulation of the problem. Reading the first column of the table from top to bottom pictures the working philosophy and the linking of operations peculiar to GetDP, from group definition to results visualization. The decomposition highlighted in the figure points out the separation between the objects defining the method of resolution, which may be isolated in a "black box" (bottom) and those defining the data peculiar to a given problem (top).

The computational tools which are in the center of a problem definition structure are formulations (Formulation) and function spaces (FunctionSpace). Formulations define systems of equations that have to be built and solved, while function spaces contain all the quantities, i.e., functions, fields of vectors or co-vectors, known or not, involved in formulations.

Each object of a problem definition structure must be defined before being referred to by others. A linking which always respects this property is the following: it first contains the objects defining particular data of a problem, such as geometry, physical characteristics and boundary conditions (i.e., Group, Function and Constraint) followed by those defining a resolution method, such as unknowns, equations and related objects (i.e., Jacobian, Integration, FunctionSpace, Formulation, Resolution and PostProcessing). The processing cycle ends with the presentation of the results (i.e., lists of numbers in various formats), defined in PostOperation fields. This decomposition points out the possibility of building black boxes, containing objects of the second group, adapted to treatment of general classes of problems that share the same resolution methods."

Problems that GetDP is actually able to solve are:

"**Numerical methods:** finite element method, boundary element method (experimental, undocumented), volume integral methods (experimental, undocumented)

Geometrical models: one-dimensional models (1D), two-dimensional models (2D) plane

and axisymmetric, three-dimensional models (3D)

Time states: static states, sinusoidal and harmonic states, transient states, eigenvalue problems "

An exemplary GetDP data text file for the resolution of the 3D potential distribution of the Zach phase plate is shown in the following:

```
//Zach_Kronos_3D_2012/Elektr_500nm_Steg_1mum_Hoehe_65nm/
//Pot_3V/Zach_Kronos_3D.pro

Include "parameters_ZachKronos_3D.pro";

Group {
// PS denotes Surfaces, PV denotes Volumes.
// # can be used instead of Region[]

// ***SURFACES***
//Zentraler Teil
  PSElectrode=#PSElectrode;
  PSGround=#PSGround;
  PSBorder=#PSBorder;
  PSVacuum=#PSVacuum;
//Isolator Oben
  PSVacuumIsoOben=#PSVacuumIsoOben;
  PSBorderIsoOben=#PSBorderIsoOben;
  PSGroundIsoOben=#PSGroundIsoOben;
//Isolator Unten
  PSVacuumIsoUnten=#PSVacuumIsoUnten;
  PSBorderIsoUnten=#PSBorderIsoUnten;
  PSGroundIsoUnten=#PSGroundIsoUnten;
//ErdungOben
  PSVacuumErdOben=#PSVacuumErdOben;
  PSErdOben=#PSErdOben;
//Erdung Unten
  PSVacuumErdUnten=#PSVacuumErdUnten;
  PSErdUnten=#PSErdUnten;
//ZwischenRaum Oben
  PSVacuumZRaumOben=#PSVacuumZRaumOben;
  PSErdZRaumOben=#PSErdZRaumOben;
//ZwischenRaum Unten
  PSVacuumZRaumUnten=#PSVacuumZRaumUnten;
  PSErdZRaumUnten=#PSErdZRaumUnten;
//Aussere Erdung Oben
  PSAusErdOben=#PSAusErdOben;
//Aussere Erdung Unten
  PSAusErdUnten=#PSAusErdUnten;

// ***VOLUMES***
//Zentraler Teil
  PVElectrode=#PVElectrode;
  PVGround=#PVGround;
  PVBoarder=#PVBoarder;
  PVVacuum=#PVVacuum;
//Isolator Oben
  PVVacuumIsoOben=#PVVacuumIsoOben;
  PVBorderIsoOben=#PVBorderIsoOben;
```

```
  PVGroundIsoOben=#PVGroundIsoOben;
//Isolator Unten
  PVVacuumIsoUnten=#PVVacuumIsoUnten;
  PVBorderIsoUnten=#PVBorderIsoUnten;
  PVGroundIsoUnten=#PVGroundIsoUnten;
//ErdungOben
  PVVacuumErdOben=#PVVacuumErdOben;
  PVErdOben=#PVErdOben;
//Erdung Unten
  PVVacuumErdUnten=#PVVacuumErdUnten;
  PVErdUnten=#PVErdUnten;
//ZwischenRaum Oben
  PVVacuumZRaumOben=#PVVacuumZRaumOben;
  PVErdZRaumOben=#PVErdZRaumOben;
//ZwischenRaum Unten
  PVVacuumZRaumUnten=#PVVacuumZRaumUnten;
  PVErdZRaumUnten=#PVErdZRaumUnten;
//Aussere Erdung Oben
  PVAusErdOben=#PVAusErdOben;
//Ausere Erdung Unten
  PVAusErdUnten=#PVAusErdUnten;

//Vol is the total calculation domain
//Grouped are domains, for which constituents
//only a single Voltage is defined
Vol= #{PVVacuum,PVVacuumIsoOben,PVVacuumIsoUnten,
PVVacuumErdOben,PVVacuumErdUnten,PVVacuumZRaumOben,
PVVacuumZRaumUnten};
Grouped = #{PSElectrode,PSGround,PSGroundIsoOben,
PSGroundIsoUnten,PSErdOben,PSErdUnten,PSErdZRaumOben,
PSErdZRaumUnten,PSAusErdOben,PSAusErdUnten};
}

Function {
        eps0=8.854187818e-12 ;
//***Zentrum***
//PPIsoMaterial AL2O3
        epsr[PVBoarder]=7.5;
//Vakuum
        epsr[PVVacuum]=1.0;
//***Iso Oben***
//PPIsoMaterial AL2O3
        epsr[PVBorderIsoOben]=7.5;
//Vakuum Iso Oben
        epsr[PVVacuumIsoOben]=1.0;
//***Iso Unten***
//Waver IsoMaterial Si3N4
        epsr[PVBorderIsoUnten]=10.0;
//Vakuum Iso Unten
        epsr[PVVacuumIsoUnten]=1.0;
//***Erdung Oben***
//Vakuum Erdung Oben
        epsr[PVVacuumErdOben]=1.0;
//***Erdung Unten***
//Vakuum Erdung Oben
        epsr[PVVacuumErdUnten]=1.0;
//***ZRaum Oben***
```

```
//Vakuum ZRaum Oben
        epsr[PVVacuumZRaumOben]=1.0;
//***Zraum Unten***
//Vakuum ZRaum Unten
        epsr[PVVacuumZRaumUnten]=1.0;
}

Jacobian {
        { Name Vol ; Case {
// All domains expand in to infinity in z direction
// Using Jacobian VolAxi would define a system with
// a sphere in an zylindrical capacitor.
// It should not hurt to have negative radii as long
// as the system is perfectly symmetric..
                { Region All ; Jacobian Vol ; }
        } }
}

Integration {
        { Name Int ; Case { { Type Gauss ;
Case {
// 3D elements are not relevant
// This block defines the accuracy for the numerical
// integrations.
// Higher NumberOfPoint should correspond to higher
// accuracy in case of nonlinear behaviour within
// single cells.
{ GeoElement Point       ; NumberOfPoints  1 ; }
{ GeoElement Line        ; NumberOfPoints  3 ; }
{ GeoElement Triangle    ; NumberOfPoints  4 ; }
{ GeoElement Quadrangle  ; NumberOfPoints  4 ; }
{ GeoElement Tetrahedron ; NumberOfPoints  4 ; }
{ GeoElement Hexahedron  ; NumberOfPoints  6 ; }
{ GeoElement Pyramid     ; NumberOfPoints  8 ; }
{ GeoElement Prism       ; NumberOfPoints  6 ; }
                }
        } } }
}

Constraint {

        { Name GlobalElectricPotential ;
                Case {
                //Boundary condition using fixed Voltages
                { Region PSElectrode;  Value 3.0 ; }
                { Region PSGround; Value 0.0 ; }
                { Region PSGroundIsoOben;  Value 0.0 ; }
                { Region PSGroundIsoUnten; Value 0.0 ; }
                { Region PSErdOben; Value 0.0 ; }
                { Region PSErdUnten; Value 0.0 ; }
                { Region PSErdZRaumOben; Value 0.0 ; }
                { Region PSErdZRaumUnten; Value 0.0 ; }
                { Region PSAusErdOben; Value 0.0 ; }
                { Region PSAusErdUnten; Value 0.0 ; }
                }
        }
```

```
        { Name GlobalElectricCharge ;
                Case {
                //Boundary Condition defining the charge
                //of a grouped domain.For each grouped
                //domain, either a charge or a potential
                //needs to be specified.
                }
        }
}

FunctionSpace {
{ Name fs_vglob ; Type Form0 ;
// so we have scalars
BasisFunction {
// ordinary nodal basis functions everywhere
// but for the grouped domains,
// which will be grouped of course.
// Then each grouped domain constituent
// can only have a single shared value
{ Name sn ; NameOfCoef vn ; Function BF_Node ;
Support Region[{Vol}] ;
Entity NodesOf[ All,Not Grouped] ; }
{ Name sf ; NameOfCoef vfu ; Function BF_GroupOfNodes ;
Support Vol ; Entity GroupsOfNodesOf[ Grouped] ; }
}

GlobalQuantity {
{ Name GlobalElectricPotential ; Type AliasOf ;
NameOfCoef vfu ; }
{ Name GlobalElectricCharge    ; Type AssociatedWith ;
NameOfCoef vfu; }
}
Constraint {
// CFoo: unused, nonexisting boundary condition
{ NameOfCoef vn ;EntityType NodesOf ;
NameOfConstraint CFoo; }
{ NameOfCoef vfu ;EntityType GroupsOfNodesOf ;
NameOfConstraint CFoo; }

{ NameOfCoef GlobalElectricCharge ;
EntityType GroupsOfNodesOf ;
NameOfConstraint GlobalElectricCharge ; }
{ NameOfCoef GlobalElectricPotential ;
EntityType GroupsOfNodesOf ;
NameOfConstraint GlobalElectricPotential ; }
                }
        }

}

Formulation {
// first problem (Laplace equation with Dirichlet BC)
{ Name for_v ; Type FemEquation ;
Quantity {
{ Name v; Type Local;  NameOfSpace fs_vglob;}
{ Name Q; Type Global; NameOfSpace fs_vglob
[GlobalElectricCharge]; }
```

```
{ Name V; Type Global; NameOfSpace fs_vglob
[GlobalElectricPotential]; }
}
Equation {
Galerkin { [ epsr[]*Dof{d v} , {d v} ] ; In Vol;
Jacobian Vol ; Integration Int ; }
// div epsr[] grad v=0

GlobalTerm { [ -Dof{Q}/eps0 , {V} ] ; In Grouped ; }
                }
        }
}

Resolution
{
        {       Name all;System
        {
        { Name A1 ; NameOfFormulation for_v ;}
        }
        Operation
        {
        Generate[A1] ; Solve[A1] ; SaveSolution[A1] ;
        }
        }
}

PostProcessing {
        { Name all ; NameOfFormulation for_v;   Quantity
        {
        { Name v ; Value { Local { [ {v} ] ; In Vol ;
        Jacobian Vol; } } }
//{ Name e ; Value { Local { [ {d v} ] ; In Vol ;
//      Jacobian Vol; } } }
//{ Name ne ; Value { Local { [ Norm[{d v}] ] ; In Vol ;
//      Jacobian Vol; } } }
//{ Name Q ; Value { Term { [ {Q} ] ; In Grouped ; } } }
//{ Name V ; Value { Term { [ {V} ] ; In Grouped ; } } }
//{ Name C ; Value { Term { [ {Q}/{V} ] ; In Grouped; } } }
        }
        }
}

PostOperation{
        { Name all ; NameOfPostProcessing all;
        Operation {
        Print[ v , OnElementsOf Vol , File "v.pos" ] ;
        Print [ v, OnBox { {-4,-4,-0.57} {4,-4,-0.57}
        {-4,4,-0.57} {-4,-4,0.635} } {100, 100, 25},
        File "v_box.pos" ];
  //Print[ e , OnElementsOf Vol , File "e.pos" ] ;
  //Print[ ne , OnElementsOf Vol , File "ne.pos" ] ;
  //Print[Q, OnRegion Grouped, Format Table];
  //Print[V, OnRegion Grouped, Format Table];
  //Print[C, OnRegion Grouped, Format Table];
                }
        }
}
```

Appendix B: MatLab

For the analysis of phase contrast images some algorithms were programmed using the software package MatLab (The Math Works, USA). In the following an example of the calculation of the projected potential for Zach phase plates, using the output file from getdp is shown.

```
function [Q_list,V,ImgQ] = Zach_Proj_Box_2012(nz)

%Dieses Programm soll das Potential der Zach_Kronos_3D Phasen Platten
%in z-Richtung integrieren.
%
%Das eingelesene Potential ist das "v_box.pos" Potential aus getdp,
%welches Potentialwerte auf Punkten in einem box mesh enthaelt.
%
%Aus dieser Datei muessen zuvor mit einem Textverarbeitungsprogram (z.B. kate)
%alle Klammer, das "SP" und das "view v"  in Zeile 1 entvert werden.
%Input:
% nz =  26
%       Anzahl der Punkte in z-Richtung (25+1=26)
%       muss aus der v_box.pos datei ermittelt werden
%       Die Anzahl der Punkte entlang einer Linie in z-Richutung
%       sind dort immer als Block zusammengefasst.
%       Bsp: bei 25 Einteilungen entlang z-Achse (angegeben in der .pro Datei)
%       stehen in v_box.pos Datei 26 Punke in einem Block.
%
%Output:
% Q_list = Liste der xy-Koordinaten mit dazugehoerigem integriertem Potential
% V = eingelesene Liste "v_box_1V.pos"
% ImgQ = Bild (Matrix) der integrierten Potntiale

V = dlmread('v_box_08V.pos', ',');
[row,col]=size(V);
n= row/nz;  % n = Anzahl der Punkte in der xy-Ebene
            % sqrt(n) = Anzahl der Punkte in x- oder y-Richtung
            % bei quadratischem Gitter.
            % Zu entnehemen aus der .pro Datei
Q_list= zeros(n,col-1); %Liste der xy-Koordinaten mit integriertem Potential

%Integrationsberechnung ueber die Sehnentrapezformel:
%(ohne Restglied d.h.nur mit Summe ueber Trapeze unter der Kurve)
m=0;                        %counter fuer Punkte in xy-Ebene in V

for k=1:n                   %1.Loop ueber alle Punkte in der xy-Ebene
    Q = 0;                  %Flaeche (Potentialwert) unter einem Trapez
                            %in mikrometer
    for l=1:(nz-1)          %2.Loop ueber alle z-slices (nz-1=25) eines Punktes
```

```
        fa = V(m+l,4);      %erster Funktionspunkt des Trapezes
        fb = V(m+l+1,4);    %zweiter Funktionspunkt des Trapezes
        a= V(m+l,3);        %erster Punkt des Trapezes
        b= V(m+l+1,3);      %zweiter Punkt deds Trapezes
        Q = Q + (abs(b-a)/2*(fa+fb)); %Aufsummierte Flaeche unter den Trapezen
    end

    Q_list(k,1) = V(m+1,1); %x-Koordinate
    Q_list(k,2) = V(m+1,2); %y-Koordinate
    Q_list(k,3) = Q;        %Wert des Integrierten Potentials entlang z-Achse
    m=m+nz; %counter
end

%Eintragen der Werte des integrierten Potentials aus Q_list
%in eine Matrix, die auch als Bild = ImgQ dargestellt werden soll:
ImgQ = zeros(sqrt(n));      %Bild
m=0;                                        %couner

for x=1:sqrt(n)             %Loop ueber Punke der x-Koordinate
    for y=1:sqrt(n)         %Loop uebrn Punkte der y-Koordinate
        ImgQ(y,x)=Q_list(m+y,3);
    end
    m=m+sqrt(n);
end

I = flipud(ImgQ);
%Lineplot
nw= sqrt(n);
Y=1:1:nw/2;
Pot=I(round(nw/2)+1:nw,round(nw/2));
figure,plot(Y,Pot,'Color',[0 0 0],'Marker','none','LineStyle','-','LineWidth',2)

%nur noetig fuer die Bild anzeige...
%figure,bild(ImgQ)

savefile = 'Zach_Proj_Box_2012.mat';
save (savefile,'Q_list','V','ImgQ','n','nz')
end
```

Appendix C: SPIDER

The following description of the SPIDER software is taken from [79]:
SPIDER (System for Processing Image Data from Electron microscopy and Related fields) is an image processing system for electron microscopy. It has an emphasis on 3D reconstruction, Averaging of single particle macromolecule specimens,Multivariate statistical classification and Electron tomography. This software package was used for many analysis purposes of phase contrast images. In the following an scripting example of defocus determination is given:

```
; Estimates defocus from 1D rotational average and makes phase flipping
;Uses SPIDER operation 'TF ED' and 'TF CT'
; ------------ Input files ----------------
FR L
[micgr]../Micrographs/Muskel_D+_{***[mic]}   ; Micrographs
FR L
[pow]power/pw_avg{****[mic]}_{*[sec]} ; 2D power spectra
FR L
[sel_mic]../sel_micrograph        ; Micrograph file numbers
FR L
[params]../params                 ; Reconstruction parameter file
; ------------ Output files ----------------
FR L
[ctf]power/ctf{***[mic]}_{*[sec]}          ; Doc files with spectrum, envelope, noise
FR L
[out]defocus                      ; Doc file of defocus values for micrographs
; ---------------- END BATCH HEADER ------------------------------
MD                                ; Skip unnecessary output
VB OFF
MD                                ; Skip unnecessary output
TR OFF

DE                                ; Delete output doc file
[out]

SD /    Micrograph   Section   Defocus    Astig.Ang    Astig.Mag   Cutoff.Freq
[out]

UD 3,[sp_micwid]                  ;Micrograph width
[params]
UD 5,[sp_pixsiz]                  ; Pixel size
[params]
UD 7,[sp_sph_abb]                 ; Spherical aberration
[params]
UD 8,[sp_sourcesiz]               ; Source size
[params]
```

```
UD 9,[sp_def_spr]                ; Defocus spread
[params]
UD 12,[sp_acr]                   ; Amplitude contrast ratio
[params]
UD 14,[sp_lambda]                ; Lambda
[params]
UD 15,[sp_nyq]                    ;maximum spacial frequency
[params]


DO                               ; Loop over all micrographs
   UD NEXT [key],[mic]           ; Get micrograph number
   [sel_mic]                     ; Doc file          (input)
   IF([key].LE.0) EXIT


 DO LB9 [sec]=0,5                 ;loop for 5 sections

   DE                            ; Delete output doc file
   [ctf]

   ; Transfer Function -- Estimation of CTF parameters

   TF ED [v12],[v13],[v14],[v15],[v16]
   [pow]                         ; 2D spectrum          (input)
   ([sp_pixsiz], [sp_sph_abb]) ; Pixel size (A), Cs (mm)
   ([sp_lambda])                 ; Lambda
   ([sp_acr])                    ; Ampl. contrast ratio
   [ctf]                         ; Doc file          (output)

        ;[v12]= angle of astigmatism
        ;[v13]= magnitude of astigmatism
        ;[v14]= astgmatisn corrected defocus value
        ;[v15]= overall defocus without taking astigmatism into account
        ;[v16]= the cutoff frequency in 1/A

   ; Save parameters for each group in doc file
   SD [key], [mic],[sec],[v14],[v12],[v13],[v16]
   [out]                         ; Doc file          (output)


   VM
   echo ' 'Micrograph: {*****[mic]}_{*[sec]}'    'Defocus: {%f8.2%[v14]}

   FI x41,x42           ;get file information
   [micgr]_{*[sec]}
   (12,2)          ; Get image dimensions

   TF CT                ;transfere function phase flipping
   _1                                ;output
   [sp_sph_abb]                      ;spherical aberration
   ([v14],[sp_lambda])               ;defocus, lambda
   x41                               ;number of spatial frequency points
   [sp_nyq]                          ;max spatial frequency (A-1)
   ([sp_sourcesiz],[sp_def_spr])     ;source size, defocus spread
   ([v13],[v12])                     ;astigmatism, azimuth
   [sp_acr]                          ;amplitude ratio contrast
```

```
    (-1)                                    ;sign

    FT
    [micgr]_{*[sec]}
    _3

    MU
    _3
    _1
    _4
    *

    FT
    _4
    _5

    CP
    _5
    [micgr]_{*[sec]}_phasecorr

  LB9

ENDDO

UD NEXT E                          ; Finished
[sel_mic]                          ; Doc file

SD E
[out]


VM
echo 'Done. '; date

EN
```

Bibliography

[1] J. Dubochet, M. Adrian, J.J. Chang, J.C. Homo, J. Lepault, A.W. McDowall, and P. Schultz. Cryo-electron microscopy of vitrified specimens. *Quarterly reviews of biophysics*, 21(02):129–228, 1988.

[2] X. Zhang, L. Jin, Q. Fang, W.H. Hui, and Z.H. Zhou. 3.3 å cryo-em structure of a nonenveloped virus reveals a priming mechanism for cell entry. *Cell*, 141(3):472–482, 2010.

[3] Y. Cong, M.L. Baker, J. Jakana, D. Woolford, E.J. Miller, S. Reissmann, R.N. Kumar, A.M. Redding-Johanson, T.S. Batth, A. Mukhopadhyay, et al. 4.0-å resolution cryo-em structure of the mammalian chaperonin tric/cct reveals its unique subunit arrangement. *Proceedings of the National Academy of Sciences*, 107(11):4967, 2010.

[4] J.Z. Chen, E.C. Settembre, S.T. Aoki, X. Zhang, A.R. Bellamy, P.R. Dormitzer, S.C. Harrison, and N. Grigorieff. Molecular interactions in rotavirus assembly and uncoating seen by high-resolution cryo-em. *Proceedings of the National Academy of Sciences*, 106(26):10644–10648, 2009.

[5] S.W. Hell and J. Wichmann. Breaking the diffraction resolution limit by stimulated emission: stimulated-emission-depletion fluorescence microscopy. *Optics letters*, 19(11):780–782, 1994.

[6] S. Boutet, L. Lomb, G.J. Williams, T.R.M. Barends, A. Aquila, R.B. Doak, U. Weierstall, D.P. DePonte, J. Steinbrener, R.L. Shoeman, et al. High-resolution protein structure determination by serial femtosecond crystallography. *Science*, 337(6092):362–364, 2012.

[7] L. Reimer and H. Kohl. *Transmission Electron Microscopy: Physics of Image Formation*. Springer Verlag, 2008.

[8] Earl J. Kirkland. *Advanced Computing in Electron Microscopy*. Springer Verlag, 2009.

[9] F. Thon. Phase contrast electron microscopy. *Electron Microscopy in Material Sciences*, pages 571–625, 1971.

[10] H. Boersch. Über die Kontraste von Atomen im Elektronenmikroskop. *Z. Naturforschung 2a*, pages 615–633, 1947.

[11] F. Zernike. Das Phasenkontrastverfahren bei der mikroskopischen Beobachtung. *Z. tech. Physik*, 16:454–457, 1935.

[12] K. Kanaya, H. Kawakatsu, K. Ito, and H. Yotsumoto. Experiment on the electron phase microscope. *Journal of Applied Physics*, 29(7):1046–1049, 1958.

[13] HG Badde and L. Reimer. Der einfluss einer streuenden phasenplatte auf das elektronenmikroskopische bild. *Zeitschrift Naturforschung Teil A*, 25:760, 1970.

[14] K. Nagayama. Phase contrast enhancement with phase plates in electron microscopy. *Advances in Imaging and Electron Physics*, 138:69–146, 2005.

[15] R Danev, H Okawara, N Usuda, K Kametani, and K Nagayama. A novel phase-contrast transmission electron microscopy producing high-contrast topographic images of weak objects. *J. Biol. Phys*, 28:627–635, 2002.

[16] T. Matsumoto and A. Tonomura. The phase constancy of electron waves traveling through Boerschs electrostatic phase plate. *Ultramicroscopy*, 63(1):5–10, 1996.

[17] E. Majorovits, B. Barton, K. Schultheiss, F. Pérez-Willard, D. Gerthsen, and RR Schröder. Optimizing phase contrast in transmission electron microscopy with an electrostatic (Boersch) phase plate. *Ultramicroscopy*, 107(2-3):213–226, 2007.

[18] K. Schultheiß, F. Pérez-Willard, B. Barton, D. Gerthsen, and RR Schröder. Fabrication of a boersch phase plate for phase contrast imaging in a transmission electron microscope. *Review of scientific instruments*, 77:033701, 2006.

[19] R. Cambie, K.H. Downing, D. Typke, R.M. Glaeser, and J. Jin. Design of a microfabricated, two-electrode phase-contrast element suitable for electron microscopy. *Ultramicroscopy*, 107(4-5):329–339, 2007.

[20] *Comptes Rendus, Acad. Sci. (Paris)*, 157:1533 1536, 1913.

[21] J. Zach, 2008. WO/2008/061603, PCT/EP2007/009289.

[22] K. Schultheiss, J. Zach, B. Gamm, M. Dries, N. Frindt, R. Schröder, and D. Gerthsen. New electrostatic phase plate for transmission electron microscopy and its application for wave-function reconstruction. *Microscopy and Microanalysis*, 16(S2):536–537, 2010.

[23] RR Schröder, B. Barton, H. Rose, and G. Benner. Contrast enhancement by anamorphotic phase plates in an aberration corrected TEM. *Microscopy and Microanalysis*, 13(S03):8–9, 2007.

[24] D.B. Williams and C.B. Carter. *Transmission electron microscopy: a textbook for materials science*. Plenum Publishing Corporation, 1996.

[25] O. Scherzer. Über einige fehler von elektronenlinsen. *Zeitschrift für Physik A Hadrons and Nuclei*, 101:593–603, 1936. 10.1007/BF01349606.

[26] S. Uhlemann and M. Haider. Residual wave aberrations in the first spherical aberration corrected transmission electron microscope. *Ultramicroscopy*, 72(3):109–119, 1998.

[27] H. Rose. *Optik*, 85(19), 1990.

[28] M. Lentzen, B. Jahnen, CL Jia, A. Thust, K. Tillmann, and K. Urban. High-resolution imaging with an aberration-corrected transmission electron microscope. *Ultramicroscopy*, 92(3):233–242, 2002.

[29] R. Danev and K. Nagayama. Transmission electron microscopy with Zernike phase plate. *Ultramicroscopy*, 88(4):243–252, 2001.

[30] B. Gamm, K. Schultheiss, D. Gerthsen, and R.R. Schröder. Effect of a physical phase plate on contrast transfer in an aberration-corrected transmission electron microscope. *Ultramicroscopy*, 108(9):878–884, 2008.

[31] RM Glaeser, D. Typke, KH Downing, PC Tiemeijer, R. Cambie, and J. Jin. Adapting the spatial-frequency band pass of in-focus phase-contrast apertures for biological applications. *Microsc Microanal*, 13(Suppl 2):1214–1215, 2007.

[32] G. Benner and M. Matijevic. Europäisches Patentamt, 2007. EP 1 835 523 A2.

[33] Carl Zeiss AG Nano Technology Systems Division, 2011. KRONOS instruction manual.

[34] E. Majorovits, B. Barton, K. Schultheiss, F. Perez-Willard, D. Gerthsen, and RR Schröder. Optimizing phase contrast in transmission electron microscopy with an electrostatic (boersch) phase plate. *Ultramicroscopy*, 107(2):213–226, 2007.

[35] J. Zach. Phase plate, imaging method, and electron microscope, patent us 2010/0001183 a1. United States Patent Application Publication, 2010.

[36] B. Buijsse, F. van Laarhoven, A. Schmid, R. Cambie, S. Cabrini, J. Jin, and R. Glaeser. Design of a hybrid double-sideband/single-sideband (schlieren) objective aperture suitable for electron microscopy. *Ultramicroscopy*, 111:1688–1695, 2011.

[37] S. Hettler, B. Gamm, M. Dries, N. Frindt, R.R. Schröder, and D. Gerthsen. Improving fabrication and application of zach phase plates for phase-contrast transmission electron microscopy. *Microscopy and Microanalysis*, 18(5):1010, 2012.

[38] K. Schultheiß. Entwicklung und Anwendung electrostatischer Phasenplatten in der Transmissionselektronenmikroskopie. *Dissertation, Karlsruher Institut für Technologie*, 2010.

[39] C. Geuzaine and J.-F. Remacle. Gmsh: a three-dimensional finite element mesh generator with built-in pre- and post-processing facilities. *International journal for numerical methods in engineering*, 79(11):1309–1331, 2009.

[40] P. Dular, C. Geuzaine, F. Henrotte, and W. Legros. A general environment for the treatment of discrete problems and its application to the finite element method. *IEEE Transactions on Magnetics*, 34(5):3395–3398, September 1998.

[41] LG Dowell and AP Rinfret. Low-temperature forms of ice as studied by X-ray diffraction. *Nature*, 188(4757):1144–1148, 1960.

[42] J. Dubochet, J. Lepault, R. Freeman, JA Berriman, and J.C. Homo. Electron microscopy of frozen water and aqueous solutions. *J. Microsc*, 128:219–237, 1982.

[43] B. Alberts et al. Molecular biology of the cell in cell 5th.

[44] *Advances in Protein Chemistry, Fibrous Proteins: Muscle and Molecular Motors*, volume 71. Elsevier Academic Press, 2005.

[45] J.R. Harris. *Electron Microscopy in Biology: A Practical Approach*. Oxford University Press, New York, 1991.

[46] N.G. Wrigley et al. The lattice spacing of crystalline catalase as an internal standard of length in electron microscopy. *Journal of ultrastructure research*, 24(5):454, 1968.

[47] J. Krim, JG Dash, and J. Suzanne. Triple-point wetting of light molecular gases on au (111) surfaces. *Physical review letters*, 52(8):640–643, 1984.

[48] MJ Walker, D. Berman, C. Nordquist, and J. Krim. Electrical contact resistance and device lifetime measurements of au-ruo 2-based rf mems exposed to hydrocarbons in vacuum and nitrogen environments. *Tribology Letters*, 44(3):305–314, 2011.

[49] V. Panella, R. Chiarello, and J. Krim. Adequacy of the lifshitz theory for certain thin adsorbed films. *Physical review letters*, 76(19):3606–3609, 1996.

[50] J. Krim, ET Watts, and J. Digel. Slippage of simple liquid films adsorbed on silver and gold substrates. *Journal of Vacuum Science & Technology A: Vacuum, Surfaces, and Films*, 8(4):3417–3420, 1990.

[51] RP Chiarello, J. Krim, and C. Thompson. Quartz crystal microbalance and synchrotron x-ray reflectivity study of water and liquid xenon adsorbed on gold and quartz. *Surface science*, 306(3):359–366, 1994.

[52] G. Ferguson, G. Sigal, G. Whitesides, and M. Chaudhury. Contact adhesion of thin gold films on elastomeric supports- cold welding under ambient conditions. *Science*, 253(5021):776–778, 1991.

[53] V. Panella and J. Krim. Adsorption isotherm study of the fractal scaling behavior of vapor-deposited silver films. *Physical Review E*, 49(5):4179–4184, 1994.

[54] S.D. Szymanski. Argon plasma cleaning of fluorine, organic and oxide contamination using an advanced plasma treatment system. *March Plasma Systems,Concord, CA, USA*, 2007.

[55] D. Berman and J. Krim. Impact of oxygen and argon plasma exposure on the roughness of gold film surfaces. *Thin Solid Films*, 2012.

[56] M. Walker, C. Nordquist, D. Czaplewski, G. Patrizi, N. McGruer, and J. Krim. Impact of in situ oxygen plasma cleaning on the resistance of ru and au-ru based rf microelectromechanical system contacts in vacuum. *Journal of Applied Physics*, 107(8):084509–084509, 2010.

[57] L. Weber, M. Lehr, and E. Gmelin. Investigation of the transport properties of gold point contacts. *Physica B: Condensed Matter*, 217(3):181–192, 1996.

[58] L. Reimer. *Scanning Electron Microscopy: Physics of Image Formation and Microanalysis*. Springer Verlag, 1998.

[59] J.P. Martin and R. Speidel. Zur verwendung von dünnschicht-aperturblenden im elektronen-rastermikroskop. beitr. elektr. mikr. direktabb. oberfl. (4/2):345, 1971.

[60] L. Vitos, A.V. Ruban, H.L. Skriver, and J. Kollár. The surface energy of metals. *Surface Science*, 411(1-2):186–202, 1998.

[61] JJ Pireaux, M. Liehr, PA Thiry, JP Delrue, and R. Caudano. Electron spectroscopic characterization of oxygen adsorption on gold surfaces: Ii. production of gold oxide in oxygen dc reactive sputtering. *Surface science*, 141(1):221–232, 1984.

[62] http://www.plascotec.de/downloads/dlc_info.pdf.

[63] http://www.tu-chemnitz.de/physik/osmp/soft/v_07.pdf.

[64] M. Haider and H. Müller. Design of an electron optical system for the correction of the chromatic aberration cc of a tem objective lens. *Microscopy and Microanalysis*, 10:2–3, 2004.

[65] H. Rose. Outline of an ultracorrector compensating for all primary chromatic and geometrical aberrations of charged-particle lenses. *Nuclear Instruments and Methods in Physics Research Section A: Accelerators, Spectrometers, Detectors and Associated Equipment*, 519(1):12–27, 2004.

[66] B. Barton. Development and implementation of in focus phase contrast tem for materials and life sciences. *PhD Thesis, University of Heidelberg*, 2008.

[67] R. R. Schröder, B. Barton, H. Rose, and G. Benner. Contrast enhancement by anamorphotic phase plates in an aberration corrected tem. microsc microanal. *Microscopy and Microanalysis*, 13(2):136 – 137, 2007.

[68] Personal communication with M.Haider and J. Zach, CEOS GmbH.

[69] H. Mueller. A coherence function approach to image simulation. *PhD Thesis, Technische Universität Darmstadt*, 2000.

[70] P. Schorsch. Simulation energiegefilterter elektronenmikroskopischer bilder unter berücksichtigung inelastischer streuprozesse. *PhD Thesis, Technische Universität Darmstadt*, 2001.

[71] K. Nagayama. Development of phase plates for electron microscopes and their biological application. *European Biophysics Journal*, 37(4):345–358, 2008.

[72] R. Danev and K. Nagayama. Single particle analysis based on zernike phase contrast transmission electron microscopy. *Journal of structural biology*, 161(2):211–218, 2008.

[73] K. Murata, X. Liu, R. Danev, J. Jakana, M.F. Schmid, J. King, K. Nagayama, and W. Chiu. Zernike phase contrast cryo-electron microscopy and tomography for structure determination at nanometer and sub-nanometer resolutions. *Structure (London, England: 1993)*, 18(8):903, 2010.

[74] A. Walter, H. Muzik, H. Vieker, A. Turchanin, A. Beyer, A. Gölzhäuser, M. Lacher, S. Steltenkamp, S. Schmitz, P. Holik, et al. Practical aspects of boersch phase contrast electron microscopy of biological specimens. *Ultramicroscopy*, 2012.

[75] H. Mueller, J. Jin, R. Danev, J. Spence, H. Padmore, and R.M. Glaeser. Design of an electron microscope phase plate using a focused continuous-wave laser. *New journal of physics*, 12(7):073011, 2010.

[76] B. Gamm, M. Dries, K. Schultheiss, H. Blank, A. Rosenauer, RR Schröder, and D. Gerthsen. Object wave reconstruction by phase-plate transmission electron microscopy. *Ultramicroscopy*, 110(7):807–814, 2010.

[77] http://geuz.org/gmsh/#documentation.html.

[78] http://geuz.org/getdp/doc/texinfo/getdp.html.

[79] http://www.wadsworth.org/spider_ doc/spider/docs/spider.html.

Publications

Journal publications

S. Hettler, B. Gamm, M. Dries, N. Frindt, R. R. Schröder, and D. Gerthsen, Improving Fabrication and Application of Zach Phase Plates for Phase-Contrast Transmission Electron Microscopy. *Microscopy and Microanalysis*, 18(5):1010, 2012.

K. Schultheiss, J. Zach, B. Gamm, M. Dries, N. Frindt, R. R. Schröder, and D. Gerthsen, New Electrostatic Phase Plate for Phase-Contrast Transmission Electron Microscopy and Its Application for Wave-Function Reconstruction. *Microscopy and Microanalysis*, 16(06):785, 2010.

N. Frindt, M. Oster, L. Dieterle, K. Schultheiss, S. Hettler, B. Gamm, D. Gerthsen, and R. R. Schröder, Electrostatic Zach phase plate imaging for Transmission Electron Microscopy with tunable phase contrast of frozen-hydrated biological samples. - in preparation -

N. Frindt, M. Oster, R. R. Schröder, H. Müller, M. Haider, Anamorphic electrostatic phase plates for Transmission Electron Microscopy with Quadrupole Optics - in preparation -

Conference talks / selected oral presentations

N. Frindt, S. Hettler, M. Oster, B. Gamm, M. Dries, K. Schultheiss, D. Gerthsen and R.R. Schröder.Electrostatic Zach phase plate imaging with invertible phase contrast of frozen-hydrated biological samples. EMC 2012, Manchester, United Kingdom.

N. Frindt, M. Oster, R.R. Schroeder, S. Hettler, B. Gamm, M. Dries, D. Gerthsen and K. Schultheiss. Tunable phase contrast of vitrified macromolecular complexes by an obstruction minimized electrostatic phase plate. M&M 2012, Phoenix, Arizona, USA.

N. Frindt, B. Gamm, S. Hettler, M. Oster, K. Schultheiß, I. Wacker, D. Gerthsen R.R. Schröder. Zach phase plate imaging for transmission electron microscopy of macromolecular complexes. MC 2011, Kiel, Germany.

N. Frindt, K. Schultheiss, B. Gamm, M. Dries, J. Zach, D. Gerthsen and R. R. Schröder. The Way to an Ideal Matter-free Zernike and Hilbert TEM Phase Plate: Anamorphotic Design and First Experimental Verification in Isotropic Optics. M&M 2010, Portland, Oregon, USA.

Conference posters

M. Oster, N. Frindt, R.R. Schröder. Automating phase plate assisted phase contrast microscopy with Leginon and Zeiss TEMs. EMC 2012, Manchester, United Kingdom

M. Oster, N. Frindt and R.R. Schröder. Simulation of physical phase plate mediated phase contrast using YaMS. MC 2011, Kiel, Germany

S. Hettler, B. Gamm, M. Dries, K. Schultheiß, N. Frindt R. R. Schröder and D. Gerthsen. Optimized Fabrication and Application of Electrostatic Phase Plates for Transmission Electron Microscopy. MC 2011, Kiel, Germany

B. Gamm, S. Hettler, M. Dries, K. Schultheiss, N. Frindt, R. R. Schröder and D. Gerthsen. Application of a Zach Phase Plate in High-Resolution Transmission Electron Microscopy. MC 2011, Kiel, Germany

M. Dries, B. Gamm, S. Hettler, D. Gerthsen, K. Schultheiß, N. Frindt and R. R. Schröder. Electrostatic Charging in Phase-Plate Transmission Electron Microscopy: Attempts to Reduce Contamination. MC 2011, Kiel, Germany

E Majorovits, I Angert, G Benner, N Frindt, S Fujita-Becker and R Schröder, Cryo Imaging at 60 keV and 200 keV at a Cs-Corrected ZEISS Libra 200. M&M 2011, Nashville, Tennessee, USA

N. Frindt, M. Oster. Schultheiß, B. Gamm, M. Dries, J. Zach, D. Gerthsen, R.R. Schröder. Matter free anamorphoticZernike and Hilbert TEM phase plates: Optimized designs for imaging and alignment process. IMC17 2010, Rio de Janeiro, Brazil. Participation and travelling expenses were funded by the Deutsche Gesellschaft für Elektronenmikroskopie (DGE)

N Frindt, B Gamm, M Dires, K Schultheiss, D.Gerthsen, R R Schröder. Simulating Hilbert phase contrast produced by an anamorphotic electrostatic phase plate. MC 2009, Graz, Austria

Acknowledgments

I would like to thank my doctoral adviser Prof. Rasmus R. Schröder for his very instructive and friendly mentoring of my doctoral thesis during the last years. For the faculty of physics and astronomy I would like to thank Prof. Dr. Ulrich Schwarz for his role as first co-advisor.
Furthermore I would like to thank Simon Hettler, Björn Gamm, Katrin Schultheiß and Prof. Dagmar Gerthsen (members or former members of the Laboratory for Electron Microscopy, KIT) for the successful collaboration during this project. Special thanks go to my group colleagues Marco Oster and Levin Dieterle who were directly involved in the phase plate project. Many of the results would have not been achieved without their help. I am also very thankful to my group colleagues Martin Pfannmöller, Sarah Wulf, Götz Hofhaus, Johan Zeelen, Setsuko Fujita-Becker, Ira Röder, Christian Wacker and Caterina Trimarchi-Keller for their help, suggestions and taking care of a good working atmosphere in our group.
At CEOS GmbH I would like to thank Max Haider and Joachim Zach for their contributions and ideas concerning the phase plate project. Many thanks go also to Gerd Benner from Carl Zeiss Microscopy for support on the Zeiss Libra 200 DMU.
For financial support I would like to thank the Deutsche Forschungsgemeinschaft (DFG), the Deutsche Gesellschaft für Elektronenmikroskopie (DEG) and the European Microscopy Society (EMS).

Eidesstattliche Versicherung / Affidavit

Eidesstattliche Versicherung

Bei der eingereichten Dissertation zum Thema "Development and implementation of electrostatic Zach phase plates for phase contrast transmission electron microscopy" handelt es sich um meine eigenständige erbrachte Leistung.
Ich habe nur die angegebenen Quellen und Hilfsmittel benutzt und mich keiner unzulässigen Hilfe Dritter bedient. Insbesondere habe ich wörtlich oder sinngemäß aus anderen Werken übernommene Inhalte als solche kenntlich gemacht.

Affidavit

The presented dissertation with the title "Development and implementation of electrostatic Zach phase plates for phase contrast transmission electron microscopy" is my own independent work.
I have only used the cited references and I have not made unauthorised use of services of a third party. Work that is cited or reproduced is indicated in particular.

Heidelberg, 09.12.2012